

ANALYSIS AND DESIGN OF VANADIUM REDOX FLOW BATTERY



Mr. Tossaporn Jirabovornwisut

จุฬาลงกรณ์มหาวิทยาลัย
CHULALONGKORN UNIVERSITY

A Thesis Submitted in Partial Fulfillment of the Requirements
for the Degree of Master of Engineering in Chemical Engineering
Department of Chemical Engineering
Faculty of Engineering
Chulalongkorn University
Academic Year 2018
Copyright of Chulalongkorn University

การวิเคราะห์และออกแบบแบตเตอรี่แบบมีการไหลของวานาเดียมที่เกิดปฏิกิริยารีดอกซ์



วิทยานิพนธ์นี้เป็นส่วนหนึ่งของการศึกษาตามหลักสูตรปริญญาวิศวกรรมศาสตรมหาบัณฑิต

สาขาวิชาวิศวกรรมเคมี ภาควิชาวิศวกรรมเคมี

คณะวิศวกรรมศาสตร์ จุฬาลงกรณ์มหาวิทยาลัย

ปีการศึกษา 2561

ลิขสิทธิ์ของจุฬาลงกรณ์มหาวิทยาลัย

Thesis Title ANALYSIS AND DESIGN OF VANADIUM REDOX
FLOW BATTERY
By Mr. Tossaporn Jirabovornwisut
Field of Study Chemical Engineering
Thesis Advisor Assistant Professor Amornchai Arpornwichanop,
D.Eng.

Accepted by the Faculty of Engineering, Chulalongkorn University in Partial
Fulfillment of the Requirement for the Master of Engineering

..... Dean of the Faculty of Engineering
(Associate Professor Supot Teachavorasinskun, D.Eng.)

THESIS COMMITTEE

..... Chairman
(Varun Taepaisitphongse, Ph.D.)

..... Thesis Advisor
(Assistant Professor Amornchai Arpornwichanop,
D.Eng.)

..... Examiner
(Palang Bumroongsakulsawat, Ph.D.)

..... External Examiner
(Assistant Professor Pornchai Bumroongsri, D.Eng.)



จุฬาลงกรณ์มหาวิทยาลัย
CHULALONGKORN UNIVERSITY

ทศพร จิรวรรณวิสุทธิ์ : การวิเคราะห์และออกแบบแบตเตอรี่แบบมีการไหลของวานาเดียมที่เกิดปฏิกิริยารีดอกซ์ . (ANALYSIS AND DESIGN OF VANADIUM REDOX FLOW BATTERY) อ.ที่ปรึกษาหลัก : ศศ. ดร.อมรรชย์ อารักษ์วิชานพ

งานวิจัยนี้นำเสนอแบบจำลองทางพลวัตของแบตเตอรี่แบบมีการไหลของวานาเดียมที่เกิดปฏิกิริยารีดอกซ์เพื่อใช้ในการวิเคราะห์ประสิทธิภาพและความสามารถในการกักเก็บพลังงานที่ลดลงเนื่องจากความไม่สมดุลในสารละลายอิเล็กโทรไลต์ ซึ่งเกิดจากปฏิกิริยาข้างเคียงของการแพร่ผ่านเยื่อเลือกผ่านชนิดแลกเปลี่ยนไอออนรวมไปถึงการเกิดแก๊สออกซิเจนและไฮโดรเจน จากการศึกษพบว่า ความสามารถในการกักเก็บพลังงานที่ลดลงเป็นผลมาจากการเปลี่ยนแปลงความเข้มข้นของสารวานาเดียมที่ขึ้นกับชนิดของวัสดุที่ใช้เป็นขั้วไฟฟ้าและเยื่อเลือกผ่านชนิดแลกเปลี่ยนไอออน รวมไปถึงสภาวะที่ใช้ดำเนินงานของแบตเตอรี่ โดยการเปลี่ยนแปลงความเข้มข้นของวานาเดียม จากการแพร่ผ่านเยื่อเลือกผ่าน ขึ้นอยู่กับความเข้มข้นของสารละลายอิเล็กโทรไลต์เริ่มต้นและระยะเวลาที่ใช้ในการดำเนินงานของแบตเตอรี่ นอกจากนี้อุณหภูมิที่สูงขึ้นทำให้อัตราการแพร่ผ่าน และปฏิกิริยาข้างเคียงการเกิดแก๊สมีค่ามากยิ่งขึ้น อย่างไรก็ตามสำหรับการควบคุมอัตราการไหลของสารละลายอิเล็กโทรไลต์แบบเปลี่ยนแปลงไม่สามารถเพิ่มความสามารถในการกักเก็บพลังงานและประสิทธิภาพได้เนื่องจากผลของความไม่สมดุลในสารละลายอิเล็กโทรไลต์ ดังนั้นเพื่อแก้ปัญหาดังกล่าว การแก้ปัญหาที่เหมาะสมแบบพลวัตถูกจัดทำขึ้น เพื่อหาการเปลี่ยนแปลงของอัตราการไหลที่เหมาะสมระหว่างการดำเนินงานของแบตเตอรี่ซึ่งประสิทธิภาพของแบตเตอรี่สามารถเพิ่มขึ้น ด้วยการดำเนินงานด้วยอัตราการไหลที่เหมาะสมซึ่งเปลี่ยนแปลงไปตามค่าศักย์ไฟฟ้าวงจรเปิดและศักย์ไฟฟ้าสูญเสียที่เกิดจากการถ่ายโอนมวลและระดับความไม่สมดุลในสารละลายอิเล็กโทรไลต์ นอกจากนี้เพื่อเพิ่มสมรรถนะของระบบ การแก้ปัญหาที่เหมาะสมแบบพลวัตออนไลน์ถูกนำเสนอเพื่อหาค่าอัตราการไหลที่เหมาะสมให้สอดคล้องกับการเปลี่ยนแปลงของกระแสที่ไม่แน่นอน โดยตัวกรองคาบมานแบบขยายถูกนำมาใช้เพื่อประมาณค่าความเข้มข้นของวานาเดียมเพื่อใช้ในการคำนวณค่าอัตราการไหลที่เหมาะสม โดยใช้งานร่วมกับการวัดศักย์ไฟฟ้าวงจรเปิดแบบตัดแปลง ซึ่งวิธีดังกล่าวสามารถเพิ่มประสิทธิภาพของระบบและยังป้องกันไม่ให้แบตเตอรี่ดำเนินงานโดยที่ค่าศักย์ไฟฟ้าถึงขอบเขตที่กำหนด ก่อนที่ระดับของกักเก็บและจ่ายพลังงานตามเป็นไปตามต้องการ



สาขาวิชา วิศวกรรมเคมี
ปีการศึกษา 2561

ลายมือชื่อนิสิต
ลายมือชื่อ อ.ที่ปรึกษาหลัก

5970174221 : MAJOR CHEMICAL ENGINEERING

KEYWORD Vanadium redox flow battery, Electrolyte imbalance, Dynamic model, Optimal electrolyte flow rate, Performance analysis

D: Tossaporn Jirabovornwisut : ANALYSIS AND DESIGN OF VANADIUM REDOX FLOW BATTERY. Advisor: Asst. Prof. Amornchai Arpornwichanop, D.Eng.

In this study, the dynamic model of a vanadium redox flow battery (VRFB) was developed to analyze the battery performance and capacity degradation caused by an electrolyte imbalance from hydrogen and oxygen evolution and self-discharge side reactions. The model-based analysis of the VRFB performance revealed that the rate of battery capacity loss resulting from the electrolyte imbalance considerably depended on electrode and membrane material as well as operating conditions. Self-discharge reactions were controlled by the operational time of the battery. In addition, the rate of capacity degradation increased with an increase in the total vanadium concentration and operating temperature, affecting the increased rates of the gassing and self-discharge side reactions. It was also found that operating the VRFB with variable flow rate did not improve the battery capacity and efficiency during long-term operation due to the electrolyte imbalance. To solve this problem, the dynamic optimization was performed to determine an optimal electrolyte flow rate. The obtained optimal flow rate profile can maximize the system efficiency, regarding the variation in an open circuit voltage and concentration overpotentials, and the electrolyte imbalance level. To further improve the performance of the VRFB, an on-line dynamic optimization was proposed for updating the optimal flow rate when the battery is operated under the intermittent current density. The extended Kalman filter was integrated into the proposed on-line optimization to estimate the current state of the vanadium concentration in the VRFB from the measurement of modified open circuit voltage. The results showed that the on-line optimization approach can increase the VRFB system efficiency and prevent the battery voltage from reaching to the limited voltage before the battery achieve the desired state of charge.

CHULALONGKORN UNIVERSITY

Field of Study: Chemical Engineering

Student's Signature

Academic Year: 2018

Advisor's Signature

Year:

.....

ACKNOWLEDGEMENTS

First of all, I would like to express my sincere thanks to my thesis advisor, Assistant Professor Dr. Amornchai Arpornwichanop, for his invaluable recommendation as well as constant encouragement throughout this research. I am most grateful for his teaching and suggestion for research methodology and point of view towards life. This thesis would not have been completed without the support that I have always received from him.

Moreover, I gratefully thank the chairman, Dr. Varun Teapaisitphongse, and the other members of the thesis committee, Dr. Palang Bumroongsakulsawat and Assistant Professor Dr. Pornchai Bumroongsri, for their times and valuable suggestion in improving my research. My sincere thanks also go to Associate Professor Dr. Yong-Song Chen for offering me the summer internship opportunities in his research group on the vanadium redox flow battery and providing the financial support during my visit at National Chung Cheng University, Taiwan.

Furthermore, I would also like to thank the Department of Chemical Engineering, Chulalongkorn University, and the Computational Process Engineer Research Unit for providing the financial support during my Master's degree study and all my friends in the Computational Process Engineer Research Unit and Control and System Engineering Research Center for their friendships and help.

Finally, I most gratefully thank my family, especially my mother, Mrs. Rattana Jirabovornwisut, my father, Mr. Khunchai Jirabovornwisut, and my brother Mr. Sorarat Jirabovornwisut, for their love, encouragement and support.

Tossaporn Jirabovornwisut

TABLE OF CONTENTS

	Page
ABSTRACT (THAI)	iii
ABSTRACT (ENGLISH)	iv
ACKNOWLEDGEMENTS	v
TABLE OF CONTENTS	vi
LIST OF FIGURES	ix
LIST OF TABLES	xiii
NOMENCLATURES	xv
CHAPTER I INTRODUCTION	1
1.1 Background and motivation	1
1.2 Research objective	4
1.3 Scope of research	4
CHAPTER II THEORIES	6
2.1 Principle of electrochemistry	6
2.1.1 Definitions	6
2.1.2 Overpotential and actual cell voltage	8
2.2 Cell components of vanadium redox flow battery	11
2.2.1 Current collector	11
2.2.2 Flexible graphite foil	12
2.2.3 Graphite block	12
2.2.4 Flow field	12
2.2.5 Electrode	12
2.2.6 Membrane	13

2.3 Operation of vanadium redox flow battery	13
2.4 Side reaction and capacity loss	15
2.5 Kalman filter	16
2.5.1 Kalman filter Algorithm	16
2.5.2 Observability	19
2.5.3 Tuning of Kalman Filter	21
2.6 Dynamic optimization.....	22
2.6.1 Variation approach for optimal control problem.....	24
2.6.2 Discretization techniques with sequential approach	26
CHAPTER III LITERATURE REVIEWS	28
3.1 Causes and effects of an electrolyte imbalance	28
3.1.1 Gassing side reactions	29
3.1.2 Air oxidation.....	32
3.1.3 Ion diffusion	34
3.1.4 Volumetric transfer.....	38
3.2 Performance prediction by mathematical model of VRFB.....	39
3.2.1 Application of the VRFB multi-dimensional model or zero-dimensional model.....	40
3.2.2 Electrolyte imbalance model	42
3.2.3 Pump power loss model.....	44
3.3 Operating condition of the VRFB.....	45
CHAPTER IV MODELING OF VANADIUM REDOX FLOW BATTERY	47
4.1 Mathematical model of vanadium redox flow battery	47
4.1.1 Model assumptions	47
4.1.2 Electrochemical models	48

4.1.3 Conservation equation.....	51
4.1.4 Pump power model.....	53
4.2 Extended Kalman filter for vanadium redox flow batteries	54
4.2.1 Observability matrix for vanadium redox flow batteries models.....	55
4.3 Simulation method.....	59
4.4 Model validation	63
CHAPTER V PERFORMANCE ANALYSIS OF VANADIUM REDOX FLOW BATTERY UNDER THE ELECTROLYTE IMBALANCE CONDITIONS	67
5.1 Effect of the electrolyte imbalance	67
5.2 Effect of the operating conditions on battery performance	73
5.2.1 Current density	74
5.2.2 Vanadium and proton concentrations.....	78
5.2.3 Operating temperature.....	84
5.2.4 Electrolyte flow rate.....	87
CHAPTER VI DESIGN OF ELECTROLYTE FLOW RATE CONTROL STRATEGY FOR IMPROVING THE PERFORMANCE OF VANADIUM REDOX FLOW BATTERY	90
6.1 Problem statements.....	90
6.2 Dynamic optimization.....	91
6.2.1 Comparison of the effect of electrolyte flow rate control strategies on the battery performance.....	92
6.2.2 Extended Kalman Filter for vanadium redox flow battery.....	99
6.3 On-line dynamic optimization	104
6.3.1 Effect of current density fluctuation on the optimal electrolyte flow rate profile	104
CHAPTER VII CONCLUSIONS AND RECOMMENDATIONS	109
9.1 Conclusions.....	109
9.2 Recommendations.....	110
REFERENCES	112
VITA.....	117

LIST OF FIGURES

	Page
Figure 2.1 Cell components and their arrangement of single VRFB cells.	11
Figure 2.2 Schematic and mechanism of redox reaction in a VRFB system.....	14
Figure 2.3 Optimal control solution via the sequential approach	27
Figure 3.1 (a) Potentiodynamic polarization curves of a graphite electrode in 2 mol dm ⁻³ from 0.4 to 1.5 V vs SCE at 20–60 °C. (b) Correlation between coulombic efficiency and operating temperature.....	30
Figure 3.2 Hydrogen evolution rate for all VRFBs employing different carbon felt electrodes	31
Figure 3.3 Effect of operating temperature on (a) the charge-discharge battery voltage and (b) the coulombic and energy efficiency.....	32
Figure 3.4 (a) Charge-discharge characteristic voltage and current. (b) Discharge capacity	33
Figure 3.5 Relationship between SOC degradation and reaction time under different (a) volume to air-electrolyte solution interface area ratio, (b) vanadium concentration, and (c) sulfuric concentration	34
Figure 3.6 Concentration of positive and negative electrolytes during 200 cycles for (a) CMV membrane, (b) AMV membrane, and (c) Nafion 115 membrane	36
Figure 3.7 Open circuit voltage curve during the self-discharge process.....	38
Figure 3.8 Change of electrolyte volume due to bulk water transfer across the membrane during 200 cycles of the charge-discharge process.....	39
Figure 3.9 Comparison of capacity loss in three different types of membrane (a) CMV (b) AMV (c) Nafion 115	43
Figure 3.10 Comparison of capacity change with and without bulk electrolyte transfer phenomenon across 200 cycles.....	44
Figure 3.11 Energy and battery efficiencies under various flow rates.....	46

Figure 4.1 The schematic of the experiment to measure the open circuit voltage: (a) conventional OCV and (b) modified OCV	57
Figure 4.2 Algorithm for calculating battery voltage variation during charging-discharging process and performance analysis.	60
Figure 4.3 Algorithm for calculating the optimal electrolyte flow rate maximizing the system efficiency.	62
Figure 4.4 Algorithm for estimating the vanadium concentration by Extended Kalman Filter with the modified open circuit voltage measurement.	63
Figure 4.5 Comparison of the simulation results with the experimental data (a) charge-discharge characteristic curve. (b) effect of imbalance level on discharge capacity	66
Figure 5.1 Efficiencies of vanadium redox flow batteries (VRFB) with different electrode and membrane types.	70
Figure 5.2 Capacity of vanadium redox flow batteries (VRFB) with different electrode and membrane types.	71
Figure 5.3 Vanadium concentration and state of charge (SOC) of the electrolyte at the upper and lower limit voltages during 200 cycles.	73
Figure 5.4 Effect of current density on battery voltage curve with maximum and minimum SOC at voltage limit.	74
Figure 5.5 Effect of current density on (a) battery overpotentials and (b) HER current density and initial SOC of OER.	76
Figure 5.6 Effect of current density on (a) battery power and capacity and (b) battery efficiency.	77
Figure 5.7 Effect of current density on long-term capacity variation.	78
Figure 5.8 Effect of vanadium concentration on battery voltage curve with maximum and minimum SOC at voltage limit.	79
Figure 5.9 Effect of (a) vanadium concentration and (b) proton concentration on overpotentials.	80

Figure 5.10 Effect of vanadium and proton concentration on (a) battery capacity and power and (b) battery efficiencies.....	81
Figure 5.11 Effect of (a) vanadium concentration and (b) proton concentration on HER current density and initial SOC of OER.	82
Figure 5.12 Effect of proton concentration on standard potential of (a) redox couples $\text{VO}^{2+}/\text{VO}_2^+$ and OER (b) redox couples $\text{V}^{2+}/\text{V}^{3+}$ and HER.	82
Figure 5.13 Effect of (a) vanadium and (b) proton concentration on long-term capacities.....	83
Figure 5.14 Effect of operating temperature on (a) battery capacity and power and (b) battery efficiency.	85
Figure 5.15 Effect of operating temperature on long-term capacity variation of AMV membrane.....	85
Figure 5.16 Effect of operating temperature on HER current density at upper limit voltage.....	86
Figure 5.17 Effect of electrolyte flow rate on (a) overpotentials and (b) HER current density and initial SOC of OER.....	87
Figure 5.18 Effect of electrolyte flow rate on (a) battery capacity and power and (b) battery efficiency.	88
Figure 5.19 (a) Effect of flow factor on battery capacity and efficiency. (b) comparison the effect of constant and variable electrolyte flow rate approaches on long-term capacity.	89
Figure 6.1 Optimal electrolyte profile with different time interval.	92
Figure 6.2 Battery voltage curve under different flow rate control strategies.	93
Figure 6.3 Electrolyte flow rate variation during charging-discharging process under different flow rate control strategies.	94
Figure 6.4 Variation of vanadium concentration in negative half-cell under different flow rate control strategies.....	94
Figure 6.5 Effect of electrolyte flow rate on the open circuit voltage.	95

Figure 6.6 Comparison of electrolyte flow rate with different charging current density between (a) variable flow rate control and (b) optimal flow rate control.....	97
Figure 6.7 Comparison of electrolyte flow rate under different electrolyte imbalance level between (a) variable flow rate control (b) optimal flow rate control.....	98
Figure 6.8 Effect of electrolyte imbalance under different flow rate control strategies on (a) battery capacity and (b) system efficiency.	99
Figure 6.9 Positive and negative open circuit voltage measured by modified open circuit cell.....	101
Figure 6.10 Estimation result of vanadium concentration in (a) negative half-cell and (b) positive half-cell.....	101
Figure 6.11 Charging current density with (a) positive pulse current and (b) hybrid pulse current.....	102
Figure 6.12 Estimation result of vanadium concentration under positive pulse charging current density.....	103
Figure 6.13 Estimation result of vanadium concentration under hybrid pulse charging current density.....	103
Figure 6.15 Comparison of battery voltage under off-line flow rate and on-line flow rate control.	106
Figure 6.16 Effect of high charging current density on the on-line electrolyte flow rate profile.....	107
Figure 6.17 Comparison of battery voltage charging with high charging current density under off-line flow rate and on-line flow rate control.....	108

LIST OF TABLES

	Page
Table 2.1 Dimension of discrete time system variables for Kalman filter algorithm.	18
Table 2.2 Comparison of the equation set between KF and EKF	19
Table 2.3 Comparison of static and dynamic optimization.....	22
Table 2.4 Comparison of function and functional.....	23
Table 2.5 Comparison of the solution of static and dynamic optimization.....	24
Table 4.1 Summary of the total flux movement across the electrode membrane.	52
Table 4.2 Concentration variation due to molar flux movement across the electrode membrane during the self-discharge reactions.	53
Table 4.3 Definition of battery performance.....	54
Table 4.4 Model parameters used in the simulation of VRFB	64
Table 5.1 Kinetic data for the hydrogen evolution reaction (HER) and redox reactions in negative half-cells with different electrode materials.....	68
Table 5.2 Vanadium ion diffusion coefficients for different membrane types	68
Table 5.3 Case studies for different types of electrodes and membrane materials	69
Table 5.4 Operating parameters for the performance investigation.....	73
Table 6.1 Problem statement for maximizing the system efficiency	91
Table 6.2 Effect of time interval number on the total charging energy and battery voltage.....	91
Table 6.3 Comparison of charging-discharging performance under different control strategies	97
Table 6.4 Effect of electrolyte imbalance level on the charging-discharging time of different flow rate control strategies	99
Table 6.5 Extended Kalman filter covariance matrix for vanadium redox flow batteries.....	100

Table 6.6 Mean absolute error of vanadium concentration with different flow rate control 102

Table 6.7 Mean absolute error of vanadium concentration with different current profile..... 104



NOMENCLATURES

A	area [m ²]
A_s	specific surface area [m ² m ⁻³]
C	mole concentration [mol L ⁻¹]
d	thickness [m]
d_f	electrode pore diameter [m]
D^{eff}	effective diffusion coefficient [m ² s ⁻¹]
E	potential [V]
E^0	standard potential [V]
F	Faraday's constant [A s mol ⁻¹]
i	current density [mA cm ⁻²]
I	current [A]
k	rate constant [m s ⁻¹]
n	number of electron transfer [-]
N	molar flux [mol m ⁻² s ⁻¹]
Q	electrolyte flow rate [ml s ⁻¹]
R	gas constant [J mol ⁻¹ K ⁻¹]
Re	Reynolds number [-]
s	stoichiometric coefficient [-]
T	temperature [K]

Greek symbols

ρ	density [kg m ³]
μ	viscosity [Pa s]
σ	conductivity [S m ⁻¹]
α	transfer coefficient of redox reaction
β	transfer coefficient of gassing side reaction
ϕ	potential [V]
η	overpotential [V]
κ_m	local mass transfer coefficient [m s ⁻¹]
λ	permeability of porous electrode [m ²]
Δp	difference pressure between half-cell [bar]

Subscripts and superscripts

a	anode
act	activation
B	bulk
c	cathode
conc	concentration
Diff	diffusion
e	electrode
elec	electrolyte
Eosm	electro-osmosis
g	gassing side reaction
Hydr	hydraulic pressure

j	half-cell j
k	active species k
lim	limiting
m	mass transfer
mem	membrane
Mig	migration
n	negative
ohm	ohmic
Ox	oxidation
p	positive
ref	reference
Red	reduction
S	Surface

Abbreviations

CE	coulombic efficiency
DC	discharge capacity
EE	energy efficiency
HER	hydrogen evolution reaction
MOCV	modified open circuit voltage
OCV	open circuit voltage
OER	oxygen evolution reaction
RFB	redox flow battery
SE	system efficiency
SOC	state of charge



VE	voltage efficiency
VRFB	vanadium redox flow battery



CHAPTER I

INTRODUCTION

1.1 Background and motivation

Energy and electricity consumption have been increasing from an increase in the world population, leading to the requirement of large energy production capacity. Presently, fossil fuels are the main source of electricity generation. However, the negative environmental effects from the conventional processing of fossil fuels have been realized (Aneke and Wang, 2016). Renewable energy is regarded as one of the alternatives for implementation in the electrical grid. Various renewable energy sources such as solar, tidal and wind, can be converted into electrical energy in the application of peak shaving or load leveling (Rohit *et al.*, 2017). However, the nature of these energy sources has the drawback of intermittent and fluctuant problems (Weber *et al.*, 2011). To maintain the stability of energy supply, an electrical energy storage system must be integrated into the manufacturing process of electricity from renewable energy sources. The crucial point is that the electrical energy is not easy to be directly stored in its form, leading to a conversion into other forms such as mechanical energy storage, thermal energy storage, thermochemical energy storage, chemical energy storage and electrochemical energy storage (Luo *et al.*, 2015).

Electrochemical energy storage is a system for converting and storing the electricity by an electrochemical reaction (Hadjipaschalis *et al.*, 2009). The major types of this system, e.g., rechargeable batteries and redox flow batteries, are widely used for energy storage (Luo *et al.*, 2015). The mechanism of electrochemical reactions takes place in the electrochemical cell, containing an electrolyte, and cathode and anode electrodes. Both of the electrodes are connected via an electronic conductor where electrons flow through and the electrical circuit is completed by flowing of ions through the electrolyte from one electrode to the other. The advanced development in the electrochemical energy storage leads to many types of rechargeable and redox flow batteries. Various factors are used to decide the suitable energy storage technology

including the state of technology, power rating, discharge time, storage duration, capital cost, cycles efficiency, energy, and power density and life cycle time (H. Chen *et al.*, 2009).

The redox flow battery (RFB) is an energy storage system that is being developed for use in the large-scale electric utility service (M. Skyllas-Kazacos *et al.*, 2013). Its main advantage is its flexibility because the power and energy capacity of the system can be designed separately. The power output is determined by the number of cells in the stack, whereas the stored energy capacity is limited by the size of the electrolyte tank (Khazaeli *et al.*, 2015). Vanadium redox flow batteries (VRFBs) apply V^{2+}/V^{3+} and VO^{2+}/VO_2^+ active species in sulfuric acid to the respective negative and positive half-cells. Cross-contamination is avoided because vanadium is employed in both half cells. This is the mechanism in which a species crosses over and reacts irreversibly with elements in the opposite half-cell, leading to a loss in capacity and degradation in the system performance (Zhang *et al.*, 2017). Although the membrane is designed only to allow protons and other charge-carrying ions to pass through, it cannot completely prevent the diffusion of vanadium ions across the membrane via convection, diffusion, and migration. Moreover, the diffusing ions that react with other ions in the opposite half-cell contribute towards capacity loss via self-discharge reactions (Tang *et al.*, 2011). Under normal VRFB operation, the electrode potential is higher than the standard potential of the oxygen (OER) and lower for hydrogen (HER) evolution reactions. HER and OER can, therefore, occur at the electrode surface and some applied current must be consumed to charge the battery (Al-Fetlawi *et al.*, 2010; Shah *et al.*, 2010). Furthermore, air oxidation side reactions in the negative electrolyte solution reservoir can lead to a capacity loss by self-discharge when the electrolyte interface comes into contact with air (Ngamsai and Arpornwichanop, 2015b). Thus, it is important to understand the effect of the gassing side reactions as well as diffusion of the species across the membrane, which leads to an electrolyte imbalance (an unequal number of reduced species in one side of the half-cell compared to the oxidized species in the other half-cell).

A mathematical model that can describe such phenomena and predict the battery efficiency, taking into account the effect of vanadium diffusion across the membrane and the gassing side reactions, plays a significant role in the development of the control and management systems for VRFB (Tang *et al.*, 2011). Different VRFB models have been developed to investigate the VRFB performance. Two- and three-dimensional models based on the conservation equations of mass, energy, charge, and momentum integrated with an electrochemical model were proposed (Al-Fetlawi *et al.*, 2009; Ma *et al.*, 2011; Shah *et al.*, 2008). These multi-dimensional models are useful for designing the flow fields in the VRFB. A good flow field design creates a uniform distribution of fluid dynamic behavior, which can increase the system efficiency (Xu *et al.*, 2013). The analysis of a multi-dimensional model reported the concentration distribution and electrolyte velocity in the cell during the charging-discharging process in a single cycle (Oh *et al.*, 2015). Due to the complexity of the multi-dimensional model, it is difficult to monitor the performance during long-term operation. In addition, computational power and times were employed to simulate a large-scale VRFB. To study the capacity fade and enable extended VRFB cycling, a zero-dimensional or lumped system model was developed by reducing the dimensionality while capturing the necessary key physics (Boettcher *et al.*, 2016). The capacity prediction plays a significant role in scheduling electrolyte regeneration (rebalancing methods) to recover capacity loss (Tang *et al.*, 2011). However, the existing lumped model does not include the effects of the gassing side reactions and ionic diffusion through the membrane for long-term performance analysis and capacity prediction. In addition, the vanadium electrolyte of the VRFB is circulated during the charging-discharging process. As the electrolyte flow affects both the system performance and operational costs, determination of the optimal flow rate of the vanadium electrolyte becomes important.

The objective of this study is to investigate the performance of a VRFB taking the electrolyte imbalance into consideration. A dynamic model of the VRFB based on mass balances and including an electrochemical kinetic model with the gassing side reaction and a vanadium ionic diffusion model is developed. The model is validated with the experimental data recorded for the VRFB cell (Ngamsai and Arpornwichanop, 2015c). Subsequently, the effects of the operating parameters (applied current,

vanadium and acid concentrations, temperature and electrolyte flow rate) on the battery performance and capacity degradation are analyzed to establish the appropriate operating parameters for battery efficiency and long-term performance. The optimal operating flow rate of the electrolyte is determined by solving the dynamic optimization problem with the aim to maximize the system energy efficiency, considering both the system energy consumption and the rate of cell capacity reduction due to electrolyte imbalance. The performance of the optimal flow rate is compared with the conventional variable flow rate control under the effect of different electrolyte imbalance level. The state estimator is integrated into the proposed dynamic optimization for tracking the variation of vanadium concentration and updating the initial condition in the solving algorithm. An on-line optimization approach is performed in order to modify a new optimal profile of electrolyte flow rate to consist with the actual current profile.

1.2 Research objective

1.2.1 To study and analyze the effect of an electrolyte imbalance on the performance and capacity of a vanadium redox flow battery (VRFB) in a long-term operation.

1.2.2 To determine the optimal operating flow rate of electrolyte during the charging-discharging processes for maximizing the VRFB system efficiency.

1.3 Scope of research

1.3.1 The mathematic model of VRFB is developed taking into account the effects of gassing side reaction and vanadium ions moving across the membrane.

1.3.2 The developed model is validated with the experimental data of charge-discharge characteristics in a unit cell of VRFB (Ngamsai and Arpornwichanop, 2015a). The lab-scale VRFB was conducted using a GFD 4.6 felts (SGL) and an APS-4 Selemon as the electrode and proton exchange membrane, respectively. A single cell was connected to a 250 mL of electrolyte tank.

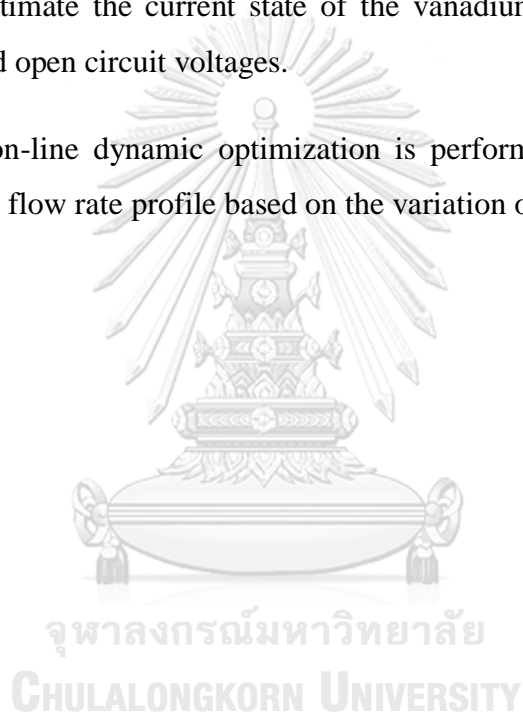
1.3.3 Simulations based on the developed model is performed in MATLAB to evaluate the efficiency and capacity of the VRFB as a function of time. The studied

parameters are current density, vanadium and acid concentration, temperature and electrolyte flow rate.

1.3.4 The optimal electrolyte flow rate of both half-cells is considered as the decision variable in the dynamic optimization problem to maximize the system energy efficiency and the performance of the VRFB using an optimal flow rate of electrolyte is compared with that with conventional variable flow rate control.

1.3.5 An extended Kalman filter is proposed and integrated with the dynamic optimization to estimate the current state of the vanadium ions concentration from measured modified open circuit voltages.

1.3.6 An on-line dynamic optimization is performed to determine the new optimal electrolyte flow rate profile based on the variation of current density.



CHAPTER II

THEORIES

2.1 Principle of electrochemistry

2.1.1 Definitions

An electrochemical system always consists of two electrodes connected via an electronic conductor and each electrode separated by an electrolyte which is the ions medium for moving from one electrode to the other but blocks movement of electrons. The electrical circuit is completed by the electron moving from the electrode which the oxidation reaction take places to reduction reaction at the other electrode through the external conductor. However, the system can be a doing work system which can extract the energy or requiring work system which the energy is needed to input depending on each process known as galvanic cell or electrolytic cell respectively.

The electrode is a material that electrons are the moving species and can be used for controlling the potential of electrons. The electrode can be a metal or other electronic conductor such as carbon, transition-metal chalcogenides, alloy or intermetallic compound and semiconductor. In particular of electrochemical systems, the electrode is used as the electronic conductor which carries out the electrochemical reaction or some similar interaction with an adjacent phase. Generally, the electronic conductivity of electrode decreases slightly with increasing temperature and is of order 10^2 to 10^4 S cm⁻¹, where a siemen (S) is an inverse ohm.

The electrolyte is a component that the moving species are ions and free electrons is blocked. The electrolyte is considered to be an ionic conductor which are molten salts, dissociated salts in solution, and some ionic solids. The term “species” is referred to the ions as well as neutral molecular components that do not dissociated. Normally, the ionic conductivity increases with an increase of temperature and is order 10^{-4} to 10^{-1} S cm⁻¹, although it can be substantially lower. Moreover, some materials are mixed conductors in which charge can be transported by both electrons and ions, for example in solid-oxide fuel cells.

The primary difference between an electrochemical reaction and a chemical redox reaction is that, in electrochemical reaction, the reduction takes place at one electrode and oxidation take place at the other thus the complete redox reaction is separated into two half-cells, and in a chemical redox reaction, both of reduction and oxidation take place on the same electrode. Additionally, the rate of electrochemical reaction can be controlled by externally applied potential different between two half-cell and the derivation of the potential from the equilibrium conditions caused by the passed current is called “polarization”. The electrochemical reactions are always heterogeneous reaction occurring at the interface between electrode surface and electrolyte solution. Occasionally, the electrochemical reaction carries out at the third phase such as a gaseous or insulating reactant.

The relation between the current to the reaction can be explain by the Faraday’s law which states that the production rate of a species is proportion to the current, and the total mass produced is proportional to the amount of charge passed multiplied by the molecular weight of the species according to Eq. (2.1)

$$m_i = -\frac{s_i M_{w,i} It}{nF} \quad (2.1)$$

$$\frac{dN_i}{dt} = \frac{s_i I}{nF} \quad (2.2)$$

where m_i is the mass of species i produced by a reaction, s_i is the stoichiometric coefficient, n is the number of electron transferred, $M_{w,i}$ is the molecular weight of species i , F is Faraday’s constant, equal to 96487 coulombs s^{-1} , I is the applied or extract current depend on charge or discharge process and t is the time that the systems is carried out. On the other hand, Eq. (2.1) can be written as the term of variation of mole per unit time as the Eq. (2.2) that usefully describing the mole or concentration variation by the current when the system is considered as the zero-dimension.

2.1.2 Overpotential and actual cell voltage

The potential difference between two electrodes depends on four components which are the equilibrium potential or open circuit voltage (OCV), the activation overpotential or activation loss (η_{act}), the concentration overpotential or concentration loss (η_{con}) and the ohmic overpotential or ohmic loss (η_{ohm}). The correlation of four potentials make the calculation of the total cell potential or cell voltage which more complicated than the only considering in ohmic overpotential. The OCV represents the maximum work that can be obtained from the system while the cell voltage represents the actual one. The cell potential differs from the open circuit voltage because the passage of current has induced overpotential and all of the overpotentials represent the voltage losses.

2.1.2.1 Surface or activation overpotential

A driving force is required to force an electrochemical reaction to take place at the electrode is the term of surface overpotential or activation loss (η_{act}) and the rate of reaction relates to the surface overpotential (i), which has the form according to Eq. (2.3) (Newman and Thomas-Alyea, 2012).

$$i = i_{0,electrode} \left[\exp\left(\frac{\alpha_a F}{RT} \eta_{act,electrode}\right) - \exp\left(-\frac{\alpha_c F}{RT} \eta_{act,electrode}\right) \right] \quad (2.3)$$

A positive $\eta_{act,electrode}$ produces a positive current (anodic) that represents the first term of Eq. (2.3) while negative $\eta_{act,electrode}$ produces a negative current (cathodic) representing by the second term. The parameter $i_{0,electrode}$ is called the exchange current density which is analogous to the rate constant in chemical reaction. The exchange current density changes with the composition of the electrolyte adjacent to the electrode surface, temperature and the nature of the electrode-electrolyte interface and impurities contaminating on the surface. The magnitude of exchange current density is of order 1 mA cm⁻² to less than 10⁻⁷ mA cm⁻². The parameters α_a and α_c are called apparent transfer coefficients (anodic and cathodic transfer coefficient) which are kinetic

parameters that explain how an applied potential favors one direction of reaction over the other.

2.1.2.2 Ohmic overpotential

The ohmic overpotential or ohmic resistance represents the resistance to ionic or electronic current such as the resistance of electrode, current collector, electrolyte and other cell components for example, the moving resistance of ions in electrolyte and moving resistance of electrons through the electrode and current collectors. The resistance of electrode and current collector depend on the types of their material and the operating temperature of the system. During operating in charge-discharge process, if the current passed dose not constant, the ohmic resistance changes with the current variation through the system according to the Ohm's law expressing in Eq. (2.4). In additional, the electrochemical system using the porous electrode, the porosity of electrode also affects the ohmic resistance that decreasing the electrode porosity can lead to increase in bulk conductivity and decrease in the rates of gassing side reactions (Shah *et al.*, 2008).

$$\eta_{\text{ohm}} = IR_{\text{ohm}} \quad (2.4)$$

2.1.2.3 Concentration overpotential

The potential difference between the bulk of electrolyte and the electrode surface resulting from a concentration gradient of that area which can be referred to a concentration overpotential. The active species mass transfer limit affects the magnitude of concentration overpotential and is dominant at high or low stage of charge that the concentrations of reactant species in oxidation and reduction reactions are low. Thus, the rate of electrochemical reaction at the electrode surface is controlled by diffusion layer created from the mass transfer limit (Tang *et al.*, 2014). The concentration overpotential can be explained by Nernst's equation according to Eq. (2.5).

$$\eta_{\text{conc}} = \frac{RT}{nF} \ln \left(\frac{C_{\text{surface}}}{C_{\text{bulk}}} \right) \quad (2.5)$$

where C_{surface} and C_{bulk} are the concentration of active species at the electrode surface and bulk electrolyte, respectively. The rate of mass transfer of active species into the electrode surface can be described by Fick's law for determining the diffusion rate, thus the reaction current density can be expressed by Eq. (2.6).

$$i = nFD \left(\frac{C_{\text{bulk}} - C_{\text{surface}}}{\delta} \right) \quad (2.6)$$

which δ is the diffusion layer thickness and D is the diffusion coefficient. The limiting current (i_{lim}) is the maximum current that reactant species can be supplied to an electrode surface, and it takes place when concentration of active species at electrode surface depleted. The limiting current can be calculated by Eq. (2.7).

$$i_{\text{lim}} = nFD \frac{C_{\text{bulk}}}{\delta} \quad (2.7)$$

Therefore, the potential different caused by a concentration gradient can be calculated by Eq. (2.8).

$$\eta_{\text{conc}} = \frac{RT}{nF} \left(1 - \frac{i}{i_{\text{lim}}} \right) \quad (2.8)$$

For galvanic cell, the actual cell voltage (V) during passing of current will always be less than the open circuit voltage, while for electrolytic cell the actual cell voltage will be greater which can be described by Eqs. (2.9) and (2.10), respectively.

For galvanic cell:

$$V = E^{\text{OCV}} - (\eta_{\text{act}} + \eta_{\text{ohm}} + \eta_{\text{conc}}) \quad (2.9)$$

For electrolytic cell:

$$V = E^{\text{OCV}} + (\eta_{\text{act}} + \eta_{\text{ohm}} + \eta_{\text{conc}}) \quad (2.10)$$

2.2 Cell components of vanadium redox flow battery

The basic components of an electrochemical system of VRFB are (1) an end plate, (2) a current collector, (3) a flexible graphite foil, (4) a graphite block, (5) a flow field, (6) a graphite felt electrode, and (7) an ion exchange membrane; the arrangement of these cell components is shown in Figure 2.1.

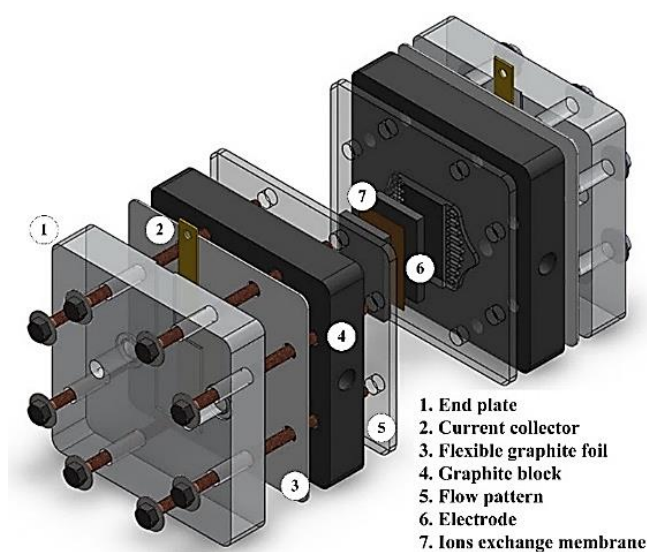


Figure 2.1 Cell components and their arrangement of single VRFB cells.

2.2.1 Current collector

The materials used for current collector in VRFB are graphite and conductive carbon plates due to the resistibility of corrosion from strong acid solution in electrolyte and inertia of redox reaction (Skylas-Kazacos and McCann, 2015). The design of current collector should have a good conductivity for electricity which depends on the thickness of the current collector. The suitable thickness must be determined because if the thickness of plate is too high, the cell stack is large size and weight; however, if the plate is too thin, the cells have a chance to break.

2.2.2 Flexible graphite foil

The main characteristic of this plate is a chemical resistance, compatible with most corrosive chemicals and reduce the contact resistance between the current collector and graphite plate.

2.2.3 Graphite block

This block has a 2 main proposes as follow 1. Graphite block acts as a conductor by transfer the energy between electrode and current collector 2. It uses as the guide flow of electrolyte at inlet and outlet of cell.

2.2.4 Flow field

The flow field is an important component in VRFB because it affects the distribution of active species. The uniformly distribution of the active species causes the decreasing of the concentration overpotential.

2.2.5 Electrode

Electrode and membrane materials are the main components affecting the efficiency and life cycle of the VRFB system as they directly affect the electrolyte imbalance. The material for using as electrode must show a good electrochemical activity for the active species in a redox reaction, low electrochemical activity for side reaction such as gassing side reactions, and good stability during operating at high voltage. Since the electrolyte used in VRFB cells is obtained by dissolving vanadyl sulfate in sulfuric acid, which is a highly acidic electrolyte, most metals corrode during the operating vessel. Consequently, the choice of the electrode material is very limited. In the mid-1980s, the UNSW researcher group investigated a material that could be used as both the positive and negative electrodes. Graphite and carbon felts were considered as the most suitable materials for both half-cell electrodes because of their ability to protect cells during excessive overcharge, chemical and mechanical stability, and high effective areas.

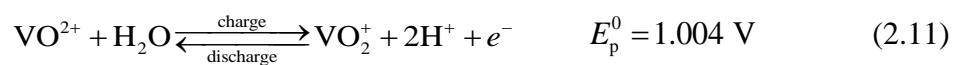
2.2.6 Membrane

Before selecting an appropriate membrane material, it must be noted that the main role of the membrane is the prevention of short circuit between electrodes and allow the transfer of active species for balancing the charge. Generally, ion exchange membranes are classified into the anion exchange membrane, which allows the transfer of negative ions, and the cation exchange membrane, which allows the transfer of positive ions; however, they must have low resistivity to reduce the ohmic loss in the cells, low permeability of vanadium ions, and good stability under highly oxidizing environment in the positive half-cell. But, the major obstacle in the commercialization of VRFB is the limited availability of low-cost and chemically stable electrodes and ion exchange membranes (Skyllas-Kazacos and McCann, 2015).

2.3 Operation of vanadium redox flow battery

All vanadium redox flow batteries utilize redox couple reactions in both positive and negative half-cells [Eqs. (2.11) and (2.12)]. During the charging process, the oxidation of VO^{2+} ions [Eq. (2.11)] occurs in the positive half-cell and this reaction produces electrons and protons. The electron moves from the positive electrode through the external circuit to the negative electrode, and the proton diffuses from the positive half-cell through the membrane to the other half-cell. The redox reaction is completed when the negative half-cell receives the electron from the positive half-cell for reduction of V^{3+} ions [Eq. (2.12)]. During the discharging process, the redox reaction takes place in a reverse manner of the charging process; the oxidation of V^{2+} ions occurs in the negative half-cell, providing the electron for the reduction of VO_2^+ ions in positive half-cells. The flow direction of the proton is the same as the direction of the moving electron. Because of electron mobility, the electrical current flows through the external circuit; the direction of this electrical current is opposite to that of the moving electron. The mechanism of the redox reaction during the charging-discharging process is shown in Figure 2.2.

Positive half-cell reaction



Negative half-cell reaction

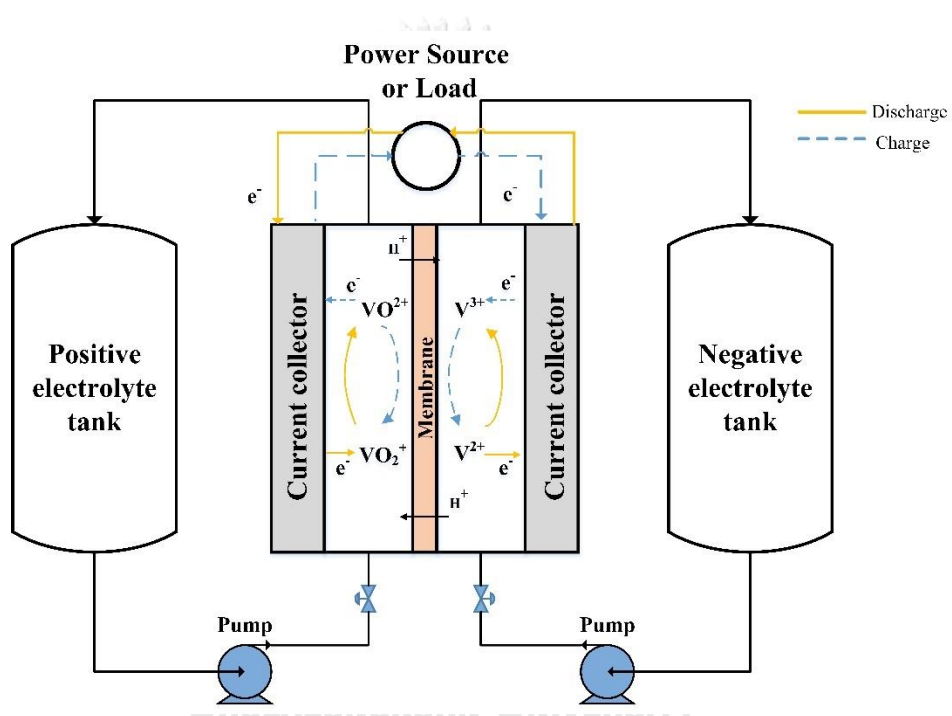


Figure 2.2 Schematic and mechanism of redox reaction in a VRFB system.

2.4 Side reaction and capacity loss

During charging-discharging process, the diffusion of vanadium ions from one half-cell to the other occur since there is a concentration gradient between two half-cells. Furthermore, the diffusing ions go to react with the vanadium ions in another half-cell leading to the self-discharge reaction (Tang *et al.*, 2011) according to Eqs. (2.13)-(2.16). The capacity of battery loss due to the increase of vanadium ions in one half-cell and decrease in the other causing an unequal ratio of reduction and oxidation species.



The gassing side reactions occur when the half-cell electrode potential is higher than the standard potential of the side reactions. The oxygen evolution reaction (OER) and the hydrogen evolution reaction (HER) are the gassing side reactions that occur in positive and negative electrode, respectively. The mechanism of gassing side reactions is presented by Eqs. (2.17) and (2.18). If 1% of the applied current is consumed by the HER during each charging cycle, this will lead to a 1% loss of capacity each cycle (Skyllas-Kazacos and McCann, 2015). The air oxidation of V^{2+} ion will reduce the concentration of V^{2+} according to Eq. (2.19). This reaction will derogate the ratio of V^{2+} and VO_2^+ redox couple in the charging process, as a result the discharge capacity is limited by the amount concentration of V^{2+} ion. The unequal in the amount of reduced species in one side of half-cell and the amount of oxidized species in another half-cell is the electrolyte imbalance problem.

Hydrogen evolution



Oxygen evolution



Air oxidation



2.5 Kalman filter

The target of the filter is to obtain the defective information for sorting out the useful data and reducing the uncertainty or noise from measurement. For example, the low-pass filter is used to allow the low frequency signals to pass though while removing high frequency signals. Kalman Filter or linear quadratic estimation is one of the filter technics that takes in the information including some error, uncertainty or noise.

2.5.1 Kalman filter Algorithm

Kalman filter is an algorithm using a series of measurement observed data from the system containing the noise and uncertainty for filtering the noisy measurement and estimating the unknown variable or parameter that could not directly measure from the process. This method required the mathematical model for calculation which consist of process [Eq. (2.20)] and measurement equation [Eq. (2.21)]. The variable in Kalman filter algorithm were summarized in Table 2.1.

$$\mathbf{x}_k = \mathbf{A}_{k-1}\mathbf{x}_{k-1} + \mathbf{B}_{k-1}\mathbf{u}_{k-1} + \mathbf{w}_{k-1} \quad (2.20)$$

$$\mathbf{y}_k = \mathbf{C}_k\mathbf{x}_k + \mathbf{v}_k \quad (2.21)$$

The algorithm uses two steps process, prediction step and correction step, for estimation the desired variable by recursive calculation.

In prediction step, the filter will project forward the next state and the state error covariance will be. First, the predicted state vector is determined by the state space model.

$$\hat{\mathbf{x}}_{k|k-1} = \mathbf{A}_{k-1} \hat{\mathbf{x}}_{k-1} + \mathbf{B}_{k-1} \mathbf{u}_{k-1} \quad (2.22)$$

where $\hat{\mathbf{x}}_{k|k-1}$ is the predicted state vector from the previous estimated state vector ($\hat{\mathbf{x}}_{k-1}$). \mathbf{A} and \mathbf{B} are the system matrixes of state and input, while \mathbf{u}_{k-1} is the input vector. The subscript $k|k-1$ means the expected value at time k based on the previous value at discrete time $k-1$. Secondly, the state error covariance matrix is determined using

$$\mathbf{P}_{k|k-1} = \mathbf{A}_{k-1} \mathbf{P}_{k-1} \mathbf{A}_{k-1}^T + \mathbf{Q}_{k-1} \quad (2.23)$$

where $\mathbf{P}_{k|k-1}$ is the predicted state error covariance matrix from the previous state error covariance matrix (\mathbf{P}_{k-1}), and \mathbf{Q}_{k-1} is the process noise covariance matrix.

In correction step, firstly, the Kalman gain matrix at discrete time k (\mathbf{K}_k) is calculated by

$$\mathbf{K}_k = \mathbf{P}_{k|k-1} \mathbf{C}_k^T (\mathbf{C}_k \mathbf{P}_{k|k-1} \mathbf{C}_k^T + \mathbf{R}_k)^{-1} \quad (2.24)$$

where \mathbf{C}_k is the observer matrix for defining the output value from predicted state and \mathbf{R}_k is the measurement noise covariance. Next, the state vector is then updated by scaling the difference between the predicted output ($\hat{\mathbf{y}}_{k|k-1}$ or $\mathbf{C}_k \mathbf{x}_{k|k-1}$) and measured output from the process (\mathbf{y}_k) with the Kalman gain matrix according to Eq. (2.25). Finally, the state error covariance matrix is updated by Eq. (2.26).

$$\hat{\mathbf{x}}_k = \hat{\mathbf{x}}_{k|k-1} + \mathbf{K}_k (\mathbf{y}_k - \mathbf{C}_k \hat{\mathbf{x}}_{k|k-1}) \quad (2.25)$$

$$\mathbf{P}_k = (\mathbf{I} - \mathbf{K}_k \mathbf{C}_k) \mathbf{P}_{k|k-1} \quad (2.26)$$

Table 2.1 Dimension of discrete time system variables for Kalman filter algorithm.

Variable	Description	Dimension
x	State vector	$n_x \times 1$
y	Output vector	$n_y \times 1$
u	Input vector	$n_u \times 1$
w	Process noise vector	$n_x \times 1$
v	Measurement noise vector	$n_y \times 1$
A	State system matrix	$n_x \times n_x$
B	Input system matrix	$n_x \times n_u$
C	Observer matrix	$n_y \times n_x$
P	State error covariance matrix	$n_x \times n_x$
Q	Process noise covariance matrix	$n_x \times n_x$
R	Measurement noise covariance matrix	$n_y \times n_y$

The Kalman filter is used for operating on linear state space system. However, if the system is non-linear systems which the state and/or output containing the non-linear function [Eqs. (2.27) and (2.28)], the extended Kalman filter (EKF) is used for handling with the non-linear system. The EKF is similar to the KF, but the values of state matrix (A) and observation matrix (C) are determined by Jacobian matrix at each time step. Moreover, the non-linear functions of state (f) and measurement (h) are directly used in the prediction step of states and outputs, rather than use the linearized format.

$$\mathbf{x}_k = \mathbf{f}(\mathbf{x}_{k-1}, \mathbf{u}_{k-1}) + \mathbf{w}_{k-1} \quad (2.27)$$

$$\mathbf{y}_k = \mathbf{h}(\mathbf{x}_k) + \mathbf{v}_k \quad (2.28)$$

Table 2.2 Comparison of the equation set between KF and EKF

Kalman filter (KF)	Extended Kalman Filter (EKF)
<i>Prediction step</i>	<i>Prediction step</i>
1. $\hat{\mathbf{x}}_{k k-1} = \mathbf{A}_{k-1}\hat{\mathbf{x}}_{k-1} + \mathbf{B}_{k-1}\mathbf{u}_{k-1}$	1. $\hat{\mathbf{x}}_{k k-1} = f(\hat{\mathbf{x}}_{k-1}, \mathbf{u}_{k-1})$
2. $\mathbf{P}_{k k-1} = \mathbf{A}_{k-1}\mathbf{P}_{k-1}\mathbf{A}_{k-1}^T + \mathbf{Q}_{k-1}$	2. $\mathbf{P}_{k k-1} = \mathbf{A}_{k-1}\mathbf{P}_{k-1}\mathbf{A}_{k-1}^T + \mathbf{Q}_{k-1}$
	where $\mathbf{A}_k = \left. \frac{\partial f}{\partial \mathbf{x}} \right _{\hat{\mathbf{x}}_{k-1}}$
<i>Correction step</i>	<i>Correction step</i>
3. $\mathbf{K}_k = \mathbf{P}_{k k-1}\mathbf{C}_k^T(\mathbf{C}_k\mathbf{P}_{k k-1}\mathbf{C}_k^T + \mathbf{R}_k)^{-1}$	3. $\mathbf{K}_k = \mathbf{P}_{k k-1}\mathbf{C}_k^T(\mathbf{C}_k\mathbf{P}_{k k-1}\mathbf{C}_k^T + \mathbf{R}_k)^{-1}$
4. $\hat{\mathbf{x}}_k = \hat{\mathbf{x}}_{k k-1} + \mathbf{K}_k(\mathbf{y}_k - \mathbf{C}_k\hat{\mathbf{x}}_{k k-1})$	4. $\hat{\mathbf{x}}_k = \hat{\mathbf{x}}_{k k-1} + \mathbf{K}_k[\mathbf{y}_k - \mathbf{h}(\hat{\mathbf{x}}_{k k-1})]$
5. $\mathbf{P}_k = (\mathbf{I} - \mathbf{K}_k\mathbf{C}_k)\mathbf{P}_{k k-1}$	5. $\mathbf{P}_k = (\mathbf{I} - \mathbf{K}_k\mathbf{C}_k)\mathbf{P}_{k k-1}$
	where $\mathbf{C}_k = \left. \frac{\partial \mathbf{h}}{\partial \mathbf{x}} \right _{\hat{\mathbf{x}}_{k k-1}}$

2.5.2 Observability

A necessary condition of Kalman Filter is the system which the states are to be estimated by the measurement variables is known as observability. Thus, the applying of Kalman Filter must be confirmed that the system has an observability. The system described by Eqs. (2.27) and (2.28) are observable if the observability matrix (\mathbf{M}_{obs}) has rank equal to n where n is the number of state variables.

$$\mathbf{M}_{\text{obs}} = \begin{bmatrix} \mathbf{C} \\ \mathbf{CA} \\ \vdots \\ \mathbf{CA}^{n-1} \end{bmatrix} \quad (2.29)$$

The rank of matrix can be calculated by find the determinant of M_{obs} . If the determinant is non-zero, the rank is full so, this system is observable. On the other hand, if the determinant is zero, his system is non-observable. For example, the state space model is given as follow:

$$\begin{bmatrix} x_{1,k} \\ x_{2,k} \end{bmatrix} = \begin{bmatrix} 1 & a \\ 0 & 1 \end{bmatrix} \begin{bmatrix} x_{1,k-1} \\ x_{2,k-1} \end{bmatrix} + \begin{bmatrix} 0 \\ 1 \end{bmatrix} u_{k-1} \quad (2.30)$$

$$y_k = [C_1 \quad 0] \begin{bmatrix} x_{1,k} \\ x_{2,k} \end{bmatrix} + [0] u_k \quad (2.31)$$

The observability matrix is (n=2)

$$M_{\text{obs}} = \begin{bmatrix} C \\ CA^{2-1} = CA \end{bmatrix} = \begin{bmatrix} [c_1 \quad 0] \\ [c_1 \quad 0] \begin{bmatrix} 1 & a \\ 0 & 1 \end{bmatrix} \end{bmatrix} = \begin{bmatrix} c_1 & 0 \\ c_1 & ac_1 \end{bmatrix} \quad (2.32)$$

The determinant of M_{obs} is

$$\det(M_{\text{obs}}) = c_1 \cdot ac_1 - c_1 \cdot 0 = ac_1^2$$

The system is observable only if $ac_1^2 \neq 0$. For example, if $a \neq 0$ which means that the state variable (x_1) has a correlation with the state variable (x_2), the system is observable if $c_1 \neq 0$ which means that the measurement variable (y) contains the information about (x_1). Meanwhile, if $a = 0$, the system is non-observable although the state variable (x_1) is measured.

2.5.3 Tuning of Kalman Filter

The selection of the covariance matrixes P_0 , Q and R have an effect on the state estimation performance of Kalman filter. The initial P_0 affect the initial convergence of the filter, however it is often arbitrary initialized to an identity matrix for simplicity. The selection of Q and R is more significantly affect the filter performance since the Q and R matrixes are weighting factor of the reliability between the predicted state equations [Eq. (2.27)] and the measurement equation [Eq. (2.8)]. Since the Kalman gain in Eq. (2.24) is calculated based on the value of P and R matrix, the matrix P increase with an increase of matrix Q as presented in Eq. (2.23). For the example, a larger Q is equal to a larger uncertainly in the state equation which means the prediction does not trust the result from model and the filter will trust with the value from measurement update [Eq. (2.33)]. Similarly, a larger R is equal to a larger uncertainty in the measurement value and the filter will trust the value calculated by the model [Eq. (2.34)].

$$\begin{aligned}\lim_{R \rightarrow 0} K_k &= \lim_{R \rightarrow 0} \frac{P_{k|k-1} C^T}{C_k P_{k|k-1} C^T + R} = \frac{1}{C_k} = C_k^{-1} \\ \hat{x}_k &= \hat{x}_{k|k-1} + C_k^{-1} (y_k - C_k \hat{x}_{k|k-1}) \\ &= \hat{x}_{k|k-1} + C_k^{-1} y_k - C_k^{-1} C_k \hat{x}_{k|k-1} \\ &= C_k^{-1} y_k\end{aligned}\tag{2.33}$$

$$\begin{aligned}\lim_{P \rightarrow 0} K_k &= \lim_{P \rightarrow 0} \frac{P_{k|k-1} C^T}{C_k P_{k|k-1} C^T + R} = \frac{1}{R} = 0 \\ \hat{x}_k &= \hat{x}_{k|k-1} + 0 \cdot (y_k - C_k \hat{x}_{k|k-1}) \\ &= \hat{x}_{k|k-1}\end{aligned}\tag{2.34}$$

2.6 Dynamic optimization

The purpose of dynamic optimization problem is the determination of the optimal control variable as a function of time to minimize or maximize the objective function according to the process constraints. The optimal control profile will drive the process system in the optimal way from the initial to final state. The techniques for solving the dynamic optimization can be considered as the variation approach and discretization approach. However, to understand the algorithm, in this part, the basic for solving the optimization was proposed. The optimal control problem could be classified as the static optimization and dynamic optimization. As seen, the objective function of the static optimization is function, while the dynamic optimization is functional. For function, the dependent variable (y) is a function of independent variable (x) and the value of y can calculate through the relationship of the function (f). For functional, the value of functional (J) depends on the function of $x(t)$; thus if function of $x(t)$ changes, the value of functional also modify with the variation of $x(t)$ as presented in Table 2.4

Table 2.3 Comparison of static and dynamic optimization

Static optimization	Dynamic optimization
$\min_{x,u}(\text{or max}) F(x,u)$	$\min_{u(t)}(\text{or max}) J(x(t),u(t),t)$
subject to	subject to
$f(x,u) = 0$	$\frac{dx}{dt} = f(x(t),u(t),t)$
$x_{\min} \leq x \leq x_{\max}$	$x_{\min} \leq x(t) \leq x_{\max}$
$u_{\min} \leq u \leq u_{\max}$	$u_{\min} \leq u(t) \leq u_{\max}$

Table 2.4 Comparison of function and functional

Function	Functional
$y = f(x)$	$J(x(t)) = \int_0^1 (x(t)) dt$
$y = x^3 + 1$	
if $x = 1 \rightarrow y = 2$	if $x(t) = 2t^2 + 1 \rightarrow J = \int_0^1 (2t^2 + 1) dt$
	$\left. \frac{2}{3} t^3 + t \right _0^1 = \frac{2}{3} + 1 = \frac{5}{3}$

Moreover, the method for calculating the optimum of function and functional were discussed. To find the optimum of function, x^* is defined as the local minimum point for all of x in the range of ε around the x^* when $f(x^*) \leq f(x)$; thus the problem can formulated in term of increment of function (Δf) and is approximated by Taylor series as follow.

$$\begin{aligned}
 f(x^*) &\leq f(x^* + \delta x) \\
 f(x^* + \delta x) - f(x^*) &\geq 0 \\
 \Delta f &= f(x^* + \delta x) - f(x^*) \\
 &= f(x^*) + \left. \frac{\partial f}{\partial x} \right|_{x=x^*} \cdot \delta x + \frac{1}{2} \delta x^T \left. \frac{\partial^2 f}{\partial x^2} \right|_{x=x^*} \cdot \delta x + 0(\delta x^2) - f(x^*) \\
 &= \left. \frac{\partial f}{\partial x} \right|_{x=x^*} \cdot \delta x + \frac{1}{2} \delta x^T \left. \frac{\partial^2 f}{\partial x^2} \right|_{x=x^*} \cdot \delta x \\
 \left. \frac{\partial f}{\partial x} \right|_{x=x^*} \cdot \delta x + \frac{1}{2} \delta x^T \left. \frac{\partial^2 f}{\partial x^2} \right|_{x=x^*} \cdot \delta x &\geq 0
 \end{aligned} \tag{2.35}$$

Thus, the necessary (N.C.) and sufficient condition (S.C.) causing the x^* is local minimum point are $\left. \frac{\partial f(x)}{\partial x} \right|_{x=x^*} = 0$ and $\left. \frac{\partial^2 f(x)}{\partial x^2} \right|_{x=x^*} > 0$, respectively. Similarly, the optimum of functional can be defined in the term of increment of functional (ΔJ) and $x^*(t)$ is the optimal function as the variation of functional (δJ) is equal to 0. Table 2.5 shows comparison of the solution of static and dynamic optimization.

Table 2.5 Comparison of the solution of static and dynamic optimization

Static optimization	Dynamic optimization
Function: $y = f(x)$	Functional: $J = F(x(t))$
Increment of function: $\Delta f = f(x + \delta x) - f(x)$	Increment of functional $\Delta J = J(x(t) + \delta x(t)) - J(x(t))$
Differential of function: $df = f'(x)\Delta x$	Variation of functional $dJ = \left(\frac{dJ}{dx}\right)^T \delta x(t)$
Minimum condition	Minimum condition
N.C. $\left.\frac{\partial f^T(x)}{\partial x}\right _{x=x^*} = 0$	N.C. $\delta J(x^*(t)) = 0$
S.C. $\left.\frac{\partial^2 f(x)}{\partial x^2}\right _{x=x^*} > 0$	S.C. $\delta^2 J(x^*(t)) > 0$

2.6.1 Variation approach for optimal control problem

Since the objective function of the dynamic optimization is a functional, the variation of functional must be defined and the first variation of functional must equal to 0 for the necessary condition. The optimal control problem can be defined as the set of equation presented in Eq. (2.36)

$$\begin{aligned} \min(\text{or max}) \quad J &= \int_{t_0}^{t_f} F(x(t), u(t), t) dt \\ \text{subject to} & \\ \dot{x} &= f(x, u, t) \\ x(t_0) &= x_0 \end{aligned} \tag{2.36}$$

The problem can be changed from constraint optimization to unconstraint optimization problem through the definition of Lagrange function in term of Lagrange multiplier (costate variable, adjoint variable) [Eq. (2.37)] and the cost function is defined as the augmented cost function as Eq. (2.38).

$$L = F(x, u, t) + \lambda^T (f - \dot{x}) \quad (2.37)$$

$$J = \int_{t_0}^{t_f} L(x, \dot{x}, u, \lambda, t) dt \quad (2.38)$$

Then, the increment of function and the first variation of function can be defined as Eqs. (2.39) and (2.40)

$$\Delta J(x, \dot{x}, \lambda, t) = J(x + \delta x, \dot{x} + \delta \dot{x}, \lambda + \delta \lambda, u + \delta u, t) - J(x, \dot{x}, \lambda, u, t) \quad (2.39)$$

$$\begin{aligned} \delta J = \int_{t_0}^{t_f} \left\{ \left(\frac{\partial L}{\partial x} + \frac{d}{dt} \frac{\partial L}{\partial \dot{x}} \right)^T \delta x + \left(\frac{\partial L}{\partial \lambda} \right)^T \delta \lambda + \left(\frac{\partial L}{\partial u} \right)^T \delta u \right\} dt + \left(\frac{\partial L}{\partial \dot{x}}(t_0) \right)^T \delta x(t_0) \\ + \left(\frac{\partial L}{\partial \dot{x}}(t_f) \right)^T \delta x(t_f) + \left[L(t_f) - \left(\frac{\partial L}{\partial \dot{x}}(t_f) \right)^T x(t_f) \right] \delta t_f = 0 \end{aligned} \quad (2.40)$$

As a result, the system contains the set of equation as

$$\text{Euler-Lagrange: } \frac{\partial L}{\partial x} - \frac{d}{dt} \frac{\partial L}{\partial \dot{x}} = 0 \quad (2.41)$$

$$\text{Initial transversality: } \frac{\partial L}{\partial \dot{x}}(t_0) \delta x(t_0) = 0 \quad (2.42)$$

$$\text{Final transversality: } \frac{\partial L}{\partial \dot{x}}(t_f) \delta x(t_f) + \left[L(t_f) - \left(\frac{\partial L}{\partial \dot{x}}(t_f) \right)^T x(t_f) \right] \delta t_f = 0 \quad (2.43)$$

$$\text{Constraint equation: } \frac{\partial L}{\partial \lambda} = 0 \quad (2.44)$$

$$\text{Optimal control equation: } \frac{\partial L}{\partial u} = 0 \quad (2.45)$$

2.6.2 Discretization techniques with sequential approach

The discretization method is a technique for solving the dynamic optimization. This concept of this technique is the transformation of ordinary optimal control problem to nonlinear programming problem through the discretization on either only control variable $u(t)$ or both state $x(t)$ and control variable and this method is classified into sequential and simultaneous approach. The advantage of the sequential approach is that the decision variables in optimization are only the parameters that are used for discretization the control variable. Thus, the optimization formulated by sequential approach becomes a small scale of nonlinear programming and can use for solving the optimal control problem with the large dimension system including the many differential equation. However, since the state variables are not directly considered as the decision variables in optimization, the sequential approach is difficulty method for dealing with a system including a constraint on state variables. The sequential approach can discrete the control variable profile into a piecewise constant, piecewise linear, or piecewise polynomial. For example, the process model is expressed in an ordinary differential equation including set of state variable ($x(t)$) and control vector parameter ($u(t)$) according to Eq. (2.46). For giving the initial condition of state, the optimal control of process starting from to initial state to final state can be determined by calculating the profile of $u(t)$ for minimizing or maximizing an objective function in functional term of Eq. (2.47).

$$\frac{dx}{dt} = f(t, x(t), u(t)) \quad [t_0, t_f] \quad (2.46)$$

$$J = \int_{t_0}^{t_f} F(x(t), u(t), t) dt \quad (2.47)$$

For applying the sequential approach, the time interval $[t_0, t_f]$ is distributed into a number of subinterval (P) and the control variable is divided into the equal the number of subinterval. Since the piecewise constant is used for representing the value of control variable in each subinterval, the dynamic optimization is transformed into nonlinear programming form [Eq. (2.48)] considering the set of control variable [Eq.

(2.49)] as the decision variable subject to the equality constraint, inequality constraint and bounds of control variable.

$$\min_y \text{ (or max) } J(y) \quad (2.48)$$

$$y = \{u_{p1}, u_{p2}, \dots, u_{pn-1}, u_{pn}\} \quad (2.49)$$

The sequential approach computation procedure is presented in Figure 2.3. For giving the initial guess of the decision variables (y), the process model is solving based on integrating method for providing the value of objective function and constraint. Then, the nonlinear programming solver will determine a new set of decision variable and send it back to the model solver and this algorithm is repeated until the set of optimal value is found and consisted with the specified accuracy.

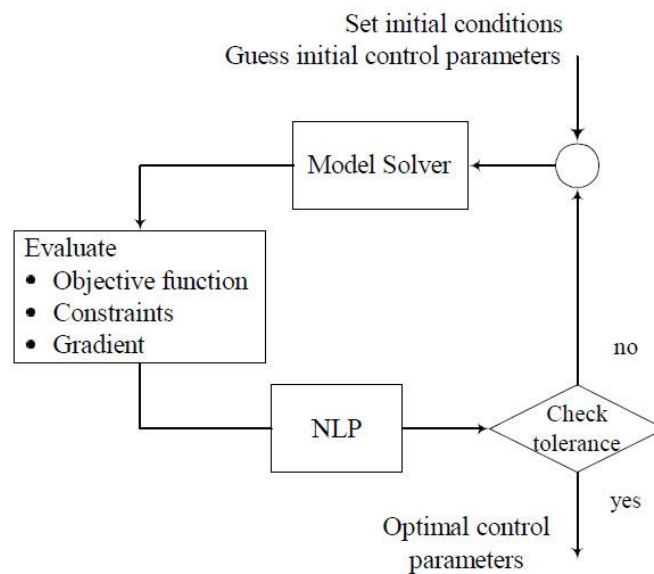


Figure 2.3 Optimal control solution via the sequential approach (Arpornwichanop *et al.*, 2005).

CHAPTER III

LITERATURE REVIEWS

Since the vanadium redox flow battery (VRFB) has become more consideration as the load levelling and peak shaving applications, several researchers worked in development of the VRFB, electrode and membrane improvement, electrolyte flow field design as well as operating and control strategy for practical application. However, during long term operation of VRFB, the performance of electrolyte in system was reported to become imbalance. The electrolyte imbalance refers to an unequal in the amount of reduced species in one side of half-cell and the amount of oxidized species in another half-cell, resulting in capacity loss. The imbalance problem has been studied by many researchers for investigating the parameters and operating condition which may lead to decrease the system efficiency. In addition, the maximum system efficiency could be obtained by solving the optimization problem for optimal operating flow rate determination. To monitor the aging of the battery and determine the optimal operating flow rate. In this chapter, the literature reviews described the causes and effects of electrolyte imbalance, mathematical model development of VRFB for prediction the performance and operating condition of VRFB.

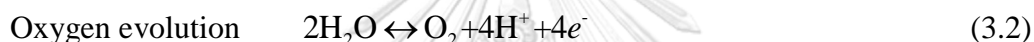
3.1 Causes and effects of an electrolyte imbalance

During long-term operations, the performance of a VRFB electrolyte tends to become unbalanced because of cross-contamination and side reactions. The imbalance of active species between half-cells, resulting in a capacity loss and 100% state of charge, can only be achieved in the half-cell that has the limiting active species in an electrolyte (Roznyatovskaya *et al.*, 2016). Interestingly, the positive or negative half-cell can be the limiting half-cell depending on the causes of the electrolyte imbalance, thereby affecting the variation of the active species concentration in the electrolyte. Thus, an electrolyte imbalance is a significant factor that must be considered in the VRFB control and management system. Moreover, the electrolyte rebalance method is required early in the charging-discharging process when the electrolyte imbalance

occurs. The imbalance can occur for many reasons and their effects deteriorate the battery performance. The causes of the imbalance affecting the battery performance are reported as follow.

3.1.1 Gassing side reactions

In a battery charging process, a side reaction could takes place when the electrode potential is higher than the standard potential of the side reactions. HER and OER take place in the negative and positive electrodes [Eqs. (3.1) and (3.2)], respectively.



The effects of HER and OER were studied using a developed model, including charge, mass and momentum conservation equations (Al-Fetlawi *et al.*, 2010; Shah *et al.*, 2010). The formation of gas bubbles affects the reduction of the liquid electrolyte volume and surface area for the electrochemical reaction, which increase the activation overpotential. Furthermore, the bubbles hinder the flow distribution of the electrolyte in the porous electrode, leading to the reduction of mass and charge transfer; consequently, the concentration overpotential also increased. Moreover, gassing side reactions partially consume the applied current for charging the battery. Therefore, the current for a redox reaction decreased and the time for charging the battery increased, resulting in the reduction of coulombic efficiency. Because the operating temperature also affects the rate of OER, when the operating temperature increases, the rate of oxygen evolution increases and leads to the high consumption of applied current. As a result, the rate of VO^{2+} oxidation reaction in the positive electrode decreases, leading to the imbalance of SOC between half-cells (Al-Fetlawi *et al.*, 2010).

The effect of operating temperature on the gassing side reaction current density also was studied. The result showed that the corrosion current density also increases with the operating temperature, as shown in Figure 3.1a. As a result, the coulombic

efficiency decreased with the increase in the operating temperature (Figure 3.1b) because of the higher consumption of the applied current density for the evolution of O_2 and CO_2 ; this experiment showed that the proposed dynamic model of Al-Fetlawi *et al.* (2010) was consistent with this measurement.

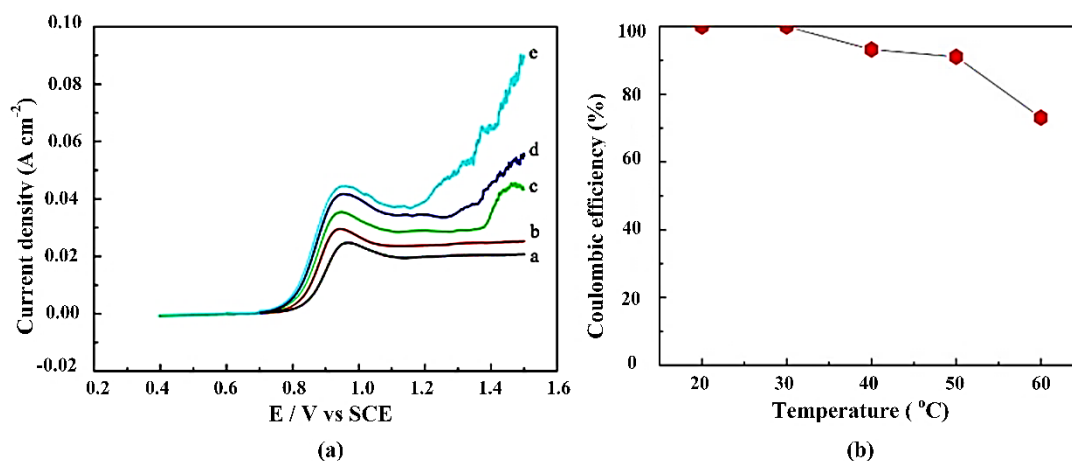


Figure 3.1 (a) Potentiodynamic polarization curves of a graphite electrode from 0.4 to 1.5 V vs SCE at 20–60 °C. (b) Correlation between coulombic efficiency and operating temperature (Liu *et al.*, 2011).

Recently, a study on parasitic hydrogen evolution at different carbon fiber electrodes in VRFB was reported by Schweiss *et al.* (2016). They investigated the effect of four carbon felt electrodes, each with a different fiber precursor and crystallinity, on the hydrogen evolution rate. The kinetics of hydrogen evolution and redox couples reaction were obtained by voltammetric analysis of the carbon felt in sulfuric acid. The hydrogen evolution rate, while charging the VRFB with different carbon felt electrodes, is shown in Figure 3.2. The hydrogen evolution in the carbon felt with a more amorphous structure (F1 and F3) was higher than that in the surface-treated felt (F2 and F4). Moreover, F1 and F3 felt might contain impurities such as a carbide, the catalyst for hydrogen evolution, from the carbonization process. Since the residual nitrogen groups in the PAN-based precursor also acted as the hydrogen evolution catalysts, the carbon precursor of PAN-based (F3) showed a higher rate of hydrogen evolution than rayon-based evolution (F1).

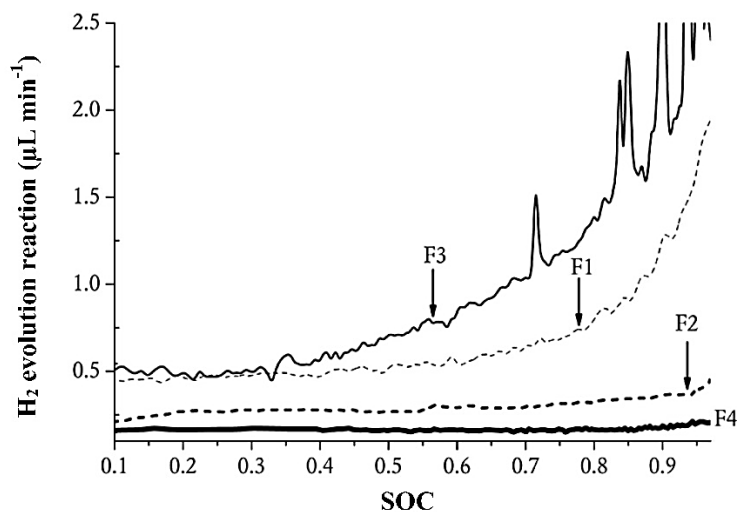


Figure 3.2 Hydrogen evolution rate for all VRFBs employing different carbon felt electrodes (Schweiss *et al.*, 2016).

The effect of HER on a carbon fiber electrode at different temperatures was recently studied by Fetyan *et al.* (2018). Although increasing the operating temperature can enhance the rate of electrochemical reaction in both positive and negative electrodes, the undesired HER also increases with temperature. The effects of the operating temperature on battery voltage at 50% SOC during the charging–discharging process are shown in Figure 3.3a. To increase the temperature, the voltage for charging the battery should be decreased, while the discharge voltage should be increased. This result could be explained by the reduction of activation overpotential due to the increase in the electrochemical rate of the reaction. As a result, the voltage efficiency increased with temperature; however, the coulombic efficiency decreased with the increasing operating temperature. This result could be explained by as follows. The diffusion rate of vanadium ions across the membrane enhanced, which increases the rate of self-discharge reaction; the charging time also increases, while the discharging time decreases. Another reason was that the current applied for charging the battery was consumed by the HER, which also increases the charging time. However, the energy efficiency is enhanced with the operating temperature. Thus, it could be said that the increase in the voltage efficiency was more influential than the reduction in the coulombic efficiency (Figure 3.3b).

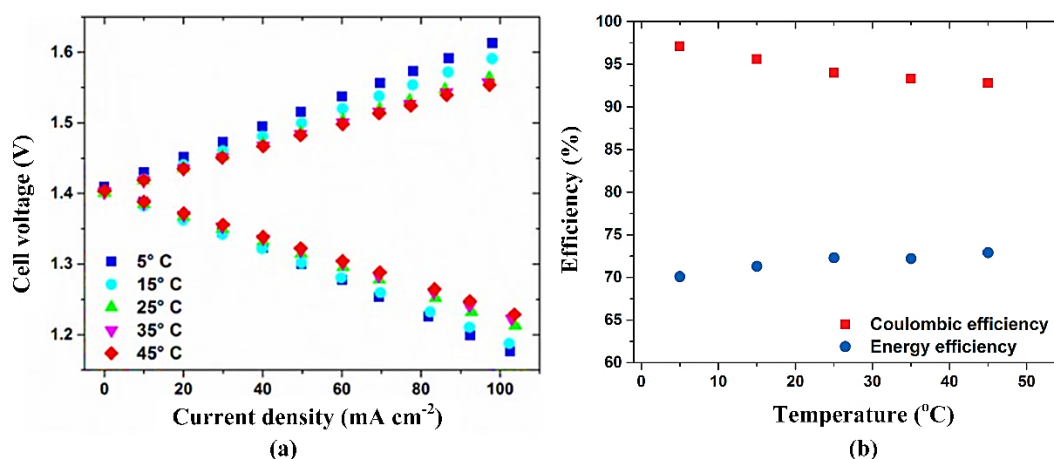


Figure 3.3 Effect of operating temperature on (a) the charge-discharge battery voltage and (b) the coulombic and energy efficiency (Fetyan *et al.*, 2018).

3.1.2 Air oxidation

Air oxidation of vanadium ions (V^{2+}), a side reaction in the negative electrolyte tank, takes place on the interface when the electrolyte is in contact with the air. This side reaction leads to an electrolyte imbalance and a self-discharge process [Eq. (3.3)].



Air oxidation of V^{2+} limits the active species to the negative half-cell because the amount of V^{2+} ions are not consistent with the V^{5+} ions present in the positive half-cell. To study the effect of air oxidation, the electrolyte tank is exposed to the surrounding and a current density of 40 mA cm⁻² is used for charging–discharging (Figure 3.4a). The effect of this phenomena on the battery discharge capacity is presented in Figure 3.4b. It can be noticed that the discharge capacity decreased from 800 to 120 mAh in only 20 cycles. The high rate of capacity degradation may be because of the high air oxidation of V^{2+} in the negative electrolyte tank, which has a large surface area to volume ratio. However, the oxidation of air could be reduced by purging an inert gas into the void volume of the electrolyte tank to cover the electrolyte surface (Tang *et al.*, 2011).

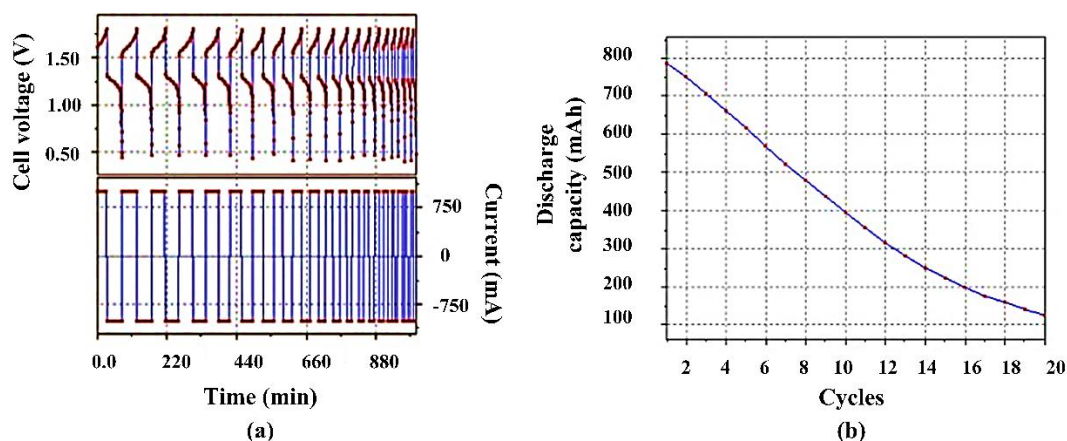


Figure 3.4 (a) Charge-discharge characteristic voltage and current. (b) Discharge capacity (Tang *et al.*, 2011).

To reduce the effect of air oxidation on capacity degradation, an appropriate design of the electrolyte tank and suitable preparation of the electrolyte solution were investigated by Ngamsai and Arpornwichanop (2015b). The effects of three factors—the electrolyte volume to air-electrolyte solution interface area ratio, vanadium concentration, and sulfuric acid concentration—on air oxidation in VRFB were studied. The ratio of the electrolyte volume to the electrolyte surface area exposed to air (which varies from 1.20 to 5.76 cm) was studied. Figure 3.5a showed that a higher ratio of the electrolyte volume to air-electrolyte solution interface area reduces the air oxidation rate, thereby decreasing the self-discharge reaction, converting V^{2+} to V^{3+} ions, and reducing the imbalance between V^{2+} and VO_2^+ ions. Moreover, the composition of the electrolyte solution, vanadium, and sulfuric concentration affect the stability of the electrolyte under air oxidation. To prevent electrolyte precipitation, the effect of vanadium concentration was studied in the range of 1–2 M. Acid concentration was limited between 3 and 5M, because high acid concentration could reduce the solubility of vanadium while increasing the electrolyte viscosity. To increase the acid concentration, the rate of capacity degradation was also decreased (Figure 3.5b). This result could be explained as follows. Firstly, the free ions from sulfuric acid, which are HSO_4^- , SO_4^{2-} and H^+ , act as hindrance ions at the interface. Secondly, many free sulfuric ions could bond with V^{2+} ions and form a vanadium salt (VSO_4 or $V(HSO_4)_2$), which increases the stability of the electrolyte solution. The result shows that as the vanadium concentration increases, the rate of air oxidation could decrease (Figure. 3.5c). Since

V^{3+} ions were increased by using high vanadium concentration, they could reduce the reactive area and hinder the air oxidation of V^{2+} at the electrolyte and air interface. To summarize, the higher concentration of vanadium ions and sulfuric acid also delays the air oxidation of V^{2+} ions and improves the conductivity of electrolyte solution, which can increase the discharge capacity and battery efficiencies.

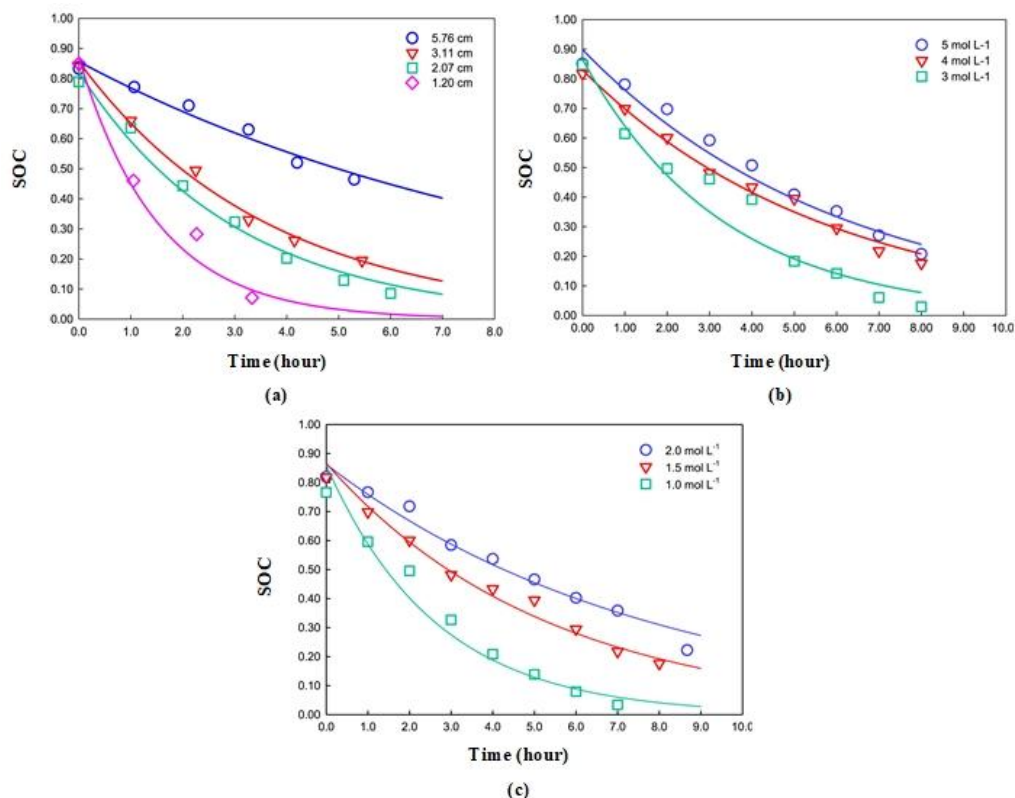


Figure 3.5 Relationship between SOC degradation and reaction time under different (a) volume to air-electrolyte solution interface area ratio, (b) vanadium concentration, and (c) sulfuric concentration (Ngamsai and Arpornwichanop, 2015b).

3.1.3 Ion diffusion

Vanadium ions transfer across a membrane and significantly affect the electrolyte imbalance problem because not only the ions diffuse through the membrane, but self-discharge side reactions also occur after this diffusion. Thus, the electrolyte imbalance rate between two half-cells is increased by a self-discharge reaction leading to capacity loss. If VO^{2+} and VO_2^+ ions diffuse across the membrane and react with V^{2+} and V^{3+} ions in the negative half-cell, the self-discharge reactions take place [Eqs. (3.4) – (3.6)]. On the contrary, if vanadium ions diffuse from the negative to the positive

half-cell, a self-discharge reaction occurs [Eqs. (3.7) – (3.9)]. The ion exchange membrane is the key component that reduces the self-discharge side reaction because the rate of self-discharge side reactions increases with the increase in the total number of vanadium ions diffused across the membrane.

Table 3.1 Self-discharge side reactions in negative and positive half-cells.

Negative half-cell		
Diffused ions into half-cell	Reaction	
VO_2^+	$\text{VO}_2^+ + 2\text{V}^{2+} + 4\text{H}^+ + \text{e}^- \rightarrow 3\text{V}^{3+} + 2\text{H}_2\text{O}$	(3.4)
VO^{2+}	$\text{VO}^{2+} + \text{V}^{2+} + 2\text{H}^+ \rightarrow 2\text{V}^{3+} + \text{H}_2\text{O}$	(3.5)
VO_2^+	$\text{VO}_2^+ + \text{V}^{3+} \rightarrow \text{VO}^{2+}$	(3.6)
Positive half-cell		
Diffused ions into half-cell	Reaction	
V^{2+}	$\text{V}^{2+} + 2\text{VO}_2^+ + 2\text{H}^+ \rightarrow 2\text{VO}^{2+} + \text{H}_2\text{O}$	(3.7)
V^{3+}	$\text{V}^{3+} + \text{VO}_2^+ \rightarrow 2\text{VO}^{2+}$	(3.8)
V^{2+}	$\text{V}^{2+} + \text{VO}^{2+} + 2\text{H}^+ \rightarrow 2\text{V}^{3+} + \text{H}_2\text{O}$	(3.9)

The effects of ion diffusion and self-discharge side reactions on the battery capacity loss were studied by using various models of VRFBs. The dynamic model, first proposed by Tang et al. (2011), describes the concentration change of vanadium ions in the stack during the charging-discharging process and can predict the capacity deterioration from cross contamination problem. Three different types of membrane, Selemion CMV, Selemion AMV, and Nafion 115, were employed in this simulation. The results show that the higher diffusion coefficient for vanadium ions across the membrane increases the rate of capacity degradation. However, in the half-cell, the vanadium concentration build-up not only depends on the magnitude of diffusion coefficient, but also on the relative value of the four diffusion coefficients. For AMV and CMV membranes, the vanadium concentration increased in the positive half-cell

because the high diffusion of V^{2+} ions caused a self-discharge side reaction and increase of vanadium concentration in the positive half-cell. It could be noticed from Figure 3.6b and c (AMV and Nafion 115 membrane) that the vanadium build-up in the half-cell was different, although the order of four diffusion coefficients was similar ($V^{2+} > VO^{2+} > VO_2^+ > V^{3+}$). Moreover, not only the absolute values of different diffusion coefficients were the important factor in determining capacity degradation, but the relative values of these coefficients could also be used for building the half-cell and planning for the regeneration procedure.

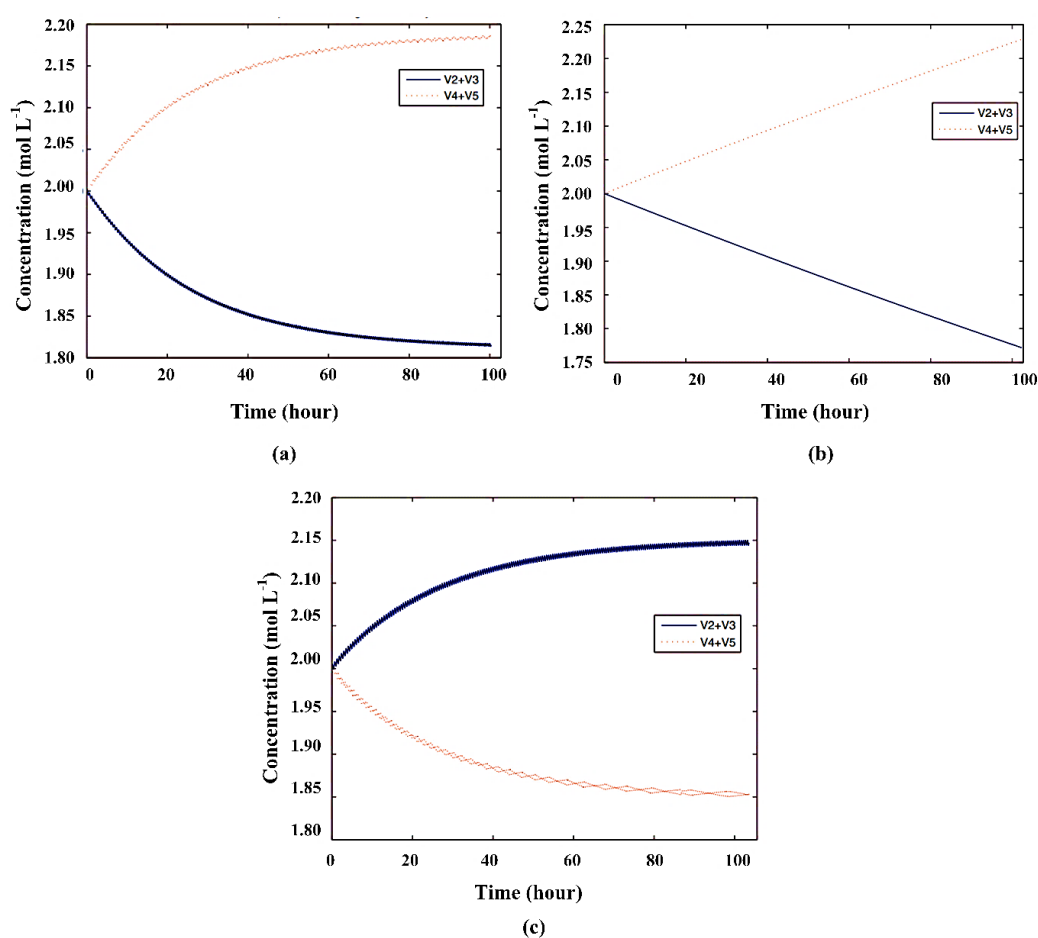


Figure 3.6 Concentration of positive and negative electrolytes during 200 cycles for (a) CMV membrane, (b) AMV membrane, and (c) Nafion 115 membrane (Tang *et al.*, 2011).

The self-discharge reactions was investigated by Sun *et al.* (2015). To study the step that the self-discharge reactions take place by the diffusion of vanadium ions across the Nafion 115 membrane, the diffusion coefficient of each vanadium ion was initially measured. The result showed that the coefficients were found in the order of $V^{2+} > VO^{2+} > VO_2^+ > V^{3+}$; this order is consistent with the report by Tang *et al.* (2011). Furthermore, the variation in the open circuit voltage cell could be used for classifying the self-discharge process into five regions: three regions with a gradual decrease of open circuit voltage (OCV) and two regions with sharply decreasing OCV (Figure 3.7). At the early stage of the self-discharge process (region 1), the self-discharge reaction in the negative half-cell occurs as shown in Eqs. (3.4) – (3.6), leading to a decrease in V^{2+} and an increase in V^{3+} . For the positive half-cell, the increase of VO^{2+} is faster than that of V^{3+} in the negative half-cell because the higher rate of V^{2+} diffusion across the membrane increases the self-discharge reactions [Eqs. (3.7) and (3.9)], which also significantly decrease the VO_2^+ concentration in the positive half-cell. As a result, the VO_2^+ concentration decreased and there is only VO^{2+} in the positive half-cell, while both V^{2+} and V^{3+} still exist in the negative half-cell. Thus, the self-discharge reactions in region 2 can be represented by Eqs. (3.5) and (3.9). In region 3, the self-discharge reactions [Eqs. (3.5) and (3.9)] continually occur in negative and positive half-cells. As a result, the accumulation of V^{3+} ions are observed in both half-cells. Finally, V^{2+} ions in the negative half-cell are exhausted and the self-discharge process switches to regions 4 and 5. At beginning of region 5, V^{3+} and VO^{2+} ions coexist in the positive electrolyte, while only V^{3+} ions are present in the negative half-cell. The amount of V^{3+} ions in the negative electrolyte is higher than that in the positive electrolyte. On the other hand, the VO^{2+} ion concentration is higher in the positive half-cell than in the negative half-cell. Hence, in this region, only diffusion of V^{3+} and VO^{2+} ions occur until the concentration becomes equal in both half-cells. However, in the normal operation of VRFB, the complete self-discharge reaction takes place only in cells that are not operational for a considerable period (standby mode); thus, the self-discharge reactions occur only in region 1. Moreover, the electrolyte imbalance from self-discharge reactions is directly affected by the residence time of the electrolyte because these reactions take place in the cell itself.

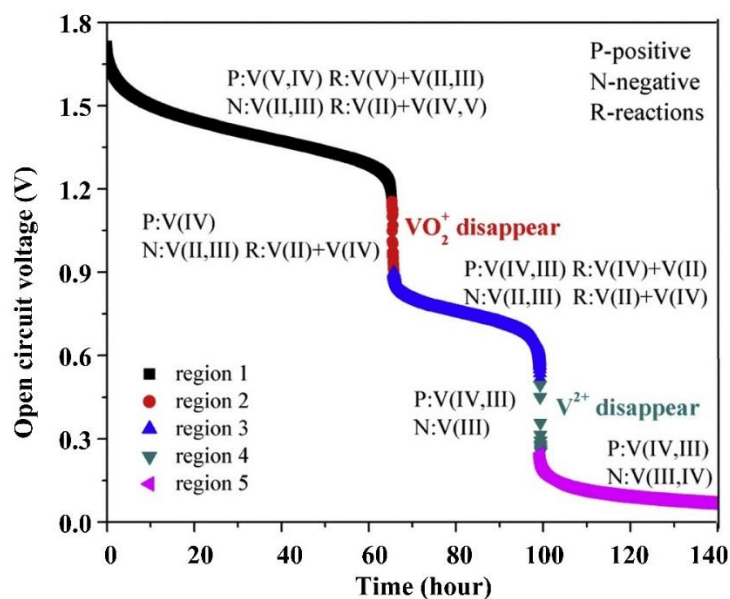


Figure 3.7 Open circuit voltage curve during the self-discharge process (Sun *et al.*, 2015).

3.1.4 Volumetric transfer

A volumetric transfer is the process of water transfer across a membrane and includes the transportation of ions under a concentration gradient across the membrane, water carried by charge-balancing species, and water transport by the pressure difference between the positive and negative half-cells (Sukkar and Skyllas-Kazacos, 2003). Water transfer is an important problem in the VRFB and needs to be eliminated as it causes variation in the vanadium concentration in both half-cells, because of which the concentrated vanadium ions can precipitate to vanadium salts. For preventing precipitation, the operating temperature window of VRFB must be decreased. In addition, the high-water transfer can lead to the electrolyte flooding in the reservoir, causing an operational problem in commercial VRFBs. The volumetric transfer direction was investigated by Mohammadi *et al.* (1997). They used CMV and Nation 117 membranes as the cation exchange membranes and AMV and DMV membranes as the anion exchange membranes. It was observed that the direction of volumetric transfer depends on membrane type. For the cation exchange membrane, the net volumetric transfer is toward the positive half-cell, which is opposite to the direction of hydrostatic pressure; for the anion exchange membrane, the net volumetric transfer is toward the

negative half-cell, which is the same as the direction of hydrostatic pressure reported by Mohammadi and Skyllas-Kazacos (1995). The extended dynamic model was proposed by Badrinarayanan *et al.* (2014) for studying the effect of bulk electrolyte transfer; a cation exchange membrane is used in this simulation. Thus, volume of electrolyte transfer from negative to positive half-cell (Figure 3.8).

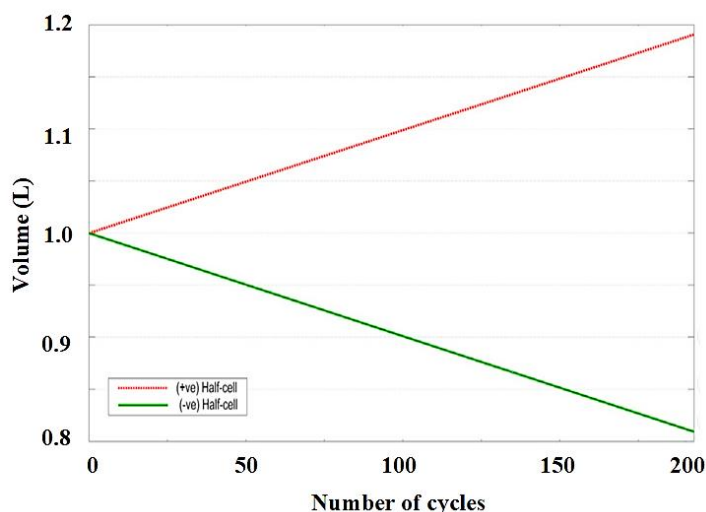


Figure 3.8 Change of electrolyte volume due to bulk water transfer across the membrane during 200 cycles of the charge-discharge process (Badrinarayanan *et al.*, 2014).

3.2 Performance prediction by mathematical model of VRFB

Modelling and simulations of VRFB are utilized to develop and prediction the performance of battery and they are a cost-effective method for reducing the number of cases in experimental test. To study and improve on performance of VRFB, many research groups have developed the modelling of VRFB for prediction the effects of operating parameters such as the initial vanadium and acid concentration, applied current density, electrolyte flow rate on the battery performance (Ma *et al.*, 2012; Yang *et al.*, 2015). The mathematical model plays a significant role to effective performance predict and solve optimization problem to achieve the maximum system efficiency. Thus, it is important to study the various models and their assumptions for implement in this research. The details of modelling are shown as follow.

3.2.1 Application of the VRFB multi-dimensional model or zero-dimensional model

The multi-dimensional models are very useful in design application which can study in distribution of concentration, electrolyte velocity as well as the potential in the cell. Shah *et al.* (2008) developed the two-dimension transient model of VRFB and reported that the electrolyte flow rate was an important operating parameter. At higher electrolyte flow rate, there were uniformity in the vanadium concentration, more distributed of current density and overpotential. You *et al.* (2009) proposed a simple model of VRFB based on the developed model by Shah *et al.* (2008). The results revealed that decreasing of electrode porosity could also increase the reduction rate of reactant concentration affecting to higher average transfer current density and uniform distribution of overpotential. Al-Fetlawi *et al.* (2009) reported that increasing electrolyte flow rate, not only improved the coulombic efficiency but could also use for keeping the uniform temperature distribution leading to avoidance the hot spot in stack. In additional, heat loss to environment had a significant effect on the charge-discharge cell voltage and temperature distribution therefore, heat management strategy was required to maintain the desired of operating stack temperature. Ma *et al.* (2011) analyzed the negative half-cell performance of VRFB by using an isothermal three-dimensional model based on the comprehensive conservation laws which were momentum, mass and charge transfer couple with kinetic model of vanadium species. At the inlet-outlet area, it was found that there was a higher value of transfer current density where the high velocity occurred and the flow pattern along with the inlet-outlet electrode had a similar symmetric pattern. The side reaction and corrosion of electrode material took place at a higher value of overpotential caused by the lower of electrolyte flow rate. Thus, the key point for optimal design of VRFB should create the uniform of electrolyte velocity distribution in electrode.

However, their complexity of multi-dimensional models was consumed the computation power and times for simulating in large scale and long-term monitoring. To study the capacity fade and enables extend cycling of the VRFB, a zero-dimensional or lumped system model was developed by reducing dimensionality while capturing the key physics necessary depended on the assumption of researcher. The cycling performance of VRFB including the effects of vanadium ions diffusion was

investigated by Maria Skyllas-Kazacos and Goh (2012). The results of this simulation showed that the number of cycles that battery capacity reaches steady stage depends on operating current and magnitude of permeability coefficient through membrane. The capacity loss of VRFB was due to the build-up or decay of vanadium ions concentration in each half-cell and periodic remixing was required for regeneration the capacity loss caused by differential ions and solution transfer. In case of gassing side reaction and air oxidation, if only 0.1% of charging current went to hydrogen evolution during charging cycle would lead to 10% vanadium ions imbalance and capacity loss after 100 cycles. For large scale of the VRFB, the charging and discharging time in one cycle could be used several hours. In addition, there are many cells in the stack and their interaction between each cell affected to the temperature gradient thus, the zero-dimensional model is appropriate for this application. Yan *et al.* (2016) extended the dynamic model of VRFB for investigation and prediction the temperature profile of each cells in a stack. The pilot-scale of the VRFB which is a 2.5 kW/15 kWh VFB system comprising 19 cells stack was employed in this simulation. The study considered the two different scenarios, during standby periods when the pumps were tuned off and during a resident power arbitrage periods when a battery was charged during off-peak periods and connected to the load during the peak times and the two types of membrane, Naffion 155 and AMV, was considered. The simulation results showed that in standby periods, the heat generated in stack with Naffion was dominated by heat generation from self-discharge reactions but in stack with AMV heat generated was dominated by the surrounding temperature variation according to the different magnitude of vanadium ions permeability through membrane which the Naffion was higher than AMV leading to larger rate of self-discharge reaction. During a resident power arbitrage, the self-discharge reaction was completed in stack in the system with Naffion membrane while it did not occur in system with AMV and the temperature in stack with Naffion could build up to 60 °C in the one cycle of charge and discharge over a period of 7 days whereas the temperature in stack with AMV built up to only 30 °C. Additionally, the temperature profiles in stack were oscillating with high frequency and very small amplitudes caused by the interactions between adjacent cells. The heat generation was rapid and accumulated at the beginning of standby periods leading to temperature increasing quickly therefore the oscillations do not take place but at the at the end of

standby periods the temperature different between the edges and the center of stack is smaller from depletion of some self-discharge reaction thus the heat transfer between adjacent cells were not dominated by the heat form center to edges only but rather from higher to lower temperature cells.

Thus, the zero-dimensional or lumped system models are very useful for long-term monitoring, large-scale of the VRFB, studying of interaction in the system, as well as the optimal control strategy.

3.2.2 Electrolyte imbalance model

The capacity loss from electrolyte imbalance has become more essential as mention above. To predict the aging of the system, it is important to include the phenomena leading to capacity loss which are the gassing side reaction, ions diffusion through the membrane and volumetric transfer into the VRFB models. The effects of hydrogen were studied from a developed model by including dynamic conservation equations of charge mass and momentum (Shah *et al.*, 2010). Characteristic of gas evolving was the formation of gas bubble effecting in reduction in volume of liquid electrolyte, active surface area for reaction and momentum transfer. Furthermore, the bubbles hindered the flow of electrolyte and reduced mass and charge transfer coefficient resulting in reduction the efficiency of the battery. In additional, increasing of applied current density to the cell also increased the gas volume fraction in the negative electrode at the same of SOC and the results suggested that a high flow rate of electrolyte through the cell could be used to reduce this increase in gas volume (Shah *et al.*, 2010). The effects of oxygen evolution were also studied by extend the framework of an exist model to include a thermal energy balance. The results showed that formation of oxygen bubble impacts the performance by reducing the active surface area of reaction in positive electrode, reducing the effective diffusion coefficient because the increasing of gas volume fraction. For reducing the volume of oxygen gas, increasing the mean linear electrolyte flow rate was recommend because it also increased the rate of gas removed from the cell. The operating temperature also affected to the rate of oxygen evolution due to when the operating temperature increase, the rate of oxygen evolution increased and effected to more consume the applied current. Thus, the rate of oxidation in the positive electrode decreased at any fixed time resulting in

the lower level SOC. In other hand, the time required to reach an equivalent SOC increased with temperature (Al-Fetlawi *et al.*, 2010).

The studied on the effects of ion diffusion and side reactions on the capacity loss was proposed by Tang *et al.* (2011). The dynamic model described the concentration change of vanadium ions in stack during charge-discharge process and could predict their effect on battery capacity. Three different types of membrane, Selemion CMV, Selemion AMV, Nafion 115, were employed in this simulation. The results showed that the higher diffusion coefficient for vanadium ions across the membrane increased the higher rate of capacity decay and there was total vanadium concentration built-up on positive half-cell with the corresponding loosed in the negative half-cell. However, this model did not consider the effect of electrolyte flow rate on the variation of vanadium concentration in cell.

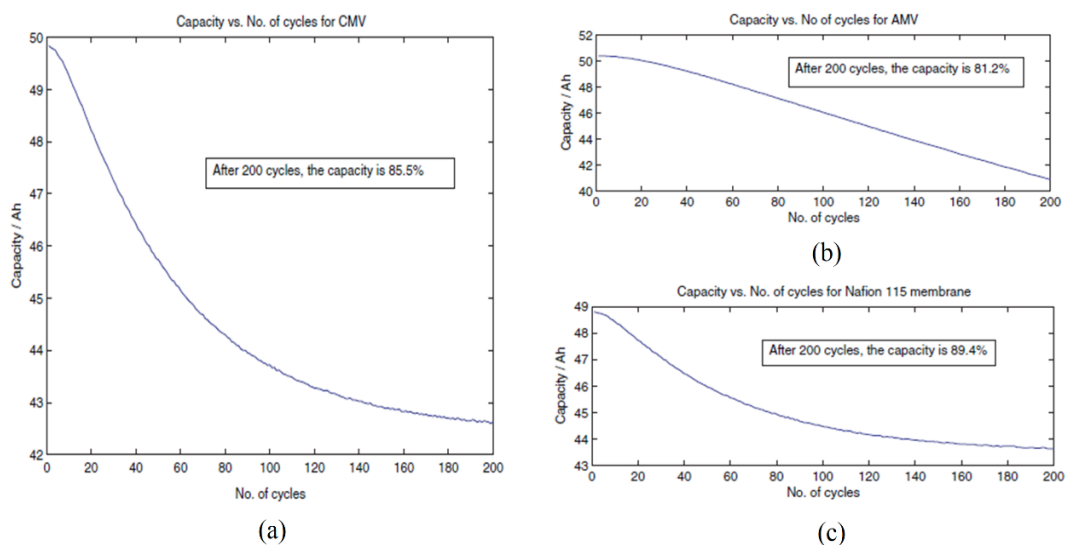


Figure 3.9 Comparison of capacity loss in three different types of membrane (a) CMV (b) AMV (c) Nafion 115 (Tang *et al.*, 2011).

Badrinarayanan *et al.* (2014) developed the extended dynamic model of stack including the effect of electrolyte volume change and temperature variation. The dynamic change of electrolyte volume explained by Schlogl's equation describing the bulk electrolyte transfer due to 3 reasons which are osmosis pressure across membrane, the vanadium ions-fluid interaction and the water transfer due to proton movement

across the membrane for charge balancing. The simulation could predict the capacity loss due to the cross-contamination and volumetric transfer over a long-term operation and electrolyte temperature variation. The result indicated that increasing the temperature affected to acceleration in capacity loss of battery, and the decay behavior also depended on the type of membrane. Naffion membrane was used for investigating the effect of bulk electrolyte transfer and temperature increase on battery capacity loss. It was noticed that there was a 19% change of electrolyte volume affecting to the change in vanadium concentration trend through 200 cycles from the initial concentration leading to the capacity loss, however there was no more capacity change when compared with the simulation excepting the effect of bulk electrolyte transfer at the end of 200 cycles as shown in Figure 3.10.

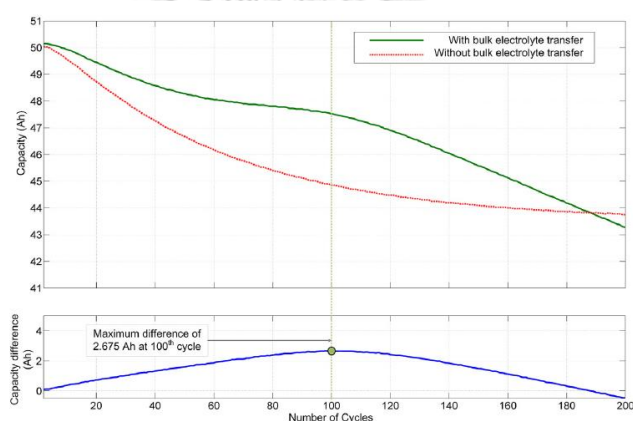


Figure 3.10 Comparison of capacity change with and without bulk electrolyte transfer phenomenon across 200 cycles (Badrinarayanan et al., 2014).

3.2.3 Pump power loss model

In practical application, the pump power loss is a significant factor in operating of the VRFB because it reduce the system efficiency. Xiong *et al.* (2013) applied the pump power loss model with the thermal model for investigation the VRFB response under different operating conditions. A kilowatt class VRFB stack was analyzed and simulated for battery modelling and the pump power loss was calculated based on the empirical equation. Moreover, the pump power loss depended on hydraulic design of the stack and connecting part between stack and tanks configuration. Tang *et al.* (2014)

presented the link of concentration overpotential and pressure losses to the electrolyte flow. The system of this simulation was a 5-kW/15-kWh stack comprising 40 individual cells and the general pressure loss was considered with head losses in pipes, flow frame and porous electrode, the latter two are dominant in the total losses affecting to the battery performance. Merei *et al.* (2015) proposed the multi-physic model of VRFB including the mechanical loss. In order to prove the consistency with the experimental results, the simulation was carried out over a period of 90 hour with the battery capacity of 75 kWh. Over a period of simulation, the pump power losses were between 2% and 6% of the VRFB power and the higher losses occurring when the battery was charge at the high SOC or discharge a low SOC.

3.3 Operating condition of the VRFB

The electrolyte flow rate was taken into consideration as the manipulated variable in the VRFB system. Under a fast-constant flow rate providing the good heat transfer and mass transfer capability. The good heat transfer could reduce the differential temperature between stack and electrolyte tanks leading to impossible disregarding influence on stack temperature during the standby period (Tang *et al.*, 2012). The good mass transfer of active species could increase the local mass transfer coefficient leading to reducing in concentration overpotential. However, operating at high constant flow rate consumed high pump power loss. Thus, the maximum battery efficiency could achieve at the optimal flow rate which could provide the minimize charging energy and maximize discharging energy as shown in Figure 3.11.

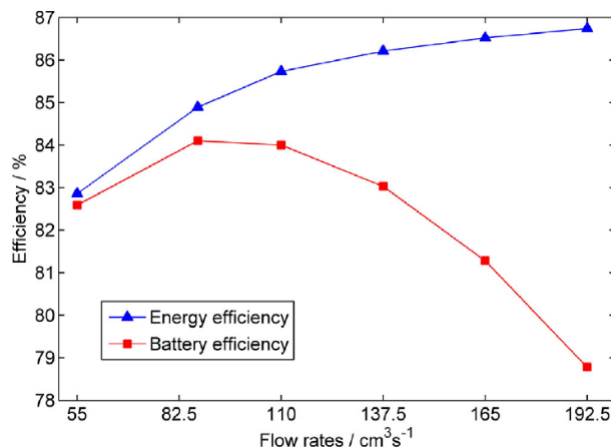


Figure 3.11 Energy and battery efficiencies under various flow rates (Xiong *et al.*, 2013).

The variation flow rate calculation was based on the Faraday's law of electrolysis and the effect of electrolyte flow rate was studied by varying a flow factor that used to manipulate the magnitude of flow rate (Tang *et al.*, 2014). From simulation results, the trend of voltage, coulombic and energy efficiency increased with increasing flow factor under both constant and variable flow rate conditions. During charging-discharging, the higher flow factor could reduce the concentration overpotential leading to avoiding the premature cut-off voltage and extending a time at the end of charge-discharge. However, the trade-off between high flow rate and pump losses had to be figured out the optimal flow rate for achieving the highest system efficiency. Wang *et al.* (2017) presented the control strategy of the electrolyte flow rate, the dynamic optimization was solved to find the flow factor of both half-cells for minimizing the total power losses during the charge-discharge process. The result shows that this control strategy can ensure a high system efficiency more than 87%.

CHAPTER IV

MODELING OF VANADIUM REDOX FLOW BATTERY

4.1 Mathematical model of vanadium redox flow battery

4.1.1 Model assumptions

In this study, the mathematical models will be developed based on necessary assumptions simplification of the system and the simulations will be carried out in MATLAB software.

Electrode assumptions

1. Electrode physical properties, electrode surface area, pore diameter and thickness of electrode are constant.
2. The anodic and cathodic transfer coefficient are equal 0.5 by the symmetry of electron transfer.

Electrolyte assumptions

3. Equilibrium of side reactions in solution are instantaneously reached.
4. Electrochemical reaction follows Butler-Volmer equation.
5. The electrolyte is perfectly mixed which the temperature and concentration in each position of cell are uniform and the convection term is dominated in the flow direction.
6. Heat due to electrolyte mixing is very small so that it can be neglected.
7. The electrolyte properties, density, viscosity and heat capacity are constant.
8. The electrolyte volume in each half-cell and tank are constant.
9. Effect of gas bubble from oxygen and hydrogen evolution is neglected.

Membrane assumptions

10. Vanadium ions diffusion through the membrane are only depended on the temperature according to Arrhenius equation.

11. Migration and electro-osmosis rate coefficient are constant.

12. The membrane conductivity is only dependent on the temperature.

4.1.2 Electrochemical models

The open circuit voltage (E_{OCV}) known as the voltage of the electrochemical cell without the current flow could be described by the Nernst equation according to Eq. (4.1) which is the potential difference between positive (E_p) and negative (E_n) electrodes as shown in Eqs. (4.2) and (4.3), respectively. The standard potentials (E_p^0 and E_n^0) are defined at the standard state which the concentration of active species ($C_{(i)}$) is 1 mol dm^{-3} , thus the variation from the standard state could be corrected by the exponential term in the Nernst equation.

$$E^{OCV} = E_p - E_n = E^0 + \frac{RT}{nF} \ln \left(\frac{C_{V^{2+}} C_{VO_2^+} C_{H^+}^2}{C_{V^{3+}} C_{VO^{2+}}} \right) \quad E^0 = 1.259 \text{ V} \quad (4.1)$$

$$E_p = E_p^0 - \frac{RT}{nF} \ln \left(\frac{C_{VO^{2+}}}{C_{VO_2^+} C_{H^+}^2} \right) \quad E_p^0 = 1.004 \text{ V} \quad (4.2)$$

$$E_n = E_n^0 - \frac{RT}{nF} \ln \left(\frac{C_{V^{2+}}}{C_{V^{3+}}} \right) \quad E_n^0 = -0.255 \text{ V} \quad (4.3)$$

The ohmic loss (η_{ohm}) in VRFB system consists of electrode, membrane and electrolyte is performed by the three terms in Eqs. (4.4), respectively. The correlation of the membrane conductivity (σ_{mem}) with the temperature is proposed by (Yang *et al.*, 2015) that can be calculated by Eq. (4.5). The loss from electrolyte expressed as the function of the electrolyte conductivity (σ_{elec}) is estimated by Eq. (4.6). Thus, the

diffusion coefficient of each species is modified to the effective diffusion coefficient as shown in Eq. (4.7).

$$\eta_{\text{ohm}} = i \left(\frac{d_e}{\sigma_e} + \frac{d_{\text{mem}}}{\sigma_{\text{mem}}} + \frac{d_{\text{elec}}}{\sigma_{\text{elec}}} \right) \quad (4.4)$$

$$\sigma_{\text{mem}} = 7.3 \exp \left[1268 \left(\frac{1}{T_{\text{ref}}} - \frac{1}{T} \right) \right] \quad (4.5)$$

$$\sigma_{\text{elec}} = \frac{F^2}{RT} \sum_i z_i^2 D_i^{\text{eff}} c_i \quad (4.6)$$

$$D_i^{\text{eff}} = \varepsilon^{3/2} D_i \quad (4.7)$$

The correlation of the current density (i) on the activation overpotential (η_{act}) and composition adjacent to the electrode surface could be represented by the Butler-Volmer equation as mentioned in section 2.1.2.1 (Newman and Thomas-Alyea, 2012). In addition, the exchange density of anodic and cathodic reactions [Eqs. (4.8) and (4.9)] also depends on the composition of the solution adjacent to the electrode surface. Not only the composition of electrolyte, but the temperature of electrolyte also effects to the exchange current density variable in the term of rate constant (k_j) shown by Eq. (4.10)

$$i_{0,\text{p}} = Fk_{\text{p}} C_{\text{VO}^{2+}}^{(1-\alpha_c)} C_{\text{VO}_2^+}^{(\alpha_c)} \quad (4.8)$$

$$i_{0,\text{n}} = Fk_{\text{n}} C_{\text{V}^{2+}}^{(1-\alpha_a)} C_{\text{V}^{3+}}^{(\alpha_a)} \quad (4.9)$$

$$k_j = k_{0,\text{ref},j} \exp \left(\frac{zFE_j^0(T_{\text{ref}})}{R} \left[\frac{1}{T_{\text{ref}}} - \frac{1}{T} \right] \right) \quad (4.10)$$

According to the detail in electrode assumption, the anodic (α_a) and cathodic (α_c) transfer coefficient are equal 0.5 by the symmetry of electron transfer. The activation loss of each half-cell in VRFB can be determined by Eq. (4.11) for positive half-cell and Eq. (4.12) for negative half-cell.

$$\eta_{\text{act,p}} = \frac{2RT}{nF} \left[\sinh^{-1} \left(\frac{i}{2i_{0,p}} \right) \right] \quad \text{where} \quad i_{0,p} = Fk_p \sqrt{C_{\text{VO}^{2+}} C_{\text{VO}_2^+}} \quad (4.11)$$

$$\eta_{\text{act,n}} = \frac{2RT}{nF} \left[\sinh^{-1} \left(\frac{i}{2i_{0,n}} \right) \right] \quad \text{where} \quad i_{0,n} = Fk_n \sqrt{C_{\text{V}^{2+}} C_{\text{V}^{3+}}} \quad (4.12)$$

The surface concentration (C_{surface}) of the active species is influenced by the electrolyte flow rate and concentration at bulk electrolyte (C_{bulk}). Thus, the regulation of electrolyte flow rate can control the magnitude of the concentration at surface of electrode. The concentration loss (η_{conc}) can be determined by using Eq. (4.13) for positive half-cell and Eq. (4.14) for negative half-cell which include the local mass transfer coefficient (k_m) of the active species in carbon fiber electrode proposed by Tang *et al.* (2014). The calculation of local mass transfer coefficient reported by Khazaeli *et al.* (2015). This value depends on the effective diffusion coefficient of reactant (D_i^{eff}), pore diameter of electrode (d_f) and Reynolds number (Re) as Eq. (4.15).

$$\eta_{\text{conc,p}} = -\frac{RT}{F} \ln \left(1 - \frac{i}{k_{m,p} n F C_{\text{bulk,p}}} \right) \quad (4.13)$$

where $C_{\text{bulk,p}} = C_{\text{VO}^{2+}}$ for charging, while $C_{\text{bulk,p}} = C_{\text{VO}_2^+}$ for discharging

$$\eta_{\text{conc,n}} = -\frac{RT}{F} \ln \left(1 - \frac{i}{k_{m,n} n F C_{\text{bulk,n}}} \right) \quad (4.14)$$

where $C_{\text{bulk,n}} = C_{\text{V}^{3+}}$ for charging while $C_{\text{bulk,n}} = C_{\text{V}^{2+}}$ for discharging

$$k_{m,i} = \frac{D_i^{\text{eff}}}{d_f} 7Re^{0.4} \quad (4.15)$$

The current density loss associated with the OER and HER, which predominantly occur during the charging process at the positive and negative electrodes, respectively, are approximated by the Tafel relationship according to Eq.

(4.16) (Al-Fetlawi *et al.*, 2010; Shah *et al.*, 2010). The correlation between the exchange current density and temperature is described by Eq. (4.17), while the overpotentials for the gassing side reactions (η_g) are calculated from Eq. (4.18), which is the difference between the half-cell electrode potential and the standard potential of the gassing side reaction (Al-Fetlawi *et al.*, 2010).

$$i_g = i_{0,g} \exp\left(\frac{F(1-\beta_g)\eta_g}{RT}\right) \quad (4.16)$$

$$i_{0,g} = i_{\text{ref},g} \exp\left(\frac{nFE_g^0(T_{\text{ref}})}{R} \left[\frac{1}{T_{\text{ref}}} - \frac{1}{T}\right]\right) \quad (4.17)$$

$$\eta_{g,j} = \eta_j + E_j^0 - E_{g,j}^0 \quad (4.18)$$

4.1.3 Conservation equation

For VRFB modelling, the mass balance in the electrode and electrolyte tank is based on the molar concentration (c_i) in the liquid electrolyte solution and assumes that the electrolyte volume is constant:

$$V^e \frac{dC_k^e}{dt} = Q^e (C_k^t - C_k^e) + \frac{I_{\text{redox}}}{nF} + \sum (s_i N_{\text{mem}}) \quad (4.19)$$

$$V^t \frac{dC_k^t}{dt} = Q^t (C_k^e - C_k^t) \quad (4.20)$$

where V is the volume of the electrolyte, Q is the electrolyte flow rate, and the superscripts e and t represent the electrode and electrolyte tank, respectively. Notably, the current for the redox reaction (I_{redox}) in Eq. (4.21) is the applied current (I_{applied}) that is consumed by the gassing side reaction and can be determined by using the following equation (Merei *et al.*, 2015).

$$I_{\text{redox}} = I_{\text{applied}} - i_g A_s V^e \quad (4.21)$$

The molar flux across the membrane (N_{mem}) is the summation of the species movement by diffusion, hydraulic pressure migration, and electro-osmosis as reported by Schafner *et al.* (2018). For migration and electro-osmosis, the direction of mass transfer depends on the potential across the membrane ($\Delta\phi$), which is a function of the current density and ohmic overpotential. During the charging process, the species in the positive half-cell move to the negative half-cell, while the reverse is observed during the discharging process. Moreover, the flux of the hydraulic pressure depends on the pressure difference between the half-cells (Δp), which is a function of the electrolyte viscosity, flow rate, and cell structure. The species in the half-cell will move from the half-cell with the higher pressure to that with the lower pressure. The summary of the total flux movement across the membrane is presented in Table 4.1. The rate of the self-discharge reaction depends on the total molar flux movement across the membrane and the stoichiometric coefficient ratio (s_i) of the self-discharge reaction as summarized in Table 4.2.

Table 4.1 Summary of the total flux movement across the electrode membrane.

Diffusion (N_i^{Diff})	$k_i^{\text{Diff}} C_i A_{\text{mem}} / d_{\text{mem}}$	(4.22)
-----------------------------------	---	--------

Migration (N_i^{Mig})	$k_i^{\text{Mig}} C_i \Delta\phi A_{\text{mem}}$	(4.23)
----------------------------------	--	--------

Electro-osmosis (N_i^{Eosm})	$k_i^{\text{Eosm}} C_i \Delta\phi A_{\text{mem}}$	(4.24)
---	---	--------

Hydraulic pressure (N_i^{Hydr})	$k_i^{\text{Hydr}} C_i \Delta p A_{\text{mem}}$	(4.25)
--	---	--------

Table 4.2 Concentration variation due to molar flux movement across the electrode membrane during the self-discharge reactions.

Self-discharge reaction	(C_k)	$(\sum s_i N_{mem})$
At the negative half-cell		
$VO_2^+ + 2V^{2+} + 4H^+ \leftrightarrow 3V^{3+} + H_2O$	$C_{V^{2+}}$	$-N_{V^{2+}}^{mem} - 2N_{VO_2^+}^{mem} - N_{VO^{2+}}^{mem}$
$VO^{2+} + V^{2+} + 2H^+ \leftrightarrow 2V^{3+} + H_2O$	$C_{V^{3+}}$	$N_{V^{3+}}^{mem} + 3N_{VO_2^+}^{mem} + 2N_{VO^{2+}}^{mem}$
	C_{H^+}	$N_{H^+}^{mem} - 4N_{VO_2^+}^{mem} - 2N_{VO^{2+}}^{mem}$
At the positive half-cell		
$V^{2+} + VO_2^+ + 2H^+ \leftrightarrow 3VO^{2+} + H_2O$	$C_{V^{4+}}$	$-N_{VO^{2+}}^{mem} + 2N_{V^{3+}}^{mem} + 3N_{V^{2+}}^{mem}$
$V^{3+} + VO_2^+ \leftrightarrow 2VO^{2+}$	$C_{V^{5+}}$	$-N_{VO_2^+}^{mem} - 2N_{V^{2+}}^{mem} - N_{V^{3+}}^{mem}$
	C_{H^+}	$-N_{H^+}^{mem} - 2N_{V^{2+}}^{mem}$

4.1.4 Pump power model

To determine the battery system efficiency, the pump power of VRFB is calculated based on the developed model by Xiong *et al.* (2013) and Wang *et al.* (2017). The energy consumption of pump is related to the stack and hydraulic circuits design and the electrolyte flow rate. The total pressure drop is caused by the piping system and the cell stack and the pump power consumption can be expressed as:

$$P_{pump}(t) = \Delta p_{pipe} Q(t) + \frac{\mu h_e}{\lambda A_{flow}} Q^2(t) \quad (4.26)$$

$$\lambda = \frac{d_f^2 \varepsilon^3}{\lambda_{CK} (1 - \varepsilon)^2} \quad (4.27)$$

where μ is the electrolyte viscosity, h_e is the height of the electrode, ε is the electrode porosity, λ is the permeability of porous electrode, and λ_{CK} is the Carman-Kozeny constant.

To monitor the battery performance, the battery efficiencies, which are the coulombic, voltage, energy and system efficiencies, and discharge capacity, are defined as shown in Table 4.3.

Table 4.3 Definition of battery performance

Coulombic efficiency (CE)	$\frac{\int (i_{\text{discharge}}(t)) dt}{\int (i_{\text{charge}}(t)) dt}$	(4.28)
Voltage efficiency (VE)	$\frac{\int (V_{\text{discharge}}(t)) dt}{\int (V_{\text{charge}}(t)) dt}$	(4.29)
Energy efficiency (EE)	CE×VE	(4.30)
System efficiency (SE)	$\frac{\int (V_{\text{discharge}}(t)I_{\text{discharge}}(t) - P_{\text{pump}}(t)) dt}{\int (V_{\text{charge}}(t)I_{\text{charge}}(t) + P_{\text{pump}}(t)) dt}$	(4.31)
Discharge capacity (DC)	$\int (i_{\text{discharge}}(t)) dt$	(4.32)

4.2 Extended Kalman filter for vanadium redox flow batteries

To achieve the highest battery efficiency, a periodic electrolyte regeneration must be conducted when the battery capacity is decreased. Consequently, the measurement of an electrolyte imbalance is required for the energy management system. The imbalance level is related to the individual half-cell state of charge (SOC); hence many approaches for individual measurement, such as conductivity, UV-vis spectroscopic, transmission spectra, ultrasonic velocity, and oxidation state measurement, are applied to the VRFB. However, the correlation between the measured data and SOC significantly depend on the vanadium and acid concentration and electrolyte temperature. Thus, to precisely measure the SOC, the variation of electrolyte concentration and temperature must be known for using them as the input parameters

in the database correlation between the measurement data and the SOC. Although the open circuit voltage can not be implemented for real-time individual SOC monitoring, this method is simple and widely used for average SOC measurement. The extended Kalman filter approach is adapted for estimating the individual SOC via the vanadium concentration prediction by only measurement the modified OCV. Moreover, this filter can be used to minimize measurement noise effects in the estimation of SOC and SOH which are the battery system states (Nicolas Watrin, 2012).

4.2.1 Observability matrix for vanadium redox flow batteries models

The dynamic model for describing the vanadium and proton concentration are shown in Eqs. (4.19) and (4.20). The number of active species in the system is 6 variables, which are V^{2+} , V^{3+} , VO^{2+} , VO_2^+ , H^+ in positive half-cell and H^+ in negative half-cell. As a result, the total number of state variable in cell and electrolyte tank is 12 variables. However, the state variables can be reduced if the proton concentration in positive and negative half-cells are assumed to be a constant value, hence the standard potential (E^0) in Nernst equation changes to formal potential (\tilde{E}^0) as shown in Eq. (4.33).

$$E_{OCV} = \tilde{E}^0 + \frac{RT}{F} \ln \left(\frac{C_{V^{2+}} C_{VO_2^+}}{C_{V^{3+}} C_{VO^{2+}}} \right) \quad (4.33)$$

To monitoring the state of charge, the open circuit voltage is measured during charging-discharging process. Since the formal potential is the constant value, the measurement equation is formulated to Eq. (4.34). Hence, the observer matrix can be calculated as presented in Eq. (4.35) which has a dimension of 1x4.

$$h(x); E_{OCV} - \tilde{E}^0 = \frac{RT}{F} \left[\ln(C_{V^{2+}}) + \ln(C_{VO_2^+}) - \ln(C_{V^{3+}}) - \ln(C_{VO^{2+}}) \right] \quad (4.34)$$

$$C_k = \frac{\partial h}{\partial x} \Big|_{\hat{x}_{k|k-1}} = \begin{bmatrix} \frac{\partial h}{\partial x_1} & \frac{\partial h}{\partial x_2} & \frac{\partial h}{\partial x_3} & \frac{\partial h}{\partial x_4} \end{bmatrix} \\ = \begin{bmatrix} \frac{RT}{FC_{V^{2+}}} & \frac{RT}{FC_{V^{3+}}} & \frac{RT}{FC_{VO^{2+}}} & \frac{RT}{FC_{VO_2^+}} \end{bmatrix} \quad (4.35)$$

Although the number of measurement variable is not sufficient for estimating the states which is the vanadium concentration in cell and electrolyte reservoir, the monitoring of individual SOC is only required to know the vanadium concentration in reservoir. As a result, the dynamic model of vanadium redox flow batteries can be simplified as shown in Eqs. (4.36) -(4.39).

$$f_1(x); V_e \frac{dC_{V^{2+}}}{dt} = \frac{I}{F} + \frac{A_{\text{mem}}}{d_{\text{mem}}} \left(-k_2 C_{V^{2+}} - 2k_5 C_{VO_2^+} - k_4 C_{VO^{2+}} \right) \quad (4.36)$$

$$f_2(x); V_e \frac{dC_{V^{3+}}}{dt} = -\frac{I}{F} + \frac{A_{\text{mem}}}{d_{\text{mem}}} \left(-k_3 C_{V^{3+}} + 3k_5 C_{VO_2^+} + 2k_4 C_{VO^{2+}} \right) \quad (4.37)$$

$$f_3(x); V_e \frac{dC_{VO^{2+}}}{dt} = -\frac{I}{F} + \frac{A_{\text{mem}}}{d_{\text{mem}}} \left(-k_4 C_{VO^{2+}} + 3k_2 C_{V^{2+}} + 2k_3 C_{V^{3+}} \right) \quad (4.38)$$

$$f_4(x); V_e \frac{dC_{VO_2^+}}{dt} = \frac{I}{F} + \frac{A_{\text{mem}}}{d_{\text{mem}}} \left(-k_5 C_{VO_2^+} - 2k_2 C_{V^{2+}} - k_3 C_{V^{3+}} \right) \quad (4.39)$$

These functions can be changed into state space model as follow:

$$\begin{bmatrix} \dot{C}_{V^{2+}} \\ \dot{C}_{V^{3+}} \\ \dot{C}_{VO^{2+}} \\ \dot{C}_{VO_2^+} \end{bmatrix} = \begin{bmatrix} \frac{-k_2 A_{\text{mem}}}{d_{\text{mem}}} & 0 & \frac{-k_4 A_{\text{mem}}}{d_{\text{mem}}} & \frac{-2k_5 A_{\text{mem}}}{d_{\text{mem}}} \\ 0 & \frac{-k_3 A_{\text{mem}}}{d_{\text{mem}}} & \frac{2k_4 A_{\text{mem}}}{d_{\text{mem}}} & \frac{3k_5 A_{\text{mem}}}{d_{\text{mem}}} \\ \frac{3k_2 A_{\text{mem}}}{d_{\text{mem}}} & \frac{2k_3 A_{\text{mem}}}{d_{\text{mem}}} & \frac{-k_4 A_{\text{mem}}}{d_{\text{mem}}} & 0 \\ \frac{-2k_2 A_{\text{mem}}}{d_{\text{mem}}} & \frac{-k_3 A_{\text{mem}}}{d_{\text{mem}}} & 0 & \frac{-k_5 A_{\text{mem}}}{d_{\text{mem}}} \end{bmatrix} \begin{bmatrix} C_{V^{2+}} \\ C_{V^{3+}} \\ C_{VO^{2+}} \\ C_{VO_2^+} \end{bmatrix} + [1/F][I] \quad (4.40)$$

To confirm the observability of this system, the rank of observability matrix depending on the matrix C and A in Eqs. (4.35) and (4.40) must equal to 4 which is the number of the state. However, the rank of observability matrix is only 3, as a result the set of measurement equation and state space model is not sufficient in the vanadium concentration estimation.

To solve this problem, the individual measurement of open circuit voltage in each half-cell is applied. A conventional open circuit voltage is modified by additional the middle half-cell between the positive and negative cells as a reference electrolyte (Figure 4.1). The reference electrolyte is prepared by dissolving the vanadium pentoxide (V_2O_5) powder in sulfuric acid to generate the vanadium and acid solution of 1.5 M and 3.0 M, respectively. In addition, the electrolyte solution is adjusted the oxidation state of vanadium to +3.50. This fraction of vanadium oxidation state refers to the electrolyte composition and is call as “Vstate”. For example, a Vstate of +3.50 indicates the electrolyte consists of a V^{3+} ions while the fractional term refers the percentage of the higher oxidation state in the solution, hence 0.50 represent 50% of VO^{2+} and the remaining is the 50% of V^{3+} .

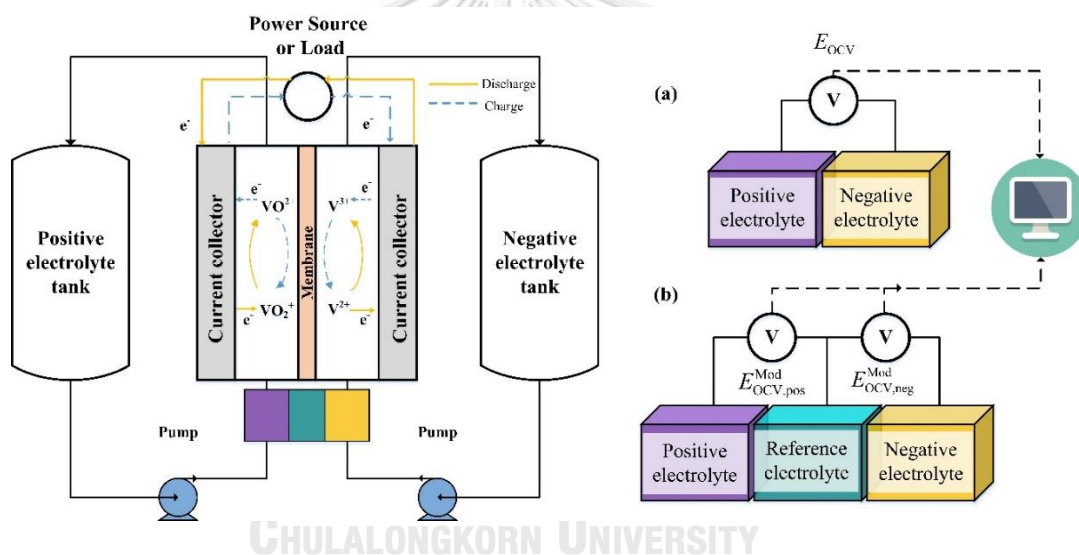


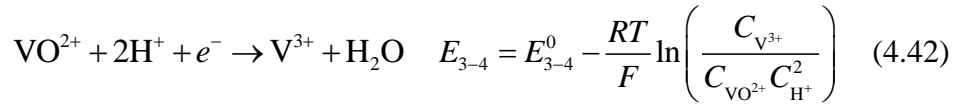
Figure 4.1 The schematic of the experiment to measure the open circuit voltage: (a) conventional OCV and (b) modified OCV (Ngamsai and Arpornwichanop, 2015a).

The Vstate of electrolyte solution is distinguished into 3 regions and their standard potentials are shown in Eqs. (4.41) - (4.43).

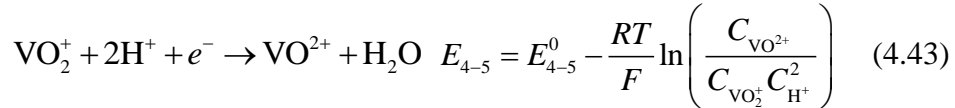
$Vstate + 2 \rightarrow +3$:

$$V^{3+} + e^{-} \leftrightarrow V^{2+} \quad E_{2-3} = E_{2-3}^0 - \frac{RT}{F} \ln \left(\frac{C_{V^{2+}}}{C_{V^{3+}}} \right) \quad (4.41)$$

Vstate +3 → +4:



Vstate +4 → +5:



In this measurement, the potential between positive (negative) electrolyte and the reference electrolyte are measured, the correlation of positive open circuit voltage ($E_{\text{OCV, pos}}^{\text{Mod}}$) and the negative open circuit voltage ($E_{\text{OCV, neg}}^{\text{Mod}}$) are presented in Eqs. (4.44) and (4.45), respectively.

$$E_{\text{OCV, pos}}^{\text{Mod}} = E_{4-5}^0 - E_{3-4}^0 - \frac{RT}{F} \ln \left(\frac{C_{\text{VO}^{2+}}}{C_{\text{VO}_2^+} C_{\text{H}^+}^2} \cdot \left(\frac{C_{\text{VO}^{2+}} C_{\text{H}^+}^2}{C_{\text{V}^{3+}}} \right)_{\text{ref}} \right) \quad (4.44)$$

$$E_{\text{OCV, neg}}^{\text{Mod}} = E_{3-4}^0 - E_{2-3}^0 - \frac{RT}{F} \ln \left(\left(\frac{C_{\text{V}^{3+}}}{C_{\text{VO}^{2+}} C_{\text{H}^+}^2} \right)_{\text{ref}} \cdot \frac{C_{\text{V}^{3+}}}{C_{\text{V}^{2+}}} \right) \quad (4.45)$$

However, the correlation between vanadium concentration and open circuit voltage can be reduced in the simple form as shown in Eqs. (4.46) and (4.47) according to the experimental data reported by Ngamsai and Arpornwichanop (2015a).

$$E_{\text{OCV, pos}}^{\text{Mod}} = E_{\text{pos}}^{0, \text{Mod}} - \frac{RT}{F} \ln \left(\frac{C_{\text{VO}^{2+}}}{C_{\text{VO}_2^+}} \right) \quad (4.46)$$

where $E_{\text{pos}}^{0, \text{Mod}} = E_{4-5}^0 - E_{3-4}^0 - \frac{RT}{F} \ln \left(\frac{1}{C_{\text{H}^+}^2} \cdot \left(\frac{C_{\text{VO}^{2+}} C_{\text{H}^+}^2}{C_{\text{V}^{3+}}} \right)_{\text{ref}} \right)$

$$E_{\text{OCV, neg}}^{\text{Mod}} = E_{\text{neg}}^{0, \text{Mod}} - \frac{RT}{F} \ln \left(\frac{C_{\text{V}^{3+}}}{C_{\text{V}^{2+}}} \right) \quad (4.47)$$

where $E_{\text{neg}}^{0, \text{Mod}} = E_{3-4}^0 - E_{2-3}^0 - \frac{RT}{F} \ln \left(\frac{C_{\text{V}^{3+}}}{C_{\text{VO}^{2+}} C_{\text{H}^+}^2} \right)_{\text{ref}}$

Since the modified positive ($E_{\text{pos}}^{0,\text{Mod}}$) and negative ($E_{\text{neg}}^{0,\text{Mod}}$) standard potential are reported to be the constant value, the measurement equation is formulated to Eqs. (4.48) and (4.49). Hence, the observer matrix can be calculated as presented in Eq. (4.50) which has a dimension of 2×4 . Since the rank of observability matrix formulating from the matrix A in Eq. (4.40) and matrix C in Eqs. (4.50) equal to 4, the system can be observed by this set of measurement equations.

$$h_1(x); \text{OCV}_{\text{pos}} - E_{\text{pos}}^{0,\text{Mod}} = \frac{RT}{F} \left[\ln(C_{\text{VO}_2^+}) - \ln(C_{\text{VO}^{2+}}) \right] \quad (4.48)$$

$$h_2(x); \text{OCV}_{\text{neg}} - E_{\text{neg}}^{0,\text{Mod}} = \frac{RT}{F} \left[\ln(C_{\text{V}^{2+}}) - \ln(C_{\text{V}^{3+}}) \right] \quad (4.49)$$

$$C_k = \frac{\partial h}{\partial x} \Big|_{\hat{x}_{k|k-1}} = \begin{bmatrix} \frac{\partial h_1}{\partial x_1} & \frac{\partial h_1}{\partial x_2} & \frac{\partial h_1}{\partial x_3} & \frac{\partial h_1}{\partial x_4} \\ \frac{\partial h_2}{\partial x_1} & \frac{\partial h_2}{\partial x_2} & \frac{\partial h_2}{\partial x_3} & \frac{\partial h_2}{\partial x_4} \end{bmatrix} = \begin{bmatrix} 0 & 0 & -\frac{RT}{FC_{\text{VO}^{2+}}} & \frac{RT}{FC_{\text{VO}_2^+}} \\ \frac{RT}{FC_{\text{V}^{2+}}} & -\frac{RT}{FC_{\text{V}^{3+}}} & 0 & 0 \end{bmatrix} \quad (4.50)$$

4.3 Simulation method

In this section, the algorithm for calculating the battery performance under electrolyte imbalance condition, the dynamic optimization and Kalman filter are presented. For analysis of battery performance in long-term operation, the vanadium redox flow battery was charged and discharge continuously until reach the desired number of cycles. The upper and lower limit voltage were defined for switching the operation mode. Figure 4.2 shows the algorithm for calculating the battery voltage of VRFB when the current density was defined in charging-discharging process. As mention in section 4.1, the electrochemical equations were used for monitoring the change of battery voltage from vanadium concentration variation. Moreover, the parameters in mathematical models relating to the system structure, cell components electrolyte properties and operating conditions.

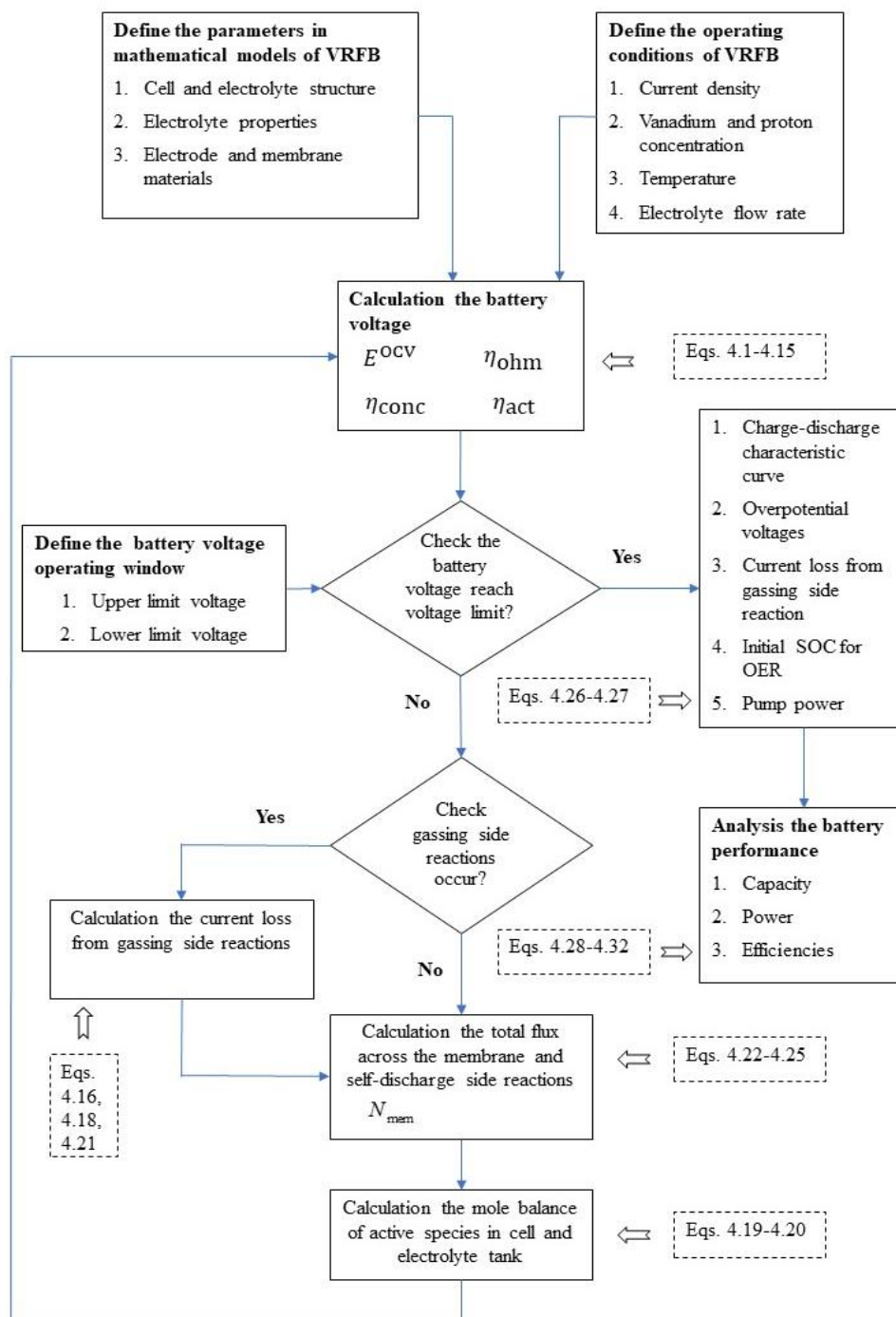


Figure 4.2 Algorithm for calculating battery voltage variation during charging-discharging process and performance analysis.

For dynamic optimization algorithm, the sequential discretization approach was applied to solve this problem. The battery operating time was defined from initial time (t_0) to final time (t_f) with the selected number of stages (n_s) for discretization the electrolyte flow rate profile. The initial guess of electrolyte flow rates was applied to solve the ordinary differential equation for vanadium concentration variation [Eq. 4.19] in each stage of system integration step. The final value of vanadium concentration in stage i was used as the initial condition for stage $i+1$. The vanadium concentration variation from t_0 to t_f , using the initial guess of electrolyte flow, was used for determining the objective function. The non-linear programming optimization was applied to find the new set of electrolyte flow rate profile, then the objective function was calculated and compared with the later value. The calculation process stops when the value of tolerance of electrolyte flow rate and objective function reach the desired value. The algorithm for calculating the optimal electrolyte flow rate maximizing the system efficiency is presented in Figure 4.3

Moreover, on-line optimization was applied to solve the optimal electrolyte flow rate consisting the variation of charge-discharge current density and this approach is necessary to know the current state of vanadium concentration before solving the optimization. As a result, Extended Kalman Filter (EKF) was applied to estimate the vanadium concentration. The initial of state error, process noise and measurement noise covariance matrix were defined as the input for EKF algorithm. The battery system models [Eqs. 4.19-4.20] were used as the reference data, while battery model according to Eq. 4.40 was used in prediction step of EKF algorithm. The vanadium concentration from the battery system model and prediction step were used for calculating the modified open circuit voltage [Eqs. 4.48-4.49] which refer to the measurement output from the system and output from the model, respectively. The error between the measurement value and model out was used for calculating the Kalman gain and updating the vanadium concentration in correction step. The algorithm for estimating the vanadium concentration is shown in Figure 4.4.

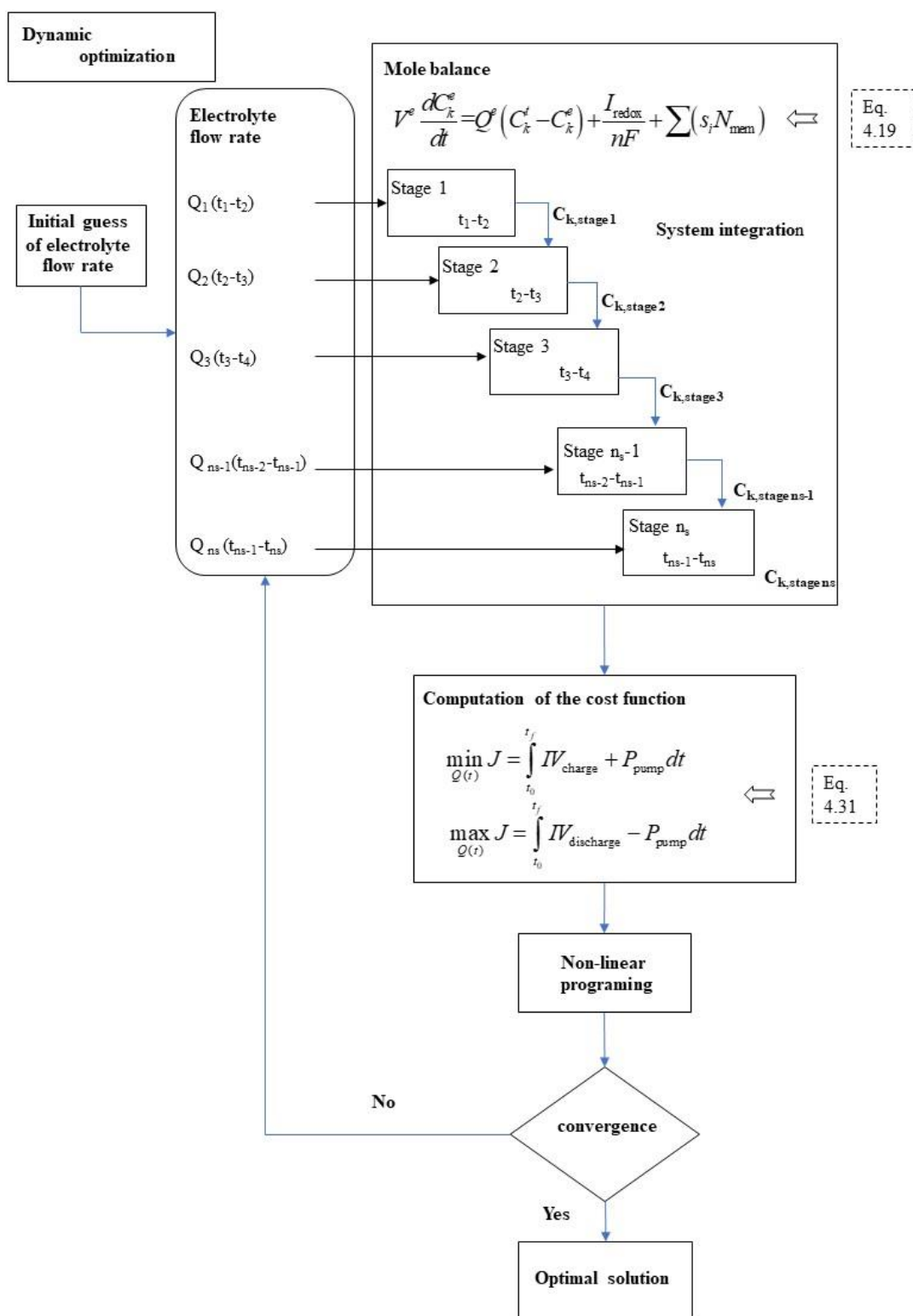


Figure 4.3 Algorithm for calculating the optimal electrolyte flow rate maximizing the system efficiency.

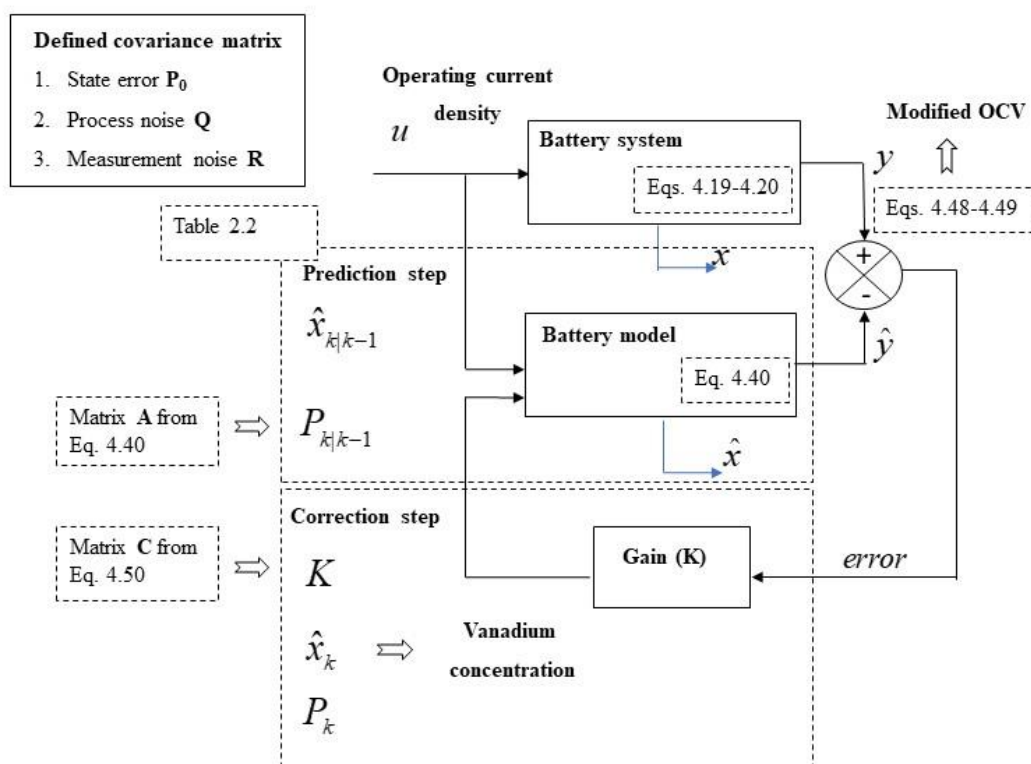


Figure 4.4 Algorithm for estimating the vanadium concentration by Extended Kalman Filter with the modified open circuit voltage measurement.

4.4 Model validation

The developed model was validated with the VRFB experimental data reported by Ngamsai and Arpornwichanop (2015c). A single cell with an effective area of 81 cm² and SIGRACELL carbon felts (GFD 4.6) was employed as the electrode. The electrode was activated by thermal treatment at 450 °C for 3 h. A 30- μ m thick APS-4 anion exchange membrane was employed. Next, 250 mL electrolyte was added to each side of the electrolyte tank. The experiment was operated by charging and discharging the battery at constant electric currents of 10 A and 20 A. Two peristaltic pumps were used to circulate the electrolyte solution through the cell at a constant flow rate per membrane surface of 0.026 mL s⁻¹ cm⁻². It was found that the open circuit voltage obtained from the experiment and simulation [Eq. (4.1)] is lightly different, which could be caused by the effect of Donan potential (Knehr and Kumbur, 2011) and the disregarding of activity coefficient (Pavelka *et al.*, 2015). In this study, the electrode

conductivity and the standard rate constant of the positive electrode are considered the tuning model parameters to explain the experimental actual cell voltage. The model parameters used for the VRFB simulation are given in Table 4.4. Figure 4.5a compares the experimental data with the simulation results, revealing that the computed results are in good agreement with the experimental data. The maximum relative error of the voltage during charging and discharging was 2.14%. Moreover, the model is validated with the experimental data reported by Ngamsai and Arpornwichanop (2015a) which presents the correlation between electrolyte imbalance level and discharge capacity. The simulation result shows a good consistency with experimental data over the low to medium range of imbalance level as shown in Figure 4.5b. This discrepancy result from in simulation, the ending point of charge-discharge process were defined by voltage limit, while the experiment is defined by the open circuit voltage. The SOC window for simulation is decreased due to the increase of overpotential at high level of electrolyte imbalance. As a result, the capacity from the simulation is lower than the experimental value.

Table 4.4 Model parameters used in the simulation of VRFB

Parameters	Symbols	Values	References
<i>VRFB geometry</i>			
- Height of the electrode	h_e	0.09 m	
- Width of the electrode	w_e	0.09 m	
- Thickness of the electrode	d_e	0.003 m	
- Thickness of the membrane	d_{mem}	30 μ m	
- Surface area of membrane	A_{mem}	8.1×10^{-3} m	
- Porosity	ε	0.94	
- Pore diameter of the electrode	d_f	1.0×10^{-5} m	
- Electrode conductivity	σ_e	363 S m ⁻¹	
- Tank volume	V^t	0.25 L	

Electrolyte properties

- Density	ρ	1300 kg m ⁻³	(Khazaeli <i>et al.</i> , 2015)
- Viscosity	μ	0.005 Pa s	(Khazaeli <i>et al.</i> , 2015)
- Diffusion coefficient of V ²⁺ /V ³⁺	$D_{V^{2+}} / D_{V^{3+}}$	2.4 x 10 ⁻¹⁰ m ² s ⁻¹	(Khazaeli <i>et al.</i> , 2015)
- Diffusion coefficient of VO ²⁺ /VO ₂ ⁺	$D_{VO^{2+}} / D_{VO_2^+}$	3.9x 10 ⁻¹⁰ m ² s ⁻¹	(Khazaeli <i>et al.</i> , 2015)
- Diffusion coefficient of H ⁺	D_{H^+}	9.312x 10 ⁻⁹ m ² s ⁻¹	(Khazaeli <i>et al.</i> , 2015)
- Diffusion coefficient of HSO ₄ ⁻	$D_{HSO_4^-}$	1.33 x 10 ⁻⁹ m ² s ⁻¹	(Khazaeli <i>et al.</i> , 2015)

Mass transfer coefficient across the membrane

- Migration coefficient of V ²⁺	$k_{V^{2+}}^{Mig}$	7.0 x 10 ⁻⁷ m V ⁻¹ s ⁻¹	(Schafner <i>et al.</i> , 2018)
- Migration coefficient of V ³⁺	$k_{V^{3+}}^{Mig}$	1.7 x 10 ⁻⁶ m V ⁻¹ s ⁻¹	(Schafner <i>et al.</i> , 2018)
- Migration coefficient of VO ²⁺	$k_{VO^{2+}}^{Mig}$	1.0 x 10 ⁻⁷ m V ⁻¹ s ⁻¹	(Schafner <i>et al.</i> , 2018)
- Migration coefficient of VO ₂ ⁺	$k_{VO_2^+}^{Mig}$	1.0 x 10 ⁻⁷ m V ⁻¹ s ⁻¹	(Schafner <i>et al.</i> , 2018)
- Electro-osmosis coefficient	k^{Eosm}	8.0 x 10 ⁻⁸ m V ⁻¹ s ⁻¹	(Schafner <i>et al.</i> , 2018)
- Hydraulic pressure coefficient	k^{Hydr}	1.2 x 10 ⁻⁷ m bar ⁻¹ s ⁻¹	(Schafner <i>et al.</i> , 2018)

Electrochemistry

- Standard potential for the V ²⁺ /V ³⁺ reaction	E_n^0	-0.255 V	
- Standard potential for the VO ²⁺ /VO ₂ ⁺ reaction	E_p^0	1.004 V	
- Standard potential for the HER	E_{HER}^0	0 V	(Shah <i>et al.</i> , 2010)
- Standard potential for the OER	E_{OER}^0	1.229 V	(Al-Fetlawi <i>et al.</i> , 2010)

- Standard rate constant for the positive electrode	$k_{0,p}$	$6.8 \times 10^{-7} \text{ m s}^{-1}$	(C. L. Chen <i>et al.</i> , 2014)
- Standard rate constant for the negative electrode	$k_{0,n}$	$2.6 \times 10^{-6} \text{ m s}^{-1}$	
- Exchange current density of OER	$j_{o,OER}$	$1.0 \times 10^{-9} \text{ A m}^{-2}$	(Al-Fetlawi <i>et al.</i> , 2010)
- Reference temperature	T_{ref}	298.15 K	
Gas constant	R	$8.314 \text{ J mol}^{-1} \text{ K}^{-1}$	
Faraday's constant	F	$96,485 \text{ A s mol}^{-1}$	

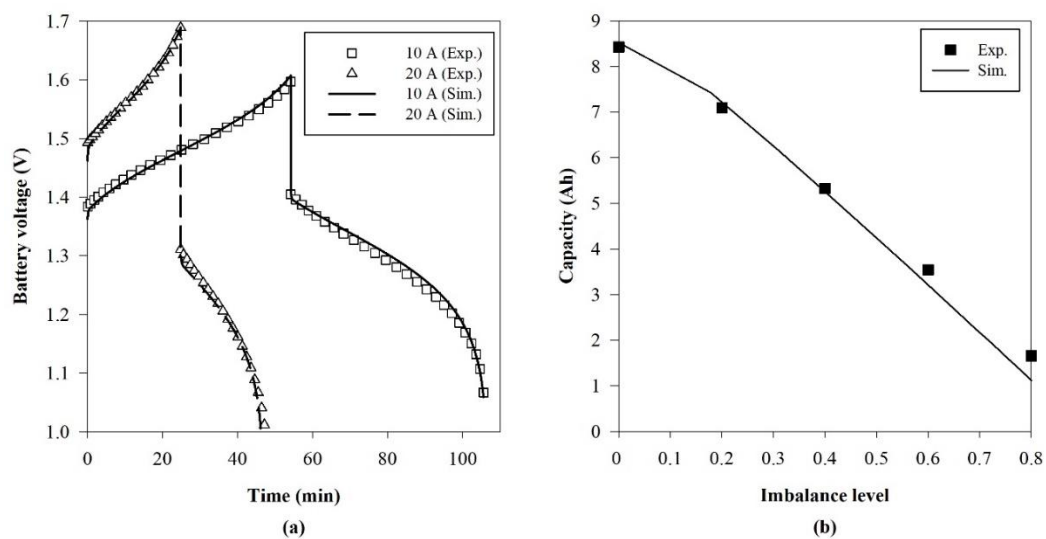


Figure 4.5 Comparison of the simulation results with the experimental data (a) charge-discharge characteristic curve. (b) effect of imbalance level on discharge capacity (Ngamsai and Arpornwichanop, 2015a).

CHAPTER V

PERFORMANCE ANALYSIS OF VANADIUM REDOX FLOW BATTERY UNDER THE ELECTROLYTE IMBALANCE CONDITIONS

This chapter presents the effect of electrolyte imbalance and the operating parameters on the vanadium redox flow battery performance. The different electrode and membrane materials are considered for representing the cause of electrolyte imbalance from the gassing side reactions and cross contamination problem, respectively. In addition, the effect of key operating parameters such as the current density, active species concentration in electrolyte solution, electrolyte temperature and electrolyte flow rate on the battery overpotentials, rate of gassing side reaction, discharge power and capacity and battery efficiencies are analyzed using the proposed dynamic model of vanadium redox flow battery.

5.1 Effect of the electrolyte imbalance

The decrease in VRFB capacity during long-term operation is attributed to the electrolyte imbalance that occurs during the charging-discharging process. The ion exchange membrane cannot totally prevent the vanadium ions from diffusing across the membrane due to the concentration gradient between the half-cells. Moreover, the diffused ions go on to react with other ions in the opposite half-cell, thereby contributing to the self-discharge reaction. This phenomenon leads to an increasing rate of imbalance, creating a build-up of vanadium ions at one half-cell and a decrease in ions in the other. The gassing side reactions, corresponding to the HER and OER in the negative and positive half-cells, respectively, also contribute towards this imbalance. The gassing side reactions that occur at the electrode surface during the charging process consume some of the applied current, thereby enhancing the rate of capacity decay. To further observe the effect of ionic diffusion and the gassing side reactions, several types of electrode materials and membranes were investigated using the following operating conditions: the battery was operated at a current density of 120 mA cm^{-2} with an electrolyte flow rate of 2 mL s^{-1} and a constant temperature of 298.15 K .

The initial electrolyte conditions in both half-cells comprised a 1.6 M vanadium in 4 M H₂SO₄. The experimental kinetic data for the HER and redox reactions in negative half-cells with different felt electrodes (Schweiss *et al.*, 2016) and the diffusion coefficients of the different membranes (Tang *et al.*, 2011) are summarized in Tables 5.1 and 5.2, respectively. The CMV and Nafion 115 are cation exchange membrane, while AMV is anion exchange membrane. For electrode type 1, carbon felt based on cellulose (rayon) precursor which was treated with high temperature of 2000 °C under argon atmosphere and were brought to thermal surface oxidation with air at 750 °C for 5 min. For electrode type 2 and 3, carbon felt based on polyacrylonitrile (PAN) and this type has a low value of the interlayer spacing of crystalline domain, while has a high graphitic domain; thus, PAN based material show the high electronic conductivity.

Table 5.1 Kinetic data for the hydrogen evolution reaction (HER) and redox reactions in negative half-cells with different electrode materials (Schweiss *et al.*, 2016)

Electrode	BET	Conductivity	k_0 V ²⁺ /V ³⁺	HER	
	(m ² g ⁻¹)	(S m ⁻¹)	(m s ⁻¹)	j_0 (A m ⁻²)	$1-\beta$
Type 1	6.5	100	2.1×10^{-5}	2.5×10^{-2}	0.34
Type 2	0.5	310	6.5×10^{-7}	6.9×10^{-1}	0.21
Type 3	1.2	460	2.6×10^{-6}	6.6×10^{-4}	0.25

Table 5.2 Vanadium ion diffusion coefficients for different membrane types (Tang *et al.*, 2011)

Membrane	Vanadium ion diffusion coefficient (cm ² min ⁻¹)			
	k_2^{Diff}	k_3^{Diff}	k_4^{Diff}	k_5^{Diff}
Selemion AMV	2.94×10^{-4}	1.8×10^{-4}	7.8×10^{-5}	2.16×10^{-4}
Selemion CMV	2.64×10^{-3}	5.96×10^{-4}	1.67×10^{-3}	1.041×10^{-3}
Nafion 115	5.76×10^{-3}	2.1×10^{-3}	6.26×10^{-3}	3.84×10^{-3}

Table 5.3 Case studies for different types of electrodes and membrane materials

Case	Electrode	Membrane
1	Type 1	Selemion AMV
2		Selemion CMV
3		Nafion 115
4	Type 2	Selemion AMV
5		Selemion CMV
6		Nafion 115
7	Type 3	Selemion AMV
8		Selemion CMV
9		Nafion 115

The efficiencies (Figure 5.1) of the different batteries made from different materials (Table 5.3) reveal that the coulombic efficiency depends on both the membrane type and electrode material. The high diffusion of the vanadium ions causes a self-discharge reaction. Moreover the current loss from the HER consumes some applied current during battery charging, leading to a reduction in the coulombic efficiency. Regarding the electrode material, the use of a Type 3 electrode (Cases 7–9) afforded the highest coulombic efficiencies for all the membrane types. This occurred because this electrode type displays the lowest HER exchange current density. When considering the membrane type, the use of an AMV membrane (Cases 1, 4, and 7) produced the highest coulombic efficiencies. These membranes exhibit the lowest vanadium diffusion coefficient, thereby minimizing the loss caused by the self-discharge reaction. Furthermore, the voltage efficiency varies with the different electrode materials due to their different electronic conductivities. Thus, due to the increased voltage efficiency, the high electronic conductivity of the Type 3 electrode creates a low ohmic overpotential. When considering the coulombic and voltage

efficiencies, the use of a Type 3 electrode and an AMV membrane in the VRFB produced the highest energy efficiency.

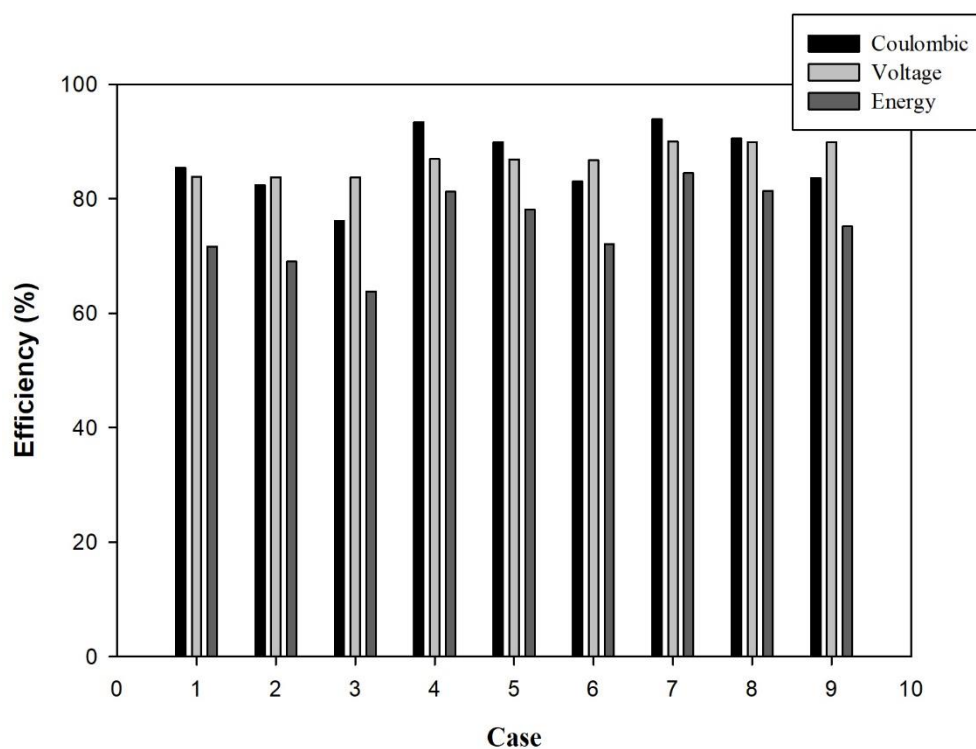


Figure 5.1 Efficiencies of vanadium redox flow batteries (VRFB) with different electrode and membrane types.

The capacities of the different VRFBs during a series of uninterrupted charging-discharging cycles are illustrated in Figures 5.2a-c. As the effect of the gassing side reactions is also considered, the capacity loss highly depends on the electrode material. For the Type 1 and 2 electrodes, the capacity degradation trend of VRFB with different membrane types is similar, according to the vanadium ion diffusion coefficients. The VRFB capacity in Cases 4 to 6 continuously decreases along the 100 cycles, resulting in a high loss in desirable current via the HER in the Type 2 electrode. On the other hand, in Type 3 electrodes, the trend in capacity loss differs with the use of AMV and CMV membranes. Although the CMV membrane exhibits a relatively high initial rate of capacity drop, the capacity does not change further during the 100 cycles. Conversely, the capacity of the AMV membrane incessantly decreases throughout 200 cycles. In this system, the different transfer rates of the four vanadium ions continue to

create a vanadium concentration build-up in the positive half-cell, causing a reduction in the vanadium concentration in the negative half-cell. Interestingly, because the current losses from the HER and OER are lower during the charging processes, the diffusion across the membrane can reach a steady state as the battery capacity is constant (Tang *et al.*, 2011). In addition, the highest degradation occurs in Case 6, which uses a Type 2 electrode and a Nafion 115 membrane. Because of the great current loss from the HER in the Type 2 electrode and the effect of the high cross-contamination in the Nafion 115 membrane, a capacity of ~24% was observed after only 50 charging-discharging cycles. This rate of capacity loss is moderately consistent with the results reported by Skyllas-Kazacos and McCann (2015), namely, a 1% loss in capacity per cycle when an applied current of only 1% is consumed by the HER during each charging process.

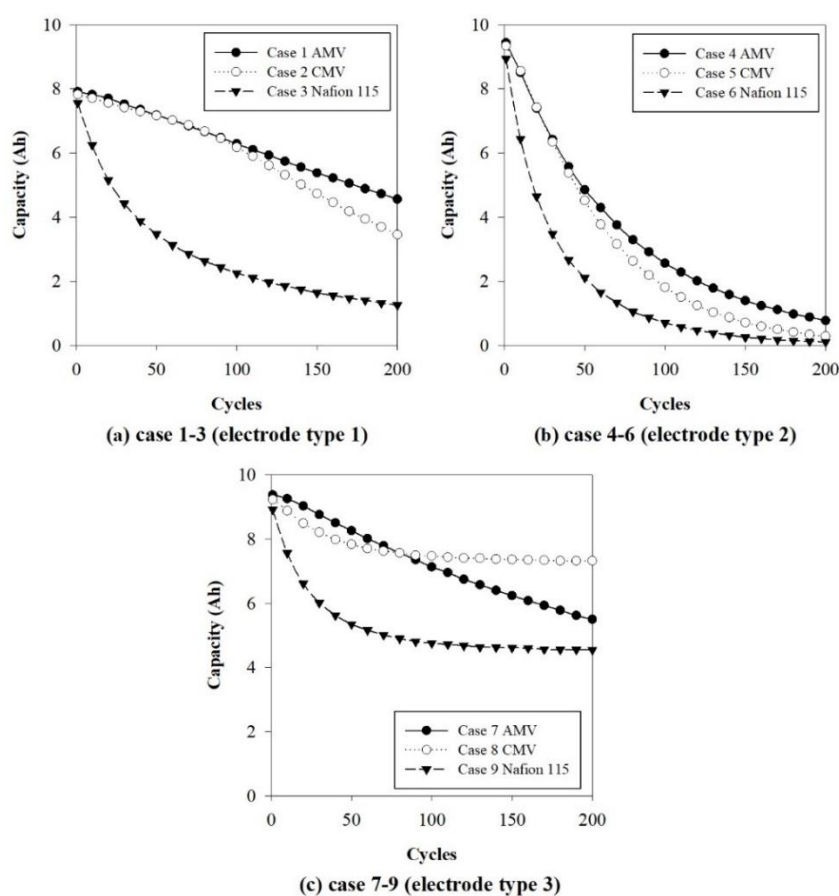


Figure 5.2 Capacity of vanadium redox flow batteries (VRFB) with different electrode and membrane types.

Figure 5.3a and b present the concentration of vanadium in each oxidation state in a VRFB operating for 200 cycles (Case 7). At the upper voltage limit, the concentrations of the VO_2^+ and V^{2+} ions decrease, while that of the VO^{2+} ions increase. This is attributed to the high V^{2+} ion diffusion from the negative half-cell, which causes a high conversion of VO_2^+ to VO^{2+} ions according to the self-discharge reaction. As a result, the state of charge (SOC) of the positive half-cell decreases significantly over that of the negative half-cell. Moreover, there is an accumulation of V^{2+} ions during the end of each cycle. This occurs because the conversion of V^{2+} to V^{3+} ions during the discharging process of the negative half-cell is limited by the reduction of the VO_2^+ ions in the positive half-cell. This reaction produces the necessary electrons for the oxidation of V^{2+} to V^{3+} ions in the negative half-cell. Thus, the SOC of both half-cells is changed by the variation in the vanadium ion concentration. The margin between the upper and lower SOC represents the energy of the battery that can be stored and discharged. Notably, the maximum SOC in the positive half-cell decreases from the initial 92% to 45% due to the depletion in VO_2^+ ions. Conversely, the minimum SOC in the negative half-cell increases from an initial 7% to 30% due to the accumulation of V^{2+} ions (Figure 5.3c). On the other hand, if the HER is high, the oxidation of VO^{2+} to VO_2^+ ions are limited by the high concentration of V^{2+} ions in the negative half-cell. Since the cathodic current is partially consumed by the HER, the conversion of the active species in the negative half-cell (V^{3+} to V^{2+} ions) is lower than that observed in the positive half-cell (VO^{2+} to VO_2^+ ions). This results in an accumulation of VO_2^+ ions due to the limited V^{2+} ion concentration in the negative half-cell, which is depleted before the VO_2^+ ions in the discharging process.

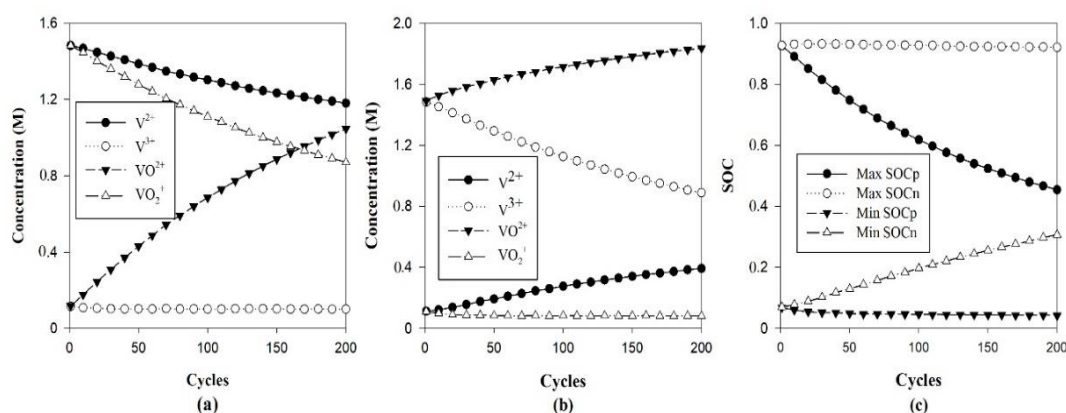


Figure 5.3 Vanadium concentration and state of charge (SOC) of the electrolyte at the upper and lower limit voltages during 200 cycles.

5.2 Effect of the operating conditions on battery performance

A VRFB comprising a Type 3 electrode and an AMV membrane was chosen as a case study: (1) to elucidate the effect of the operating conditions on the battery performance, influenced by the gassing side reactions and vanadium ion diffusion and (2) to determine the optimal operating conditions for long-term operation. The studied parameters are summarized in Table 5.4.

Table 5.4 Operating parameters for the performance investigation

Parameters	Studied range	Standard value
Current density	40–200 mA cm ⁻²	120 mA cm ⁻²
Vanadium concentration	1.4–2.0 M	1.6 M
Proton concentration	2–5 M	4 M
Temperature	298.15–318.15 K	298.15 K
Electrolyte flow rate	1–5 mL s ⁻¹ cm ⁻²	2 mL s ⁻¹

5.2.1 Current density

This section presents the battery voltages during charging and discharging under various applied current densities. The battery is charged and discharged until the battery voltage reaches the upper and lower voltage limits, 1.7 V and 1.1 V, respectively. A high current density causes a faster increase and decrease in the battery voltage during the respective charging and discharging processes. This suggests that a shorter time is necessary for the battery to become fully charged and discharged. However, due to the different battery overpotentials (ohmic, concentration, and activation overpotentials), the SOC at the upper- and lower-limit voltages, at different current densities, are not equal as shown in Figure 5.4.

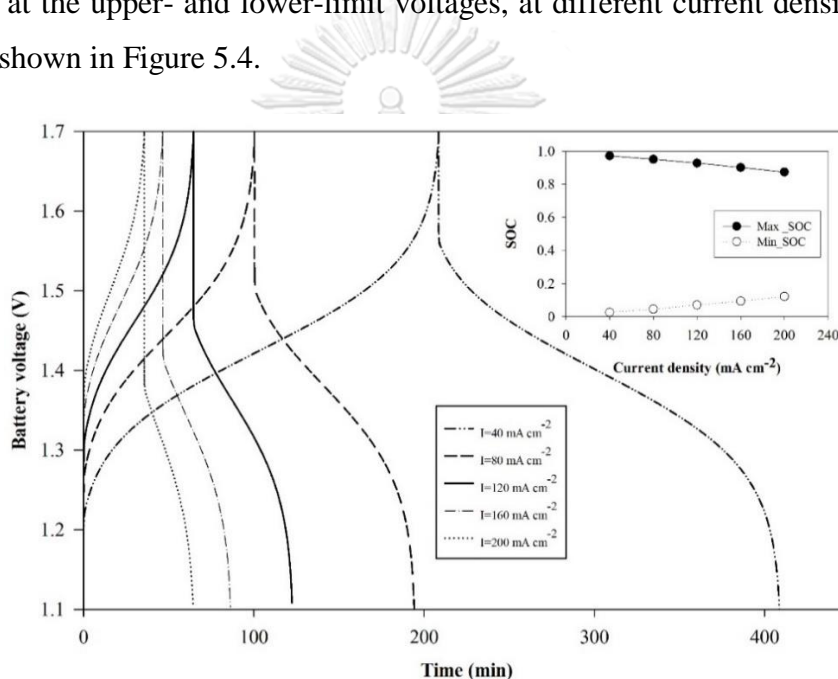


Figure 5.4 Effect of current density on battery voltage curve with maximum and minimum SOC at voltage limit.

The effect of the current density on the total overpotentials of both electrodes at SOC values of 0.25, 0.5, and 0.75 is illustrated in Figure 5.5a. Each type of overpotential increases when the current density is increased from 80 to 160 mA cm⁻². Particularly, the ohmic overpotential exhibits the highest change with the increase in current density, according to the Ohm's law. Moreover, this overpotential is less dependent on the SOC when low current densities are applied; however, it slightly decreases with an increase in SOC at high current densities due to the variation in the

electrolyte conductivity. Thus, when a high current density is applied, the rate of proton increase is significantly raised, resulting in an increase in electrolyte conductivity. Interestingly, the activation overpotential at SOC values of 0.25 and 0.75 are equal and higher than that observed at an SOC of 0.5. This is due to the effect of the exchange current density, which is a function of the rate of reaction, concentration of the redox vanadium couple, and charge transfer coefficient. At the beginning and end of the charging process, the concentration of one of the vanadium couple ions is close to zero. Therefore, the exchange current density has a low value, leading to an increment in the activation overpotential. As the value of the charge transfer coefficient approaches 0.5, the minimum activation overpotential is observed at an SOC of 0.5. Under these conditions, the concentration of the vanadium couple is at its highest multiple value, thereby producing the highest exchange current density. In addition, the concentration overpotential is considerably raised with an increase in both the current density and SOC. The latter behavior results from the depletion of vanadium reactants at the end of the charging and discharging processes, contributing to a sharp increment in the concentration overpotential at an SOC of 0.75. Furthermore, because of the mass transfer limit, the concentration overpotential depends on the applied current density. If the battery is charged or discharged at a high current density, a significant amount of vanadium reactant is consumed by the reaction at the electrode surface. Thus, if the mass transfer of the reactant species, from the bulk electrolyte to the electrode surface, is constant and does not meet the required conversion, a concentration gradient is developed between the former boundary. The current loss from the gassing side reactions are therefore enhanced according to the increase in overpotential (Figure 5.5b). The current loss from HER increases sharply at the highest SOC value, and the initial SOC for OER was decreased and occur at the lower SOC value. This behavior can be explained as follows: HER occurs when the voltage at the negative electrode is more negative than the standard potential of the HER. The standard potential of the V^{2+}/V^{3+} redox couple is -0.26 V, while that of hydrogen evolution is 0 V. Thus, HER can inherently occur over the whole range of SOC values during the charging process. On the other hand, OER only takes place when the voltage at the positive electrode is more positive than the standard potential of the OER. The standard potential of the VO^{2+}/VO_2^+ redox couple is 1.0 V, while that of oxygen evolution is 1.229 V. Hence,

oxygen evolution only arises at the higher SOC where the positive half-cell voltage, summation of the positive standard potentials, and overpotential, are higher than the standard potential of the OER. Thus, the positive overpotential increases and the initial SOC of OER decreases when the applied current density is high.

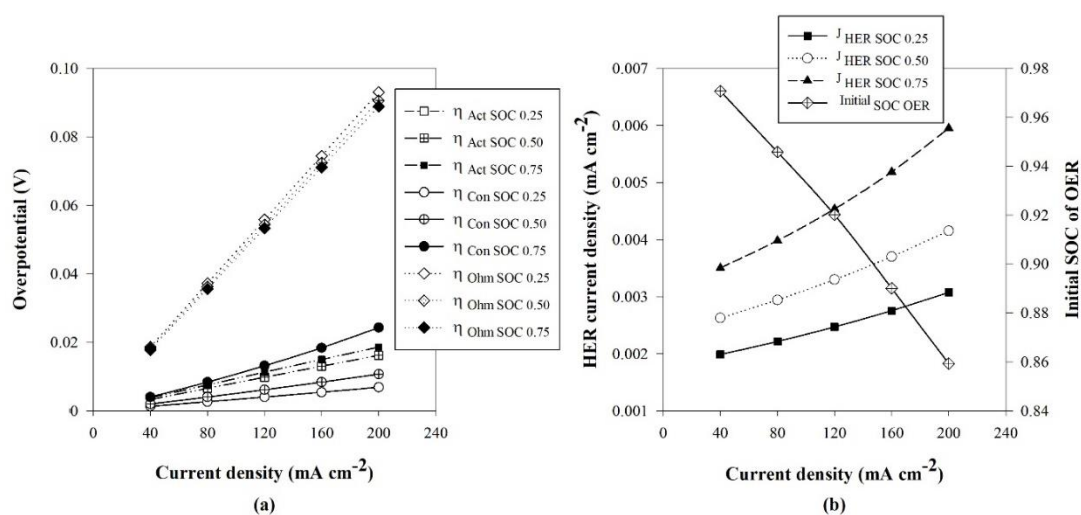


Figure 5.5 Effect of current density on (a) battery overpotentials and (b) HER current density and initial SOC of OER.

The variation in battery power, capacity, and efficiency was studied to investigate the effect of the current density on battery performance. The discharge capacity of the battery decreases by $\sim 28.2\%$ due to the reduction in the SOC window at the voltage limits. A significant increase in the discharge power (~ 4.6 -fold) is observed with an increase in current density from 40 to 200 mA cm^{-2} as shown in Figure 5.6a. On the other hand, the energy efficiency decreases from 93 to 68% as a result of the overpotentials, which increase the charge voltage and decrease the discharge voltage. Thus, the ratio of the discharge energy to the energy required for charging the battery is decreased. Moreover, the trend in system efficiency is similar to the energy efficiency through the current density range 40 – 200 mA cm^{-2} . However, if the current density at which the battery is operated is too low ($< 40 \text{ mA cm}^{-2}$), the system efficiency will decrease with the applied current. At a low current density, the battery requires a longer time to charge and discharge fully. Thus, the energy consumed by the pump also increases, leading to a reduction in the system efficiency (Figure 5.6b). Although a current density of 40 mA cm^{-2} achieved a high discharge capacity in the early cycles, it

produced the lowest capacity after 80 cycles. Moreover, the rate of capacity degradation decreased with an increase in current density. Because the battery was operated for a shorter time, a decrease in both the mole diffusion and self-discharge reaction was observed. Thus, the effect of using a low current density on the capacity loss is only apparent in long-time monitoring as presented in Figure 5.7. As a result, it can be concluded that a relatively higher current density is preferred to achieve the desired battery discharge power and short application time. Conversely, a low current density can be used for operations with no power and time constraints.

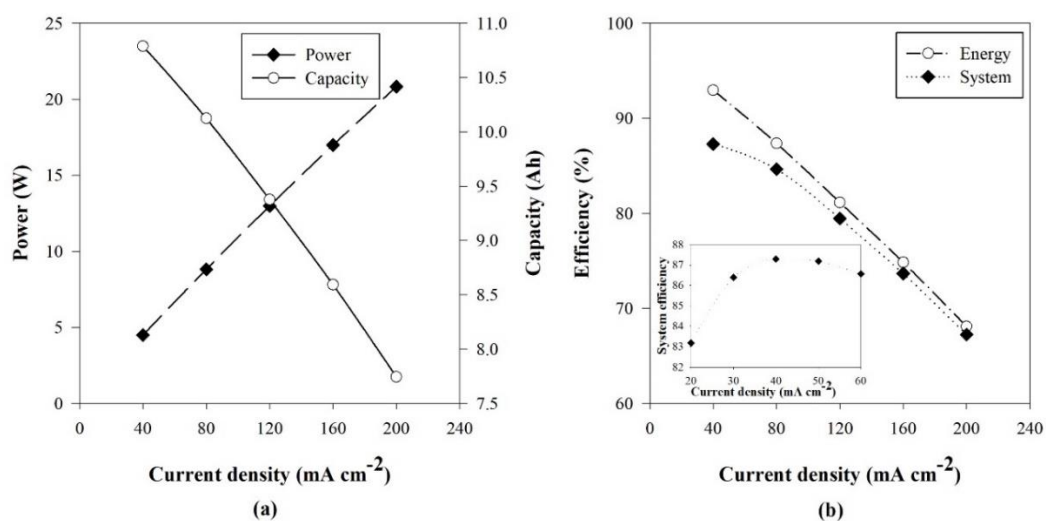


Figure 5.6 Effect of current density on (a) battery power and capacity and (b) battery efficiency.

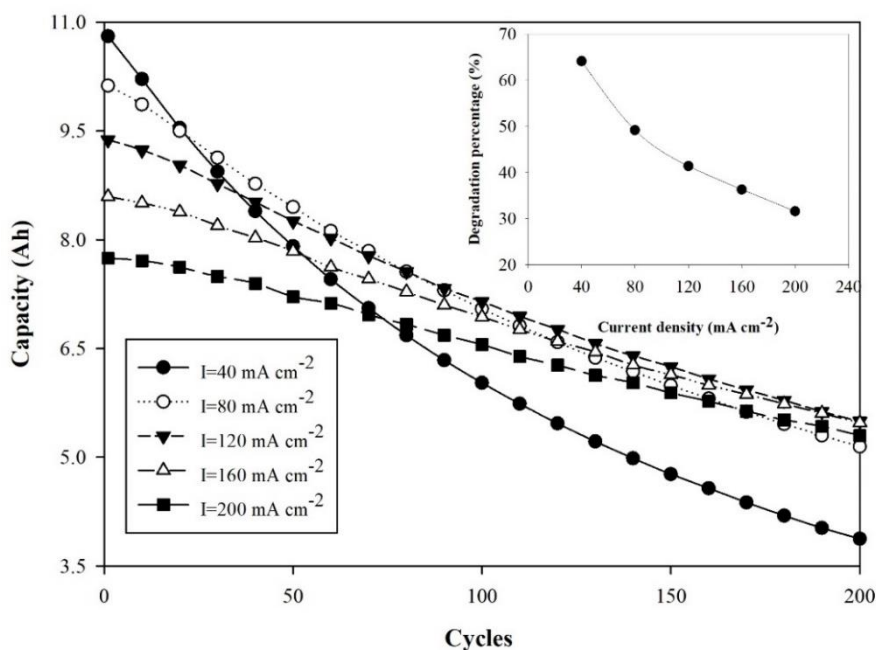


Figure 5.7 Effect of current density on long-term capacity variation.

5.2.2 Vanadium and proton concentrations

The effect of the initial vanadium and proton concentration on the battery voltage and performance as well as the capacity decay in long-term charging and discharging is next considered. The effect at different initial vanadium concentrations of 1.4, 1.6, 1.8, and 2.0 M were investigated according to the range of vanadium concentrations used for all-VRFB (M. Skyllas-Kazacos *et al.*, 2013). The proton concentration range 2.0–5.0 M was investigated because the solubility of vanadium is reduced at higher-acid concentrations (Skyllas-Kazacos and McCann, 2015). Notably, the time for charging and discharging the battery increases with an increase in the initial vanadium concentration, indicating that more energy could be stored at increased vanadium concentrations as presented in Figure 5.8.

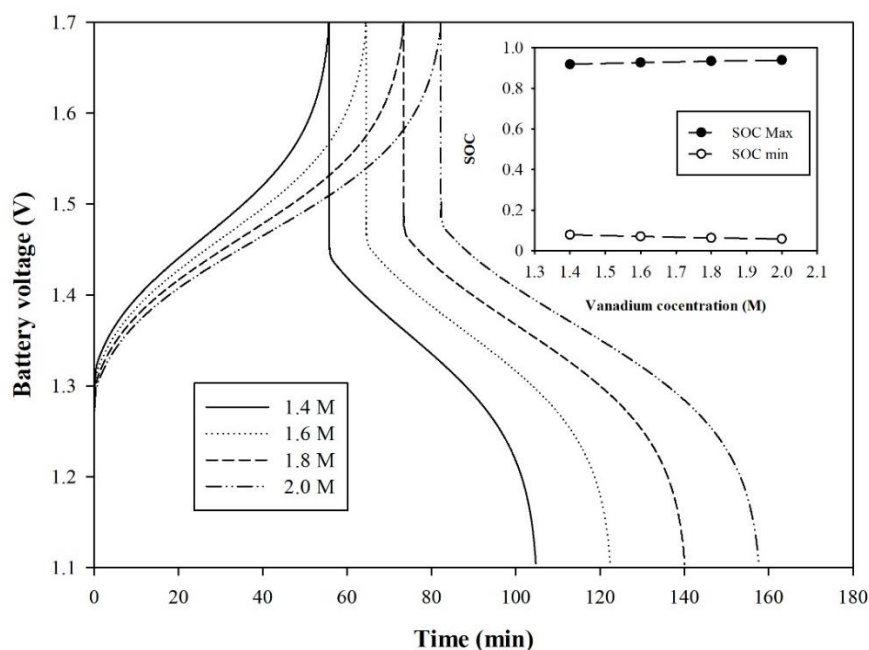


Figure 5.8 Effect of vanadium concentration on battery voltage curve with maximum and minimum SOC at voltage limit.

During charging, the different overpotentials in both the electrode and electrolyte conductivity are reduced with an increase in the vanadium concentration Figure 5.9a. This can be clarified as follows: an increase in the vanadium concentration improves the exchange current density and mass transfer, leading to a reduction in the activation and concentration overpotentials, respectively. Moreover, the ohmic overpotential is decreased due to the increment in electrolyte conductivity at high vanadium concentrations. Notably, except for the concentration overpotential at an SOC of 0.75, an increase in the vanadium concentration does not significantly affect the overpotential. This is due to the effect of the mass transfer limit as mentioned above. The effect of the proton concentration on the battery performance was also investigated. In their study, Yang *et al.* (2015) reported that the ohmic overpotential was reduced and the standard potential increased when the initial electrolyte comprised a high proton concentration. The variation of all the overpotentials with proton concentration is displayed in Figure 5.9b. The results confirm that an increment in proton concentration only affects the reduction in ohmic overpotential, while the activation and concentration overpotentials do not change over the tested SOC range.

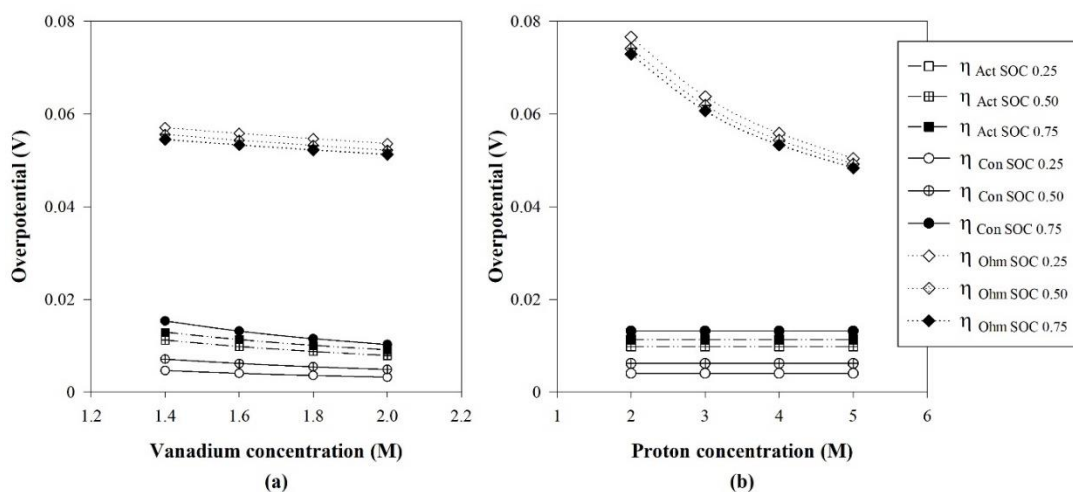


Figure 5.9 Effect of (a) vanadium concentration and (b) proton concentration on overpotentials.

The effect of the vanadium and proton concentrations on the power and capacity in the discharging process and the battery efficiency are presented in Figure 5.10a and b. When compared to the increase in proton concentration, the increase in vanadium concentration affords a greater increase in battery capacity. This implies that the discharge time of the battery can be improved by applying a high vanadium concentration. Conversely, compared to the vanadium concentration, the proton concentration displays a more marked effect on the battery power. Although using high vanadium and proton concentrations can increase the electrolyte conductivity, increasing the proton concentration exhibits a greater impact on the open circuit voltage than the vanadium concentration according to Nernst equation. As a result, the voltage efficiency trend of the increasing proton concentration is steeper than that of the increasing vanadium concentration. Nevertheless, the energy efficiency trend in both cases is analogous because of the abovementioned controversial effects of the battery capacity and power.

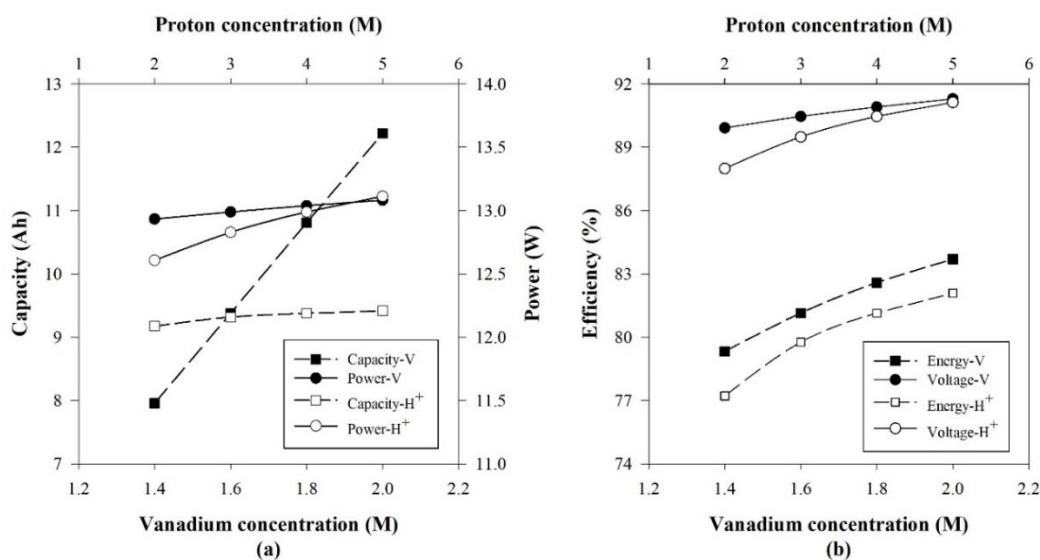


Figure 5.10 Effect of vanadium and proton concentration on (a) battery capacity and power and (b) battery efficiencies.

Figure 5.11 a and b show the effect of vanadium and proton concentration on the gassing side reactions. The current loss from the HER at each SOC also decreases with an increase in the initial SOC of the OER. This results in the reduction of all the overpotentials when a high initial vanadium concentration is applied. On the other hand, an increase in the proton concentration does not reduce the HER current density. Moreover, although the ohmic overpotential is reduced, the initial SOC of the OER decreases because the proton concentration also affects the standard potential of the HER and OER. The variations of the standard potentials of the V^{2+}/V^{3+} redox couple with the HER at the negative half-cell and the VO^{2+}/VO_2^+ couple with the OER at the positive half-cell are presented in Figure 5.12a and b. According to the Nernst equation, an increase in proton concentration, from 2 to 5 M, does not affect the standard potential of the V^{2+}/V^{3+} redox couple. However, the standard potential of the HER increases (more positive), thereby increasing the gap between the standard potentials. Owing to the opposing effects of the increasing HER standard potential and the reduction in ohmic overpotential, when a high proton concentration is applied, the HER current density trend can be increased or decreased, depending on various factors such as the electrode material. At the positive half-cell, an increase in the proton concentration increases the standard potentials of both the VO^{2+}/VO_2^+ redox couple and the OER. The

interval between the standard potentials applied with 2 M and 5 M protons dose not change considerably. Nevertheless, the initial SOC of the OER gradually decreases from 0.925 to 0.917 because the high proton concentration significantly affects the increase in standard potential of the $\text{VO}^{2+}/\text{VO}_2^+$ redox couple rather than that of the OER. This can be observed by the slope between the standard potentials.

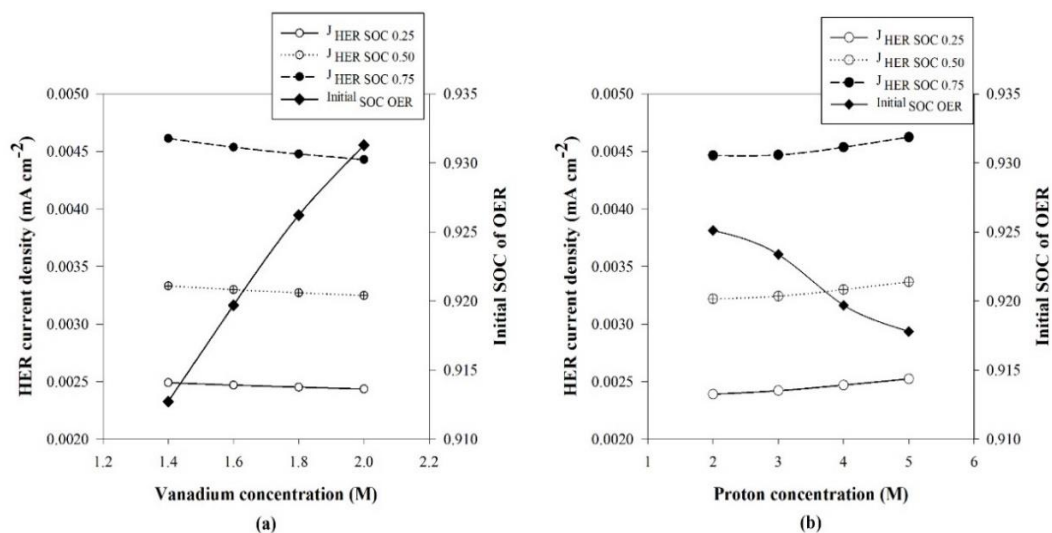


Figure 5.11 Effect of (a) vanadium concentration and (b) proton concentration on HER current density and initial SOC of OER.

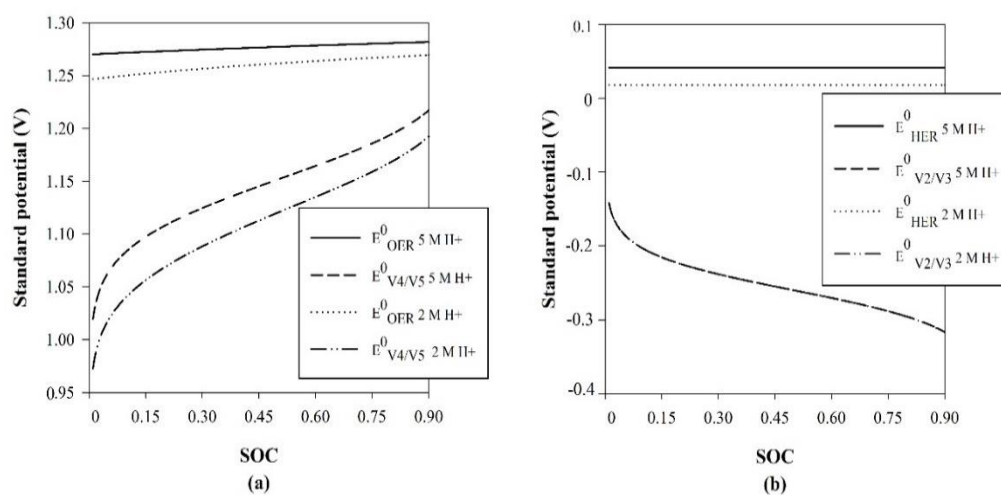


Figure 5.12 Effect of proton concentration on standard potential of (a) redox couples $\text{VO}^{2+}/\text{VO}_2^+$ and OER (b) redox couples $\text{V}^{2+}/\text{V}^{3+}$ and HER.

The long-term effects of the vanadium and proton concentrations on the battery capacity are illustrated in Figure 5.13a and b. The data reveal that the high vanadium concentrations produce greater capacities than the lower concentrations throughout the 200 cycles. However, the rate of capacity loss also increases when a high vanadium concentration is applied. This contributes to the increased vanadium ion diffusion rate across the membrane with an increase in the vanadium concentration. Although an increase in the proton concentration can increase the current loss from the HER and OER, the rates of capacity loss, when different proton concentrations are applied, are similar at the end of 200 cycles. The effects of a high current loss from the HER and OER due to the application of high proton concentrations appear in early 100 cycles. Since the rate of the HER depends on the proton concentration, the conversion of protons to hydrogen gas is increased at high initial proton concentrations. Thus, due to the total HER and OER rates in the rest cycles, the remaining proton concentrations after 100 cycles are similar for the different initial concentrations.

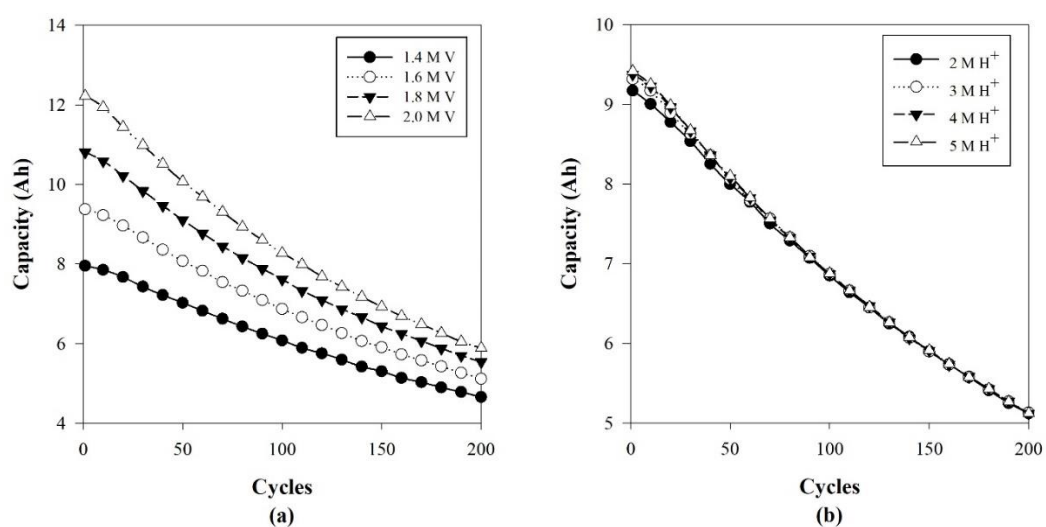


Figure 5.13 Effect of (a) vanadium and (b) proton concentration on long-term capacities.

5.2.3 Operating temperature

The electrolyte temperature of the VRFB depends on several factors during the charging-discharging process: (1) ohmic heat loss, the most important effect that causes an increase in battery temperature; (2) the heat generated from the self-discharge reactions as the vanadium ions diffuse through the membrane; (3) the heat from the electrochemical reaction, which is proportional to the charging-discharging current and concentration of the active species; and (4) heat transfer between the system and the surroundings, which depends on the locations of the battery setting. In this part of the study, the battery was operated at different constant temperatures (25 to 45 °C). The variation in the electrolyte temperature affects the efficiency and performance of the VRFB. In detail, the rise in electrolyte temperature increases the rate of the electrochemical reaction, leading to a reduction in the activation overpotential. This improves the voltage efficiency. In contrast, the coulombic efficiency decreases as the rate of vanadium ion diffusion increases with an increment in the electrolyte temperature. Thus, the overall energy efficiency, a function of the coulombic and energy efficiencies, achieves the highest value at the optimal operating temperature. Various variables, such as the membrane type, electrode material, and cell design, create different optimal temperature conditions (Skylas-Kazacos and McCann, 2015). This section studies the effect of different electrolyte temperatures corresponding to the different types of membranes. The battery capacity, power and the efficiency of three types of membranes (AMV, CMV and Naffion 115) are illustrated in Figure 5.14a and b. For all the membrane types, as the operating temperature increases, the reduction in the activation overpotential enhances the discharge power and decreases the discharge capacity. However, the rate of capacity drop depends on the diffusion rate of the vanadium ions. Therefore, the Nafion 155 membrane was very sensitive to the operating temperature. This was attributed to the use of the same electrode material, whereby the trend in energy efficiency was affected by the variation in the coulombic efficiency. Thus, the optimal temperature for the AMV, CMV, and Nafion 115 membranes were established as 35, 30, and 25 °C. In contrast, the optimal temperature did not produce the best long-term performance capacity (Figure 5.15). Since the diffusion rate of the vanadium ions vary with the electrolyte temperature, the rate of capacity degradation increases with the increment of the operating temperature.

Therefore, if the objective for the operating the battery is a long battery life cycle, the operating temperature should be low as possible.

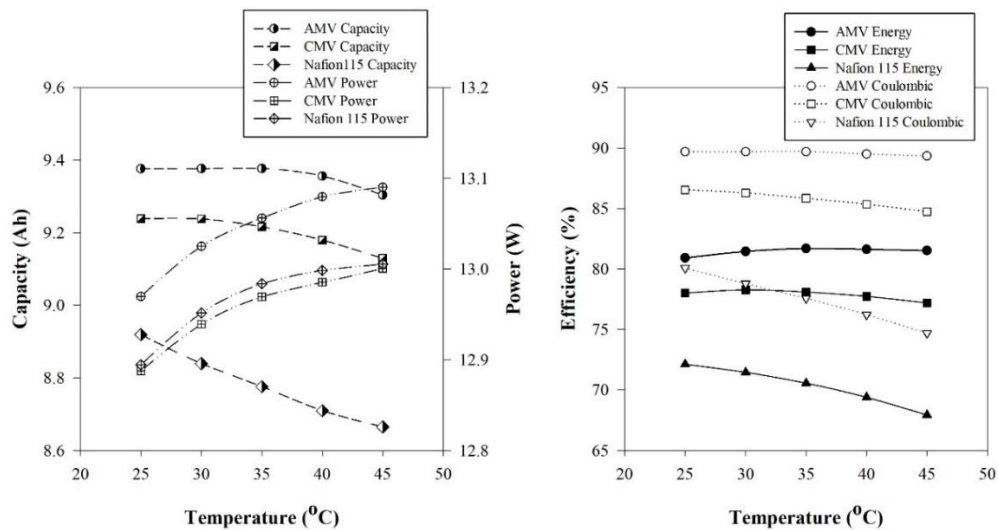


Figure 5.14 Effect of operating temperature on (a) battery capacity and power and (b) battery efficiency.

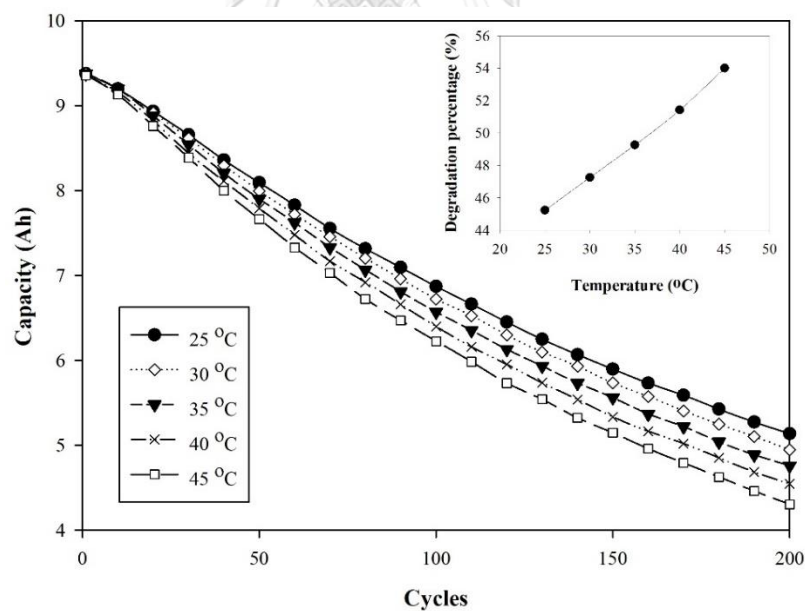


Figure 5.15 Effect of operating temperature on long-term capacity variation of AMV membrane.

Interestingly, an increase in the operating temperature always increases the exchange current density of the HER and OER; however, it can also reduce the HER and OER overpotentials. As a result, the current loss of the gassing side reaction depends on both the exchange current density and its overpotential. For the Type 3 electrode, the current loss from the HER decreases with a rise in the operating temperature because their exchange current density is low but if the temperature is too high, the current loss from HER is increased. Thus, the effect of the overpotential reduction is more significant than the increment of the exchange current density in medium range of temperature. On the other hand, if the exchange current density of the HER is high (Type 2 electrode), the current loss of the HER is enhanced when the operating temperature is increased (Figure 5.16). Therefore, the effect of the operating temperature on the current loss from the gassing side reaction will depend on the exchange density, surface area, and conductivity of the electrode material.

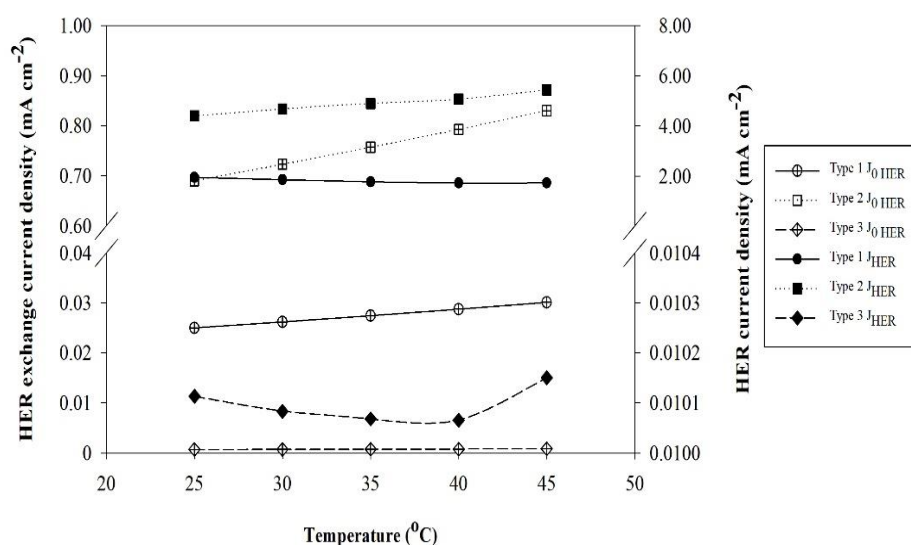


Figure 5.16 Effect of operating temperature on HER current density at upper limit voltage.

5.2.4 Electrolyte flow rate

In this section, the effect of different electrolyte flow rate electrolyte flow rate on battery performance are studied. The various constant electrolyte flow rates are applied for charging-discharge process. The concentration overpotential is decreased because the mass transfer of reactant can be enhanced by increasing the electrolyte flow rate. However, the activation and ohmic overpotential did not change with the electrolyte flow rate as shown in Figure 5.17a. Thus, the HER current density was slightly reduced, while the initial SOC of OER is less increase as presented in Figure 5.17b. Moreover, the reduction of concentration overpotential can expand charge-discharge time to voltage limit leading to the increment of battery capacity and power according to Figure 5.18a. Consequently, the battery energy efficiency always increase with the electrolyte flow rate. However, the system efficiency does not increase when operates at high electrolyte flow rate because the pump consumes more power at high flow rate. Therefore, the net discharge power of the battery has to subtract the pump power loss for discharging process while it is included for charging process. The effect of electrolyte flow rate on the system efficiency are shown in Figure 5.18b. It can be noticed that the optimal value of electrolyte flow rate is approximate 2 ml s^{-1} , nevertheless the optimal flow rate of battery depends on the cell structure as well as electrolyte condition such as the electrolyte viscosity.

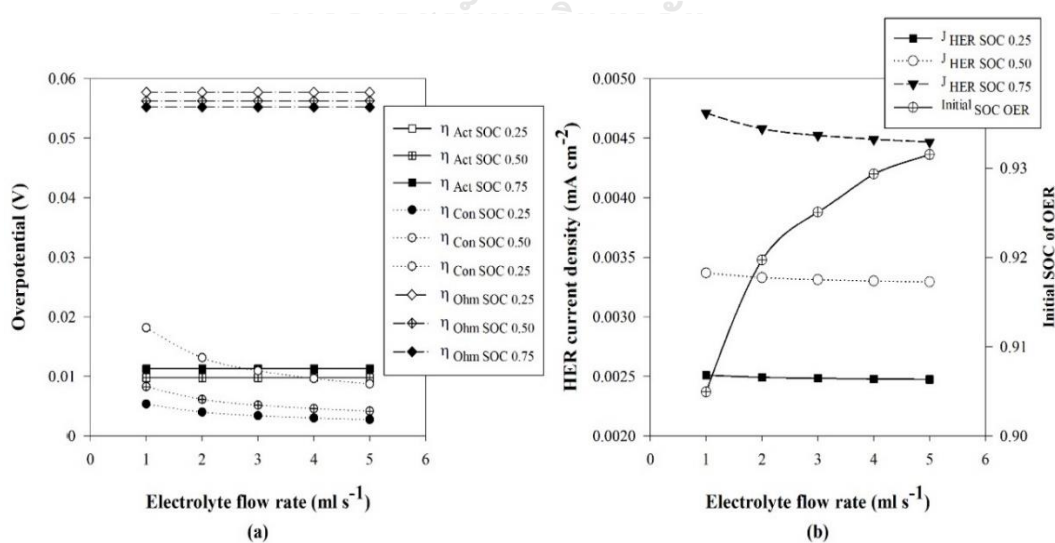


Figure 5.17 Effect of electrolyte flow rate on (a) overpotentials and (b) HER current density and initial SOC of OER.

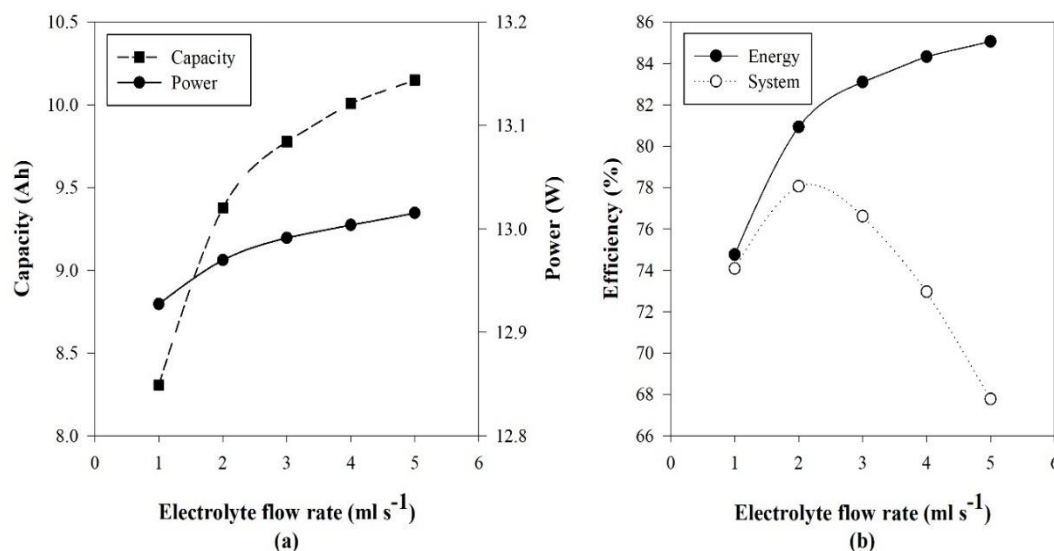


Figure 5.18 Effect of electrolyte flow rate on (a) battery capacity and power and (b) battery efficiency.

According to the concentration overpotential change with the current density and SOC, the variable flow rate approach is proposed for manipulation the electrolyte flow. As mention in the effect of current density on overpotential, the mass transfer of active species decreases at high SOC due to the low concentration of reactant species. Moreover, if battery is charged and discharged with the high current density and constant electrolyte flow rate, the mass transfer of reactant will not meet requirement for conversion. As a result, the electrolyte flow rate has to increase for improvement the mass transfer limit when applied with high current density and at high SOC. The variable flow rate approach is proposed for improvement the battery efficiency. The minimum electrolyte flow rate is calculated based on the current density, total vanadium concentration and SOC. In addition, the minimum flow rate is multiplied with the flow factor for adaptation to various battery structure system and designed. The effect of flow factor on the battery efficiency are shown in Figure 5.19a. For comparison between the constant and variable flow rate approaches at optimal point, the highest battery system efficiency of each approach was 78.05% and 80.85%, respectively and the battery capacity increase from 9.37 Ah to 10.39 Ah as well. Since the pump power loss has very valuable at only high SOC, the net pump power consumption of variable flow rate is lower than constant flow rate approach. In addition, the battery capacity

variation during 200 cycles of two approaches were shown in Figure 5.19b. During the first 80 cycles, the capacity of variable flow rate approach is higher than constant flow rate due to the improvement of mass transfer limit as mentioned whereas the rest cycles was lower. This result can be explained by the decreasing of electrolyte flow rate because the SOC at the latter cycles is reduced by electrolyte imbalance effect. Although the pump power loss of variable flow rate approach is lower than the constant flow rate, the system efficiency does not increase because the energy efficiency is decreased from the concentration overpotential at low electrolyte flow rate for long-term operation. Thus, the variable flow rate approach which electrolyte flow rate change with the SOC is suitable for operation if the level of electrolyte imbalance is low.

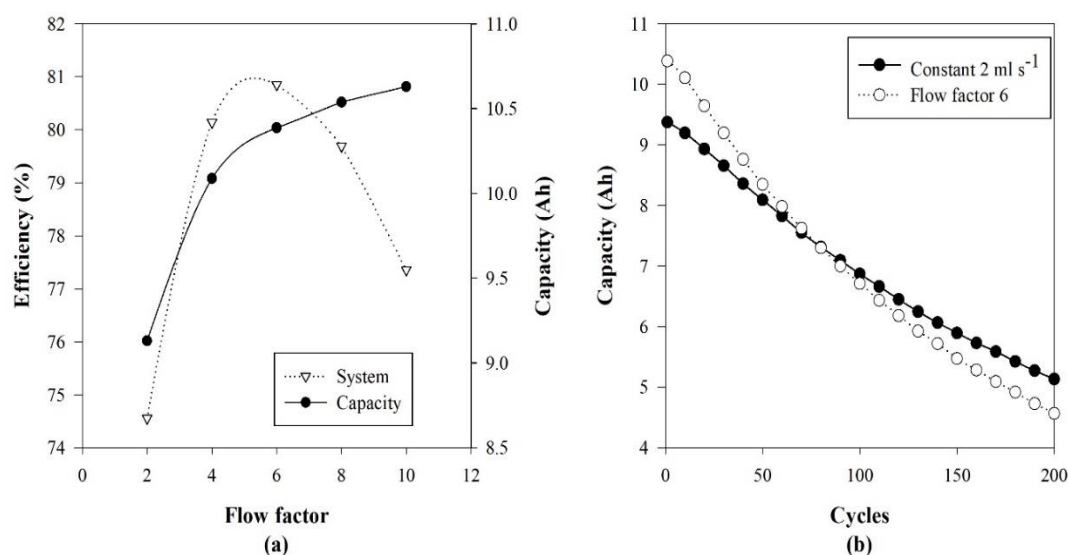


Figure 5.19 (a) Effect of flow factor on battery capacity and efficiency. (b) comparison the effect of constant and variable electrolyte flow rate approaches on long-term capacity.

CHAPTER VI

DESIGN OF ELECTROLYTE FLOW RATE CONTROL STRATEGY FOR IMPROVING THE PERFORMANCE OF VANADIUM REDOX FLOW BATTERY

6.1 Problem statements

As a vanadium redox flow battery is utilized in the energy management system, an optimization of the electrolyte flow rate is more efficiency approach to achieve the maximum system efficiency. Although the variable flow rate approach improves the battery efficiency by manipulating electrolyte flow rate in the function of the current density, total vanadium concentration, and SOC, the method only considers to reducing concentration overpotential at the end of charging-discharging process. The pumping energy could be decreased by reducing the electrolyte flow rate throughout the initial and middle stages while significantly increase the flow rate at the end stages. However, to increase the system efficiency, the electrolyte flow rate should be manipulated according to the variation of overpotentials including activation, concentration and ohmic. As a result, the dynamic optimization is taken into account for determining the optimal electrolyte flow rate maximizing the system efficiency which is the ratio of total discharging energy and charging energy and could be only determined when charging-discharging process finished. However, to maximize the system efficiency the total energy for charging battery to reach the upper voltage limit should be the lowest while the total discharging energy to reach the lower voltage limit should be the highest. As a result, the maximum system efficiency problem could be determined separately into the minimal total charging energy problem and the maximum total discharge energy as presented in Table 6.1.

Table 6.1 Problem statement for maximizing the system efficiency

Charging process	Discharging process
$\min_{Q(t)} J = \int_{t_0}^{t_f} IV_{\text{charge}} + P_{\text{pump}} dt$	$\max_{Q(t)} J = \int_{t_0}^{t_f} IV_{\text{discharge}} - P_{\text{pump}} dt$
subject to	subject to
$\dot{x} = f(x(t), Q, p, t)$ process model	$\dot{x} = f(x(t), Q, p, t)$ process model
$x(t_0) = x(0)$ initial condition	$x(t_0) = x(0)$ initial condition
$Q_L \leq Q \leq Q_U$	$Q_L \leq Q \leq Q_U$
$V(t_f) = 1.7$	$V(t_f) = 1.1$

6.2 Dynamic optimization

For charging battery, the optimal control problems were solved using the various number of time interval with start from 20 to 80 intervals. Figure 6.1 show the optimal flow rate profile during charging process with different time interval. As shown in Table 6.2, when use time interval of 20, the total energy at end of charging process is 15.7187 Wh and the terminal voltage is 1.710 V. However, when the increase the time interval to 40, the terminal voltage decreases to 1.695 V and the total energy for charging battery slightly decrease to 15.7183 Wh. According to this result, when the number of time interval increase, the amount of total charging energy and the voltage at the final time were decrease. This result could be explained by the fact that the determined optimal profile with piecewise constant is closer to the exact optimal value if the number of time interval increase to meet the requirement.

Table 6.2 Effect of time interval number on the total charging energy and battery voltage

Time interval	Charging energy (Wh)	Battery voltage (V)
20	15.7187	1.710
40	15.7183	1.695
60	15.7180	1.688
80	15.7179	1.687

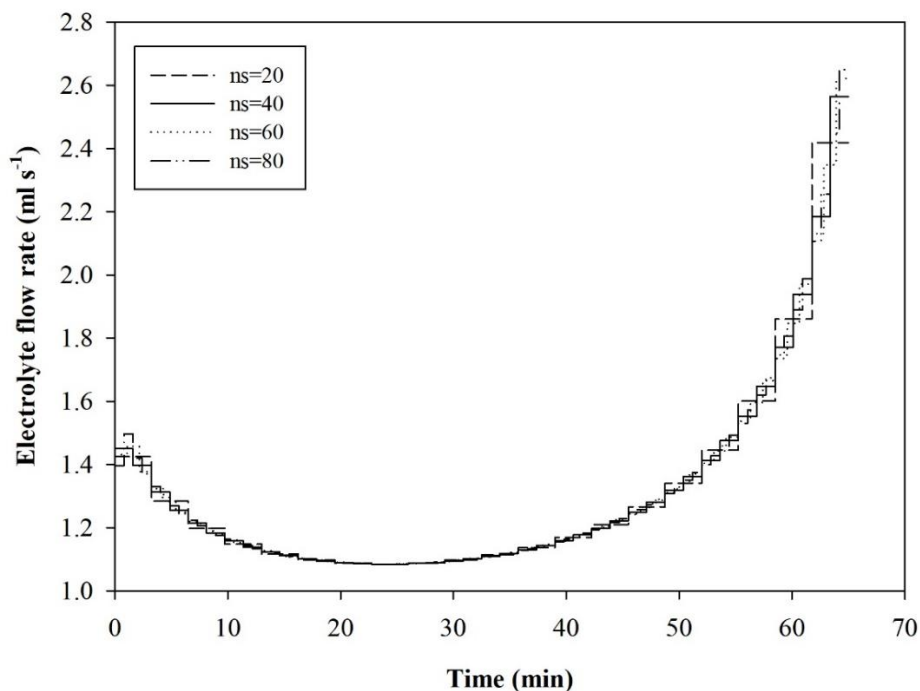


Figure 6.1 Optimal electrolyte profile with different time interval.

6.2.1 Comparison of the effect of electrolyte flow rate control strategies on the battery performance

In this section, the electrolyte flow rate is optimized for minimizing the total charging energy while maximizing the net discharging energy with the selected time interval of 40. The battery is applied with the constant charging-discharging current density of 120 mA cm^{-2} with the initial SOC of 1%. The battery is charged and discharged until the battery voltage reaches the upper and lower voltage limits, 1.7 V and 1.1 V, respectively. Figure 6.2 show the comparison of battery voltage under different flow rate control strategies which are a constant flow rate of 2 ml s^{-1} , the variable flow rate with flow factor of 6 and the optimal flow rate. As seen, the variable flow rate approach has the highest charging-discharging cycles time because the electrolyte flow rate significantly increases at the end of charging-discharging process for compensating the concentration overpotential as shown in Figure 6.3. This strategy can extend the time that battery voltage reaches the limit voltage, which means the battery can store and discharge more energy. However, low electrolyte flow rate in the early and middle stage of charging battery causes the sharply increase of battery

voltage. Consequently, the charging power of variable flow rate strategy is higher than the constant and optimal flow rate in the early and middle stages of charging process. Similarly, in discharging process, the discharging voltage decrease in the early and middle stages, as a result, the discharging power of variable flow rate strategy is lower than constant and optimal flow rate. This phenomenon can be explained as follow. The low electrolyte flow rate increases the resident time of the active species in cell enhancing the rate of vanadium concentration conversion as shown in Figure 6.4 and the highly change of vanadium concentration cause the sharply increase and decrease of open circuit voltage during charging and discharging process, respectively.

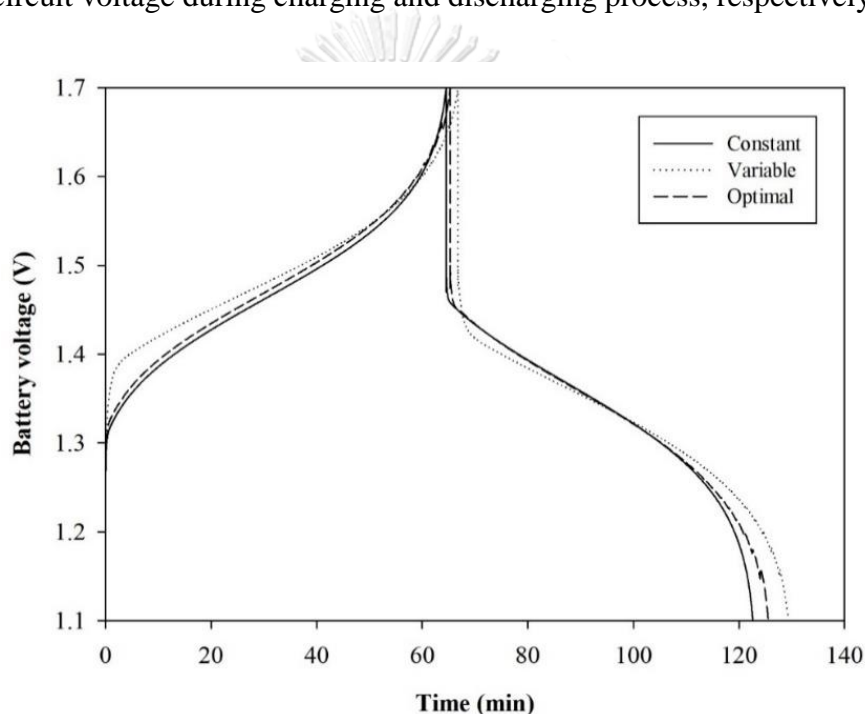


Figure 6.2 Battery voltage curve under different flow rate control strategies.

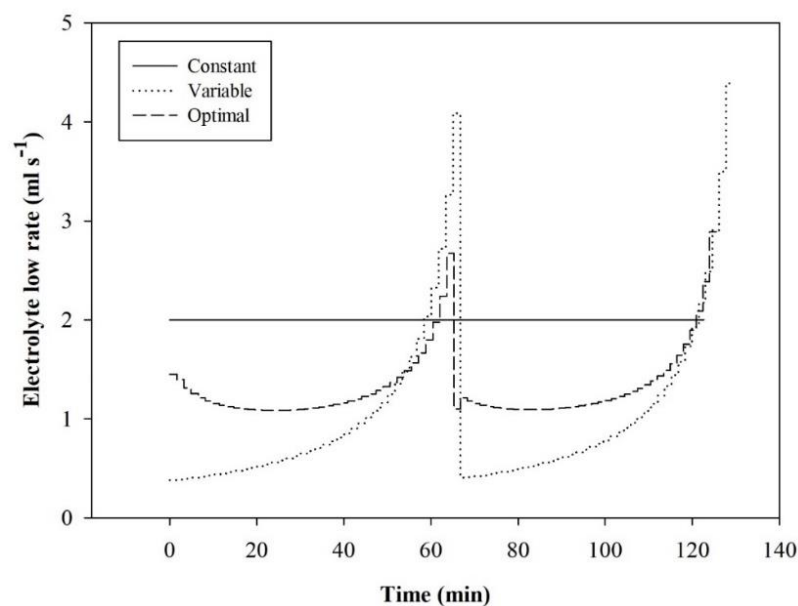


Figure 6.3 Electrolyte flow rate variation during charging-discharging process under different flow rate control strategies.

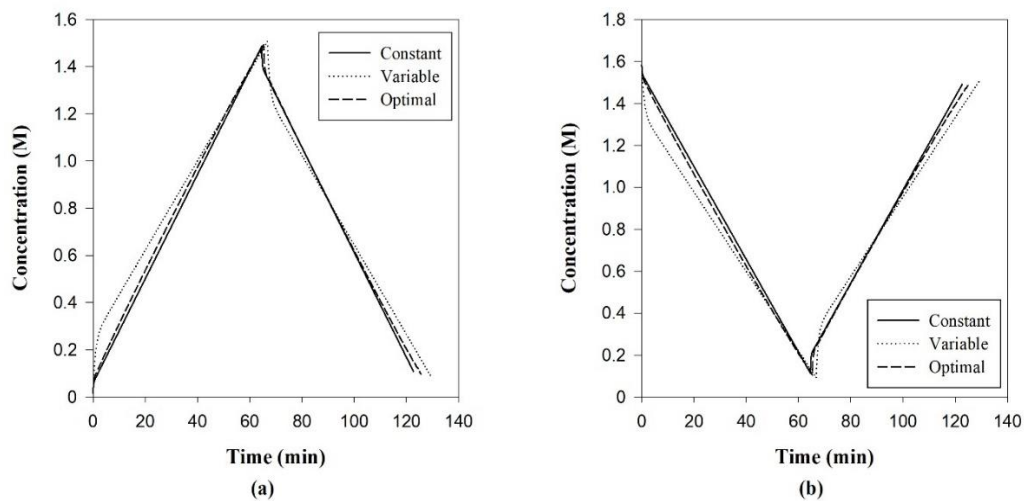


Figure 6.4 Variation of vanadium concentration in negative half-cell under different flow rate control strategies.

Although the variable flow rate strategy can increase the battery capacity, the low of electrolyte flow at the early stage causes the insufficient utilization of energy. During the initial of charging battery, it considerable consumes charging power because the battery voltage is high even though the battery SOC is low as mentioned above.

Moreover, since the flow rate increases at the end of charging process for decreasing the concentration overpotential and extending the energy stored time, it requires more charging power in this period because the battery reach to high voltage. As a result, the total energy for charging battery increase from increment of battery voltage at low SOC and the charging time at the high voltage. Similarly, the decrease of battery voltage in the early stage of discharging process cause the loss of high discharge power, moreover the large consumption of pump energy at the end state is used for extending the discharge process in the low range of discharging power. Consequently, the optimal electrolyte flow rate has a high value in the early stage of charging-discharging process for reducing the conversion of the vanadium concentration causing the decrease of open circuit voltage cell in charging process and increase the open circuit in discharging process. However, the electrolyte flow rate start decreasing as the open circuit voltage pass the steep region because the increasing flow rate does not reduce the open circuit in the flat region. Figure 6.5 show the effect of electrolyte flow rate on the open circuit voltage and the result confirms that decrease the electrolyte flow rate from 1.5 ml s^{-1} to 1.0 ml s^{-1} slightly increase the open circuit voltage cell, while decrease to 0.5 ml s^{-1} significant increases the open circuit voltage.

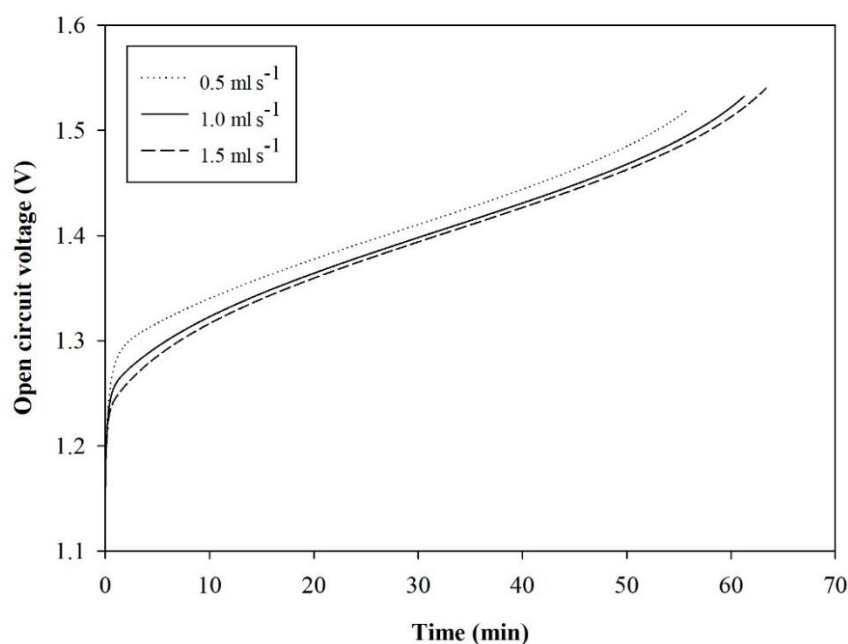


Figure 6.5 Effect of electrolyte flow rate on the open circuit voltage.

The comparison of charging-discharging performance with different control strategies is presented in Table 6.3. Although the charging energy for constant flow rate is the lowest, the battery only reaches 87.71% of SOC when the battery voltage reaches the upper limit of 1.7 V because the flow rate is not sufficient for increasing of concentration overpotential. The low stored energy at the end of charging process causes the lowest of discharge capacity and system efficiency. Even though the variable flow rate can extend the charging-time which increase the stored energy as seen from the highest SOC of 93.08%, the total energy for charging battery increase from increment of battery voltage at low SOC and extending of charging time at the high voltage. Similarly, increasing the electrolyte flow rate at the end of discharging process can increased the discharging time and achieve the highest discharge capacity of 10.11 Ah, but the pump energy is consumed for operating at low discharging power. As seen, the variable flow rate control can maximize the battery capacity, but this approach cannot achieve the highest system efficiency. In other hand, the optimal flow rate can minimize the charging energy and maximize discharging energy via manipulation the flow rate according to the variation of open circuit voltage and the concentration overpotential which can achieve a high system efficiency of 81.26%. Furthermore, the effect of current density on the optimal electrolyte flow rate profile was studied. Figure 6.6 presents the comparison of electrolyte flow rate between the variable flow rate and optimal flow rate control when applied with different charging current density from 80 to 120 mA cm⁻². It could be noticed that the optimal flow rate increase with an increase of current density and is similar to the variable flow rate control. This result confirm that proposed dynamic optimization algorithm determines the optimal electrolyte flow rate base on the variation of current density and SOC.

Table 6.3 Comparison of charging-discharging performance under different control strategies

Charging process			
	Constant flow	Variable flow	Optimal flow
SOC at V=1.7(%)	87.71	93.08	91.27
Charging energy (Wh)	15.67	16.30	15.80
Charging time (min)	64.55	66.75	65.3
Discharging process			
	Constant flow	Variable flow	Optimal flow
SOC at V=1.1 (%)	11.60	6.401	8.109
Discharging energy (Wh)	12.34	13.22	12.84
Discharging time (min)	58.10	62.45	60.20
Discharge capacity (Ah)	9.412	10.11	9.75
System efficiency (%)	78.75	81.10	81.26

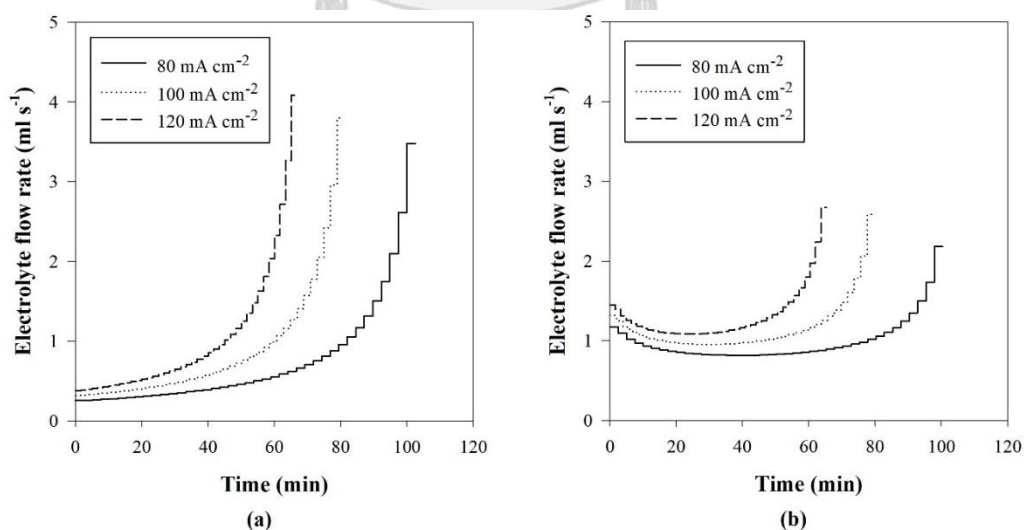


Figure 6.6 Comparison of electrolyte flow rate with different charging current density between (a) variable flow rate control and (b) optimal flow rate control.

Moreover, the effect of electrolyte imbalance on the electrolyte flow rate was investigated. The battery was charge at constant current and electrolyte flow rate of 120 mA cm^{-2} and 2 ml s^{-1} , respectively. Figure 6.7 presents the comparison of electrolyte flow rate profile under different electrolyte imbalance level between the variable flow rate control and the optimal flow rate control. It could be noticed that the electrolyte flow rate of variable strategy decreases while the flow rate of optimal strategy increases with an increase of electrolyte imbalance level. Since the maximum SOC decrease when electrolyte imbalance takes place, the electrolyte flow rate of variable control decreases with SOC. The charging time is shorted because too low electrolyte flow rate increases the concentration overpotential and accelerates the battery voltage to upper limit. In contrast with the optimal flow rate control, the flow rate increases for compensating the limiting of active species and extending the charging time when imbalance balance level increase. The charging-discharging time of the constant, variable and optimal flow rate control are summarized in Table 6.4. The charging-discharging time of variable flow control is only the highest when imbalance level equal 0.1, while the latter is lowest, and this result affect the discharge capacity as shown in Figure 6.8a. As a result, the system efficiency of variable flow rate decreases with the imbalance level, and the optimal control flow rate achieves the high system efficiency throughout the range of imbalance level (Figure 6.8b).

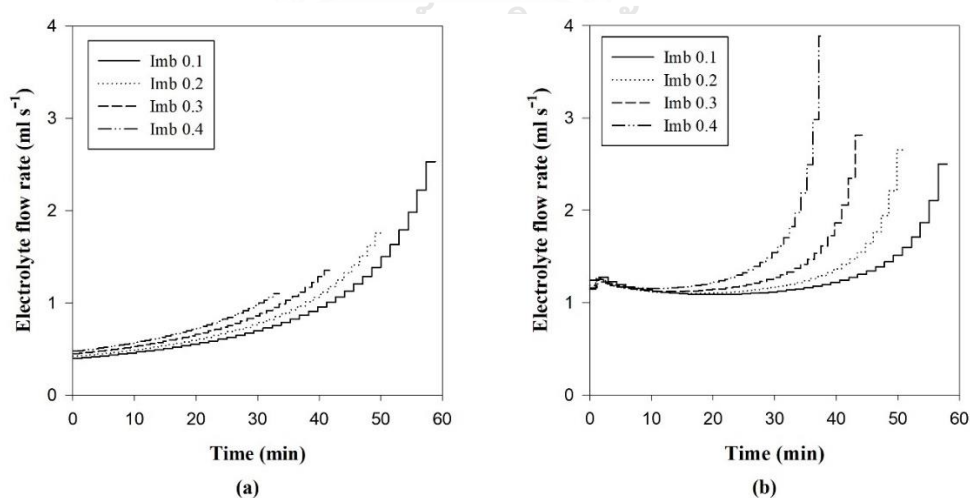


Figure 6.7 Comparison of electrolyte flow rate under different electrolyte imbalance level between (a) variable flow rate control (b) optimal flow rate control.

Table 6.4 Effect of electrolyte imbalance level on the charging-discharging time of different flow rate control strategies

Level of imbalance	Charging time (min)			Discharging time (min)		
	Constant flow	Variable flow	Optimal flow	Constant flow	Variable flow	Optimal flow
0.1	57.85	58.86	58.00	52.57	54.70	53.50
0.2	50.67	50.32	51.12	45.48	45.10	45.90
0.3	43.45	41.89	44.16	38.33	35.65	39.20
0.4	36.22	33.53	38.10	31.16	26.33	34.15

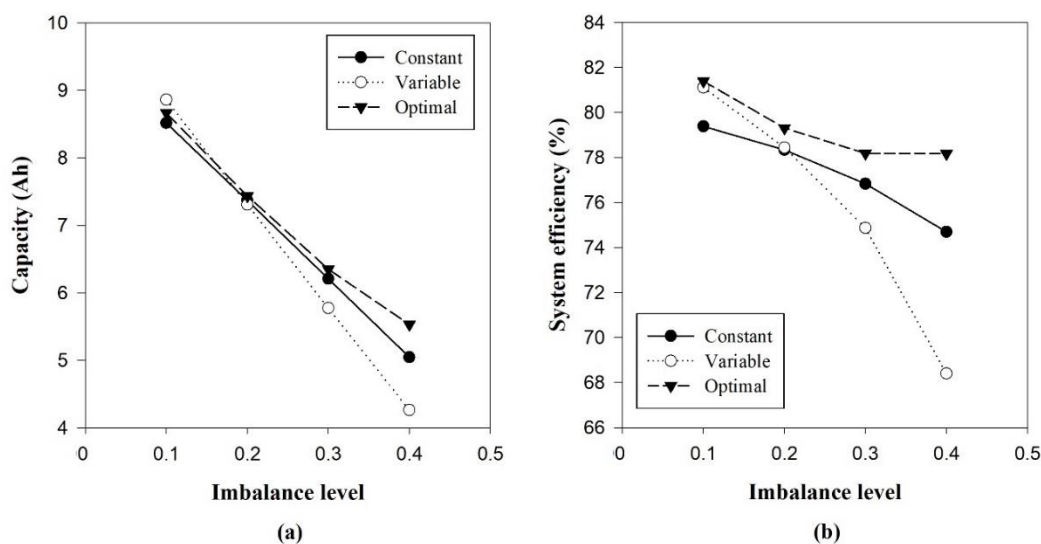


Figure 6.8 Effect of electrolyte imbalance under different flow rate control strategies on (a) battery capacity and (b) system efficiency.

6.2.2 Extended Kalman Filter for vanadium redox flow battery

Since the optimal electrolyte flow rate profile depends on the electrolyte imbalance level relating to the vanadium concentration, it is necessary to know the current state of vanadium concentration before solving the optimization. To monitor the imbalance level relating to the individual half-cell state of charge (SOC), the extended Kalman filter approach is adapted for estimating the vanadium concentration by measurement the modified OCV. To verify the performance of estimator, various

operating conditions were applied to the dynamic model according to Eqs. (4.19) and (4.20) for generating the reference data and the measurement outputs for the estimator. The estimation results were compared with the reference values, subsequently the mean absolute error of individual SOC and vanadium concentration were determined. Since the extended Kalman filter algorithm lack of exactly tuning method, the state error (P), process noise (Q) and measurement noise (R) covariance matrix are tuned based on trial and error method. The initial covariance matrix assigned to the EKF are presented in Table 6.5.

Table 6.5 Extended Kalman filter covariance matrix for vanadium redox flow batteries

Covariance matrix	Value
Initial state error covariance matrix (P_0)	diag (100 100 100 100)
Process noise covariance matrix (Q)	diag (0.02 0.02 0.02 0.02)
Measurement noise covariance matrix (R)	diag (0.0001 0.0001)

To track the variation of vanadium concentration, the battery was charged for 120 minutes with constant current density and flow rate of 60 mA cm^{-2} and 2 ml s^{-1} , respectively. During charging process, the modified open circuit cell measures the positive and negative open circuit voltage cell as the measurement input for extended Kalman filter (Figure 6.9). The estimation result of vanadium concentration in both half-cell is shown in Figure 6.10 and this result confirm that the proposed estimation algorithm can be applied for vanadium concentration estimation. Since the dynamic model of vanadium redox flow batteries is simplified by disregarding the convection term of the vanadium concentration between the cell and electrolyte reservoir, the variation of the electrolyte flow rate may affect the EKF performance. To confirm the robustness against the electrolyte flow rate, the constant and variable electrolyte flow rate profiles were applied on the reference model. The mean absolute error (MAE) of vanadium concentration with different flow rate are summarized in Table 6.6. As seen, the MAE of variable flow rate control is higher than the constant flow rate because the low flow rate at the early stage of variable flow control affects the sharply change of vanadium concentration. Thus, the error between the simplified model and the actual

concentration is slightly increased when compares with the constant flow rate. However, the estimator can handle with the variation of electrolyte flow rate and can predict the vanadium concentration although the tuning parameters for EKF are constant.

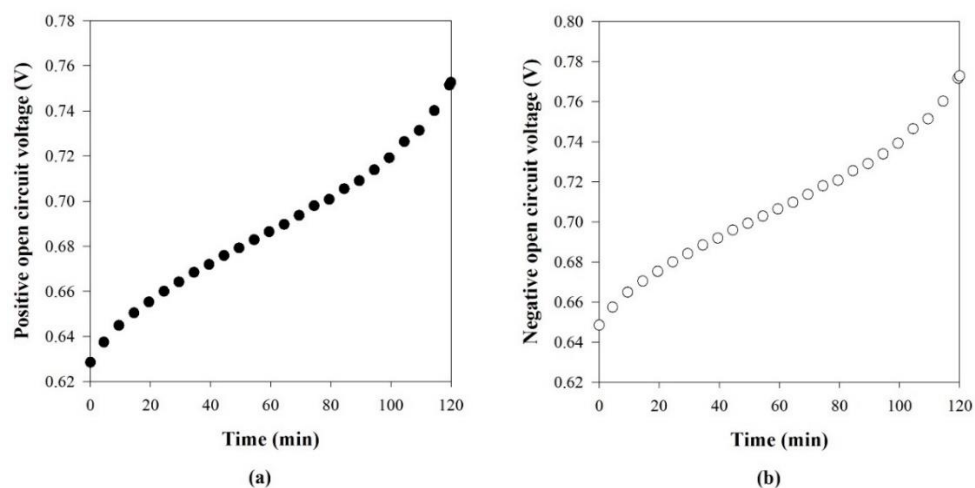


Figure 6.9 Positive and negative open circuit voltage measured by modified open circuit cell.

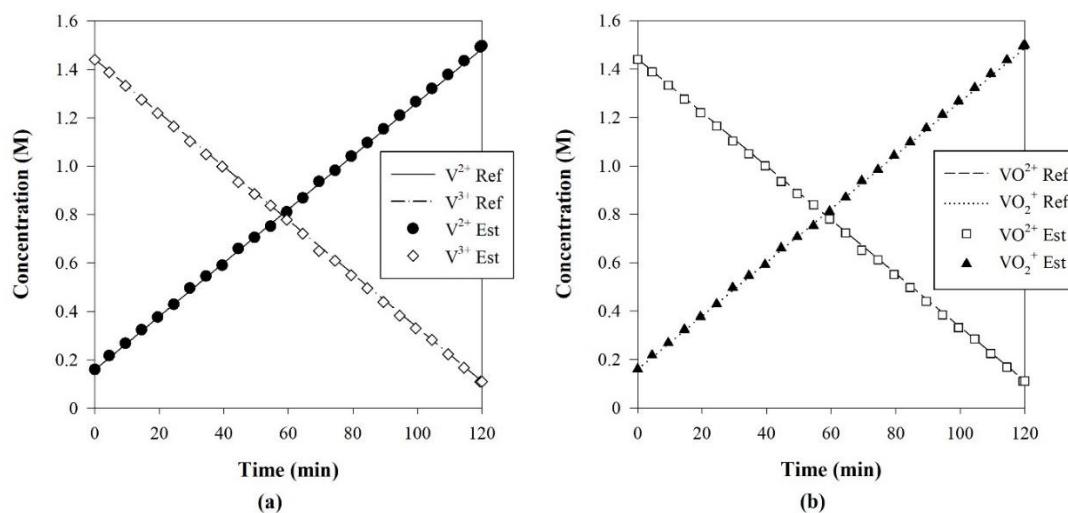


Figure 6.10 Estimation result of vanadium concentration in (a) negative half-cell and (b) positive half-cell.

Table 6.6 Mean absolute error of vanadium concentration with different flow rate control

Flow rate	MAE of concentration estimation (mM)			
	V ²⁺	V ³⁺	VO ²⁺	VO ₂ ⁺
1 ml s ⁻¹	4.794	8.192	7.571	5.117
2 ml s ⁻¹	6.791	7.623	6.949	7.491
flow factor 3	5.080	14.183	13.503	4.419
flow factor 6	4.934	11.301	10.62	5.460

The applied current for charging-discharging battery is the essential operating parameter affecting the variation of vanadium concentration. Hence, to confirm the robustness against the current variation, the positive and hybrid pulse of applied current density were used in charging battery (Figure 6.11). The vanadium concentration variation from the reference data are compared with the estimated result as shown in Figures 6.12 and 6.13. By the proposed estimator, it can be observed that both the estimated positive and negative concentration converge to the reference value with the low MAE as presented in Table 6.7 although the battery was charged-discharge with a highly fluctuating current density.

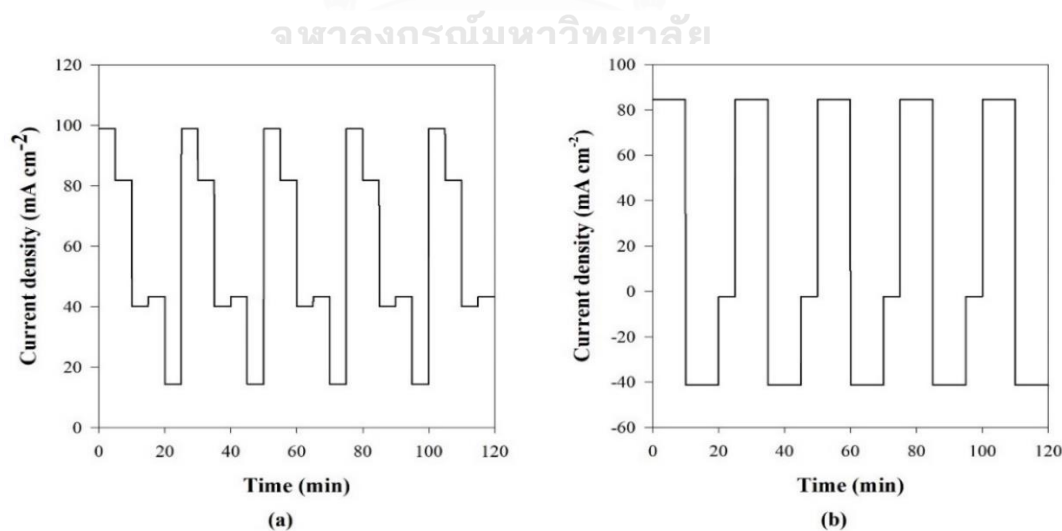


Figure 6.11 Charging current density with (a) positive pulse current and (b) hybrid pulse current.

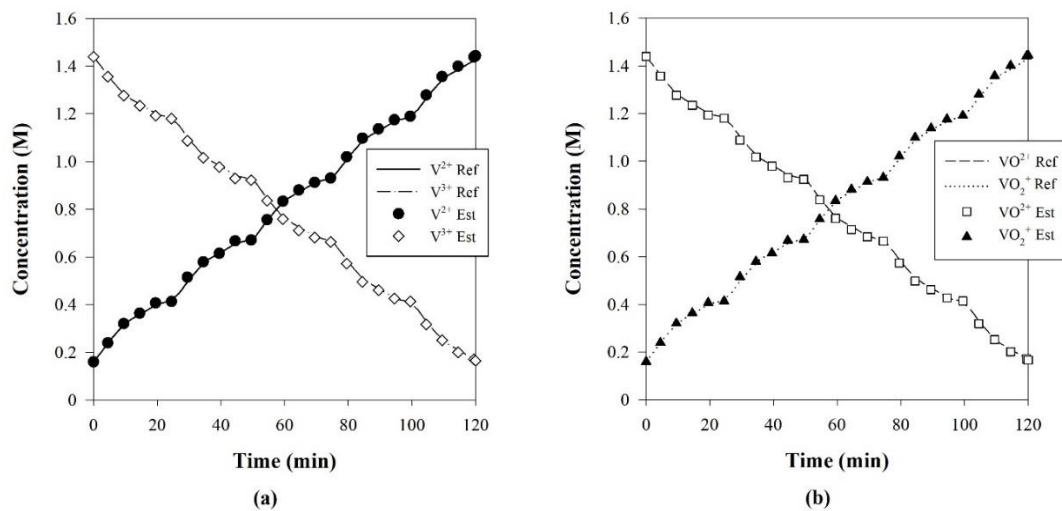


Figure 6.12 Estimation result of vanadium concentration under positive pulse charging current density.

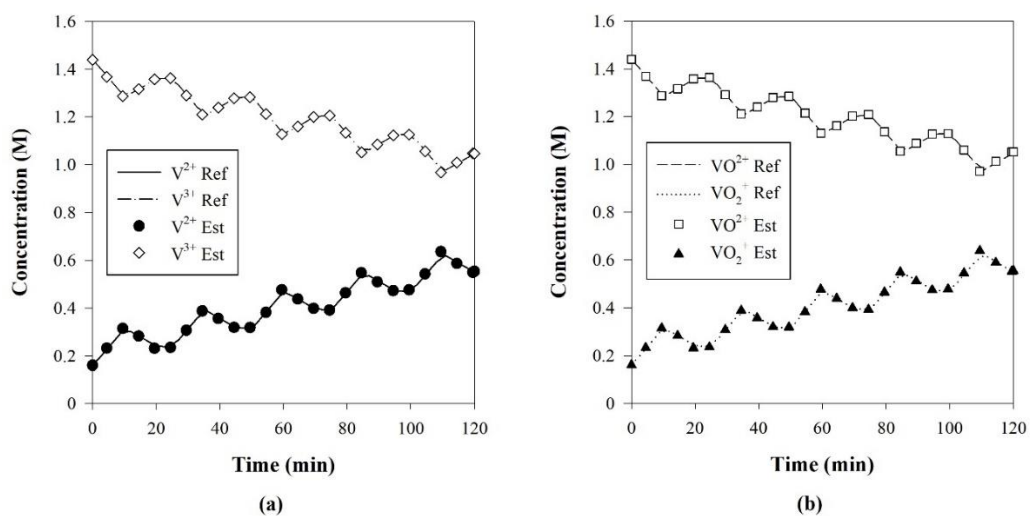


Figure 6.13 Estimation result of vanadium concentration under hybrid pulse charging current density.

Table 6.7 Mean absolute error of vanadium concentration with different current profile

Current	MAE of concentration estimation (mM)			
	V ²⁺	V ³⁺	VO ²⁺	VO ₂ ⁺
Positive pulse	7.684	8.32	7.653	8.437
Hybrid pulse	5.464	2.015	1.638	5.752

6.3 On-line dynamic optimization

To minimize the total energy for charging process and maximize in discharging process, the dynamic optimization problem is solved to determine a control profile of electrolyte flow rate driven the system from initial state to a final desired state. However, the charging-discharging current density fluctuates due to the variation of electricity demand. The pre-specified electrolyte flow rate profile may lose the optimal condition minimizing an objective function. An on-line optimization approach is applied to compensate the error from predicted current profile. Moreover, the optimal electrolyte flow rate also depends on the vanadium concentration and level of electrolyte imbalance. The implementation of on-line optimization required the knowledge of current states, vanadium concentration, in the system in order to modify a new optimal profile of electrolyte flow rate. Consequently, the state estimator was integrated into the propose on-line optimization for updating the initial condition in the solving algorithm.

6.3.1 Effect of current density fluctuation on the optimal electrolyte flow rate profile

The optimal electrolyte flow rate profile for charging battery could be determined by dynamic optimization if the charging current density was defined. However, the current density can fluctuate and the optimal flow change with the amount of charging current density as presented in section 6.2.1, thus it is important to recalculate the optimal profile of the electrolyte flow rate to consist with the variation of current density. Figure 6.14a show the predicted constant current density of 100 mA cm⁻² for charging the battery in 60 minutes, hence the electrolyte flow rate profile is updated every 1.5 minutes if the selected time interval is 40. The optimal electrolyte

flow rate profile determined by the prediction charging current density is shown in Figure 6.14c. However, the actual current density varies between the range of 60-160 mA cm^{-2} (Figure 6.14b), thus the optimal flow rate profile obtained from the on-line optimization change with the variation of current density as presented in Figure 6.14d. Interestingly, at the end of charging process, the on-line flow rate attempt to increase although the charging current step decrease due to the compensating effect of concentration overpotential at high SOC.

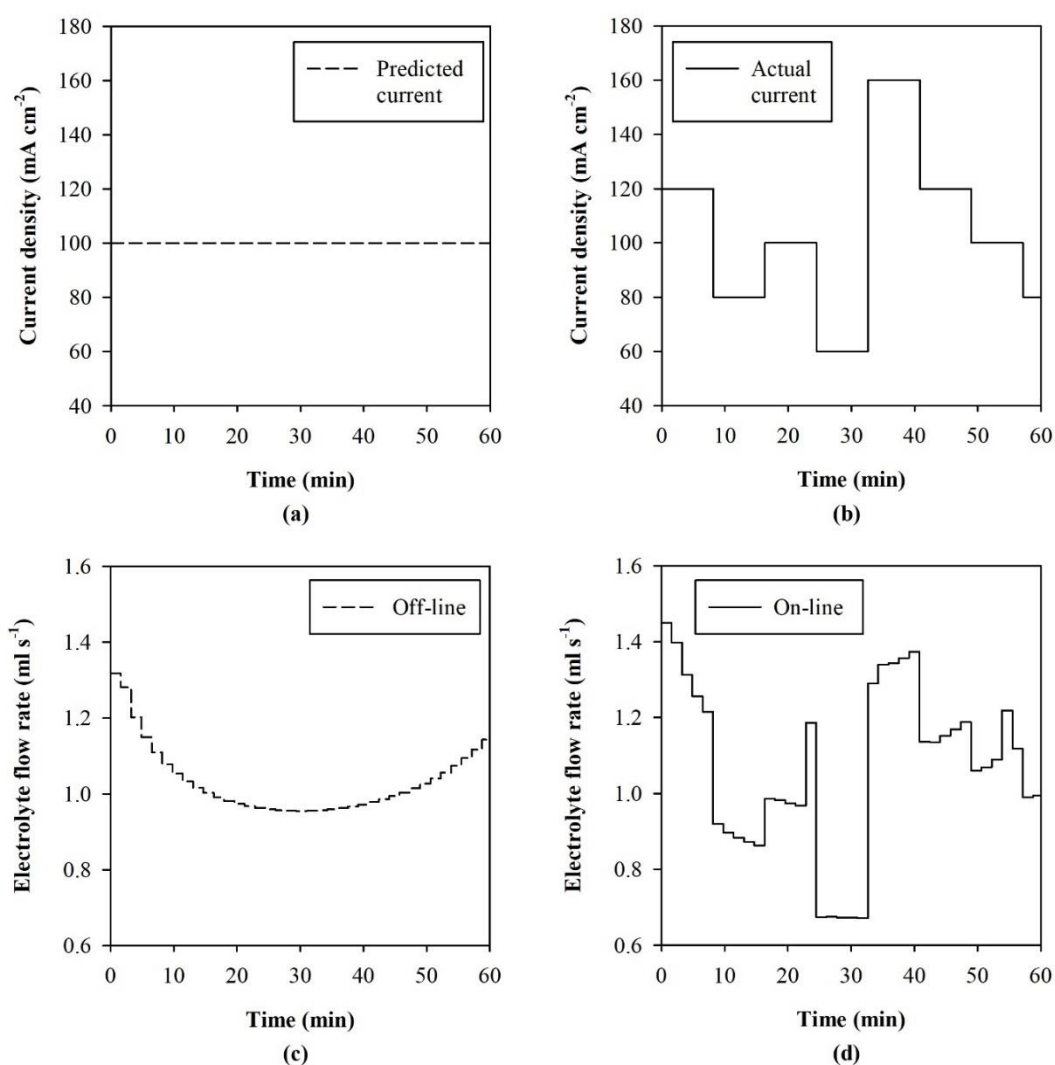


Figure 6.14 Effect of current density on the optimal electrolyte flow rate profile.

To compare the effect of electrolyte flow rate between off-line and on-line flow rate on the battery performance, the battery voltage profile and the total energy for charging battery were investigated (Figure 6.15). The battery voltage applied with the off-line flow rate control is higher than the on-line flow rate control in range at the predicted current is lower than the actual current density because the battery was charged with the low flow rate. In contrast, if the actual current is lower than the predicted current, the off-line flow rate is higher than the on-line flow rate causing the decrease of battery voltage. However, the total charging energy between applied with the on-line and off-line is slightly different because the actual charging current density vary approximate to the predicted current, as a result the off-line flow rate could be used for charging the battery with this actual current density profile.

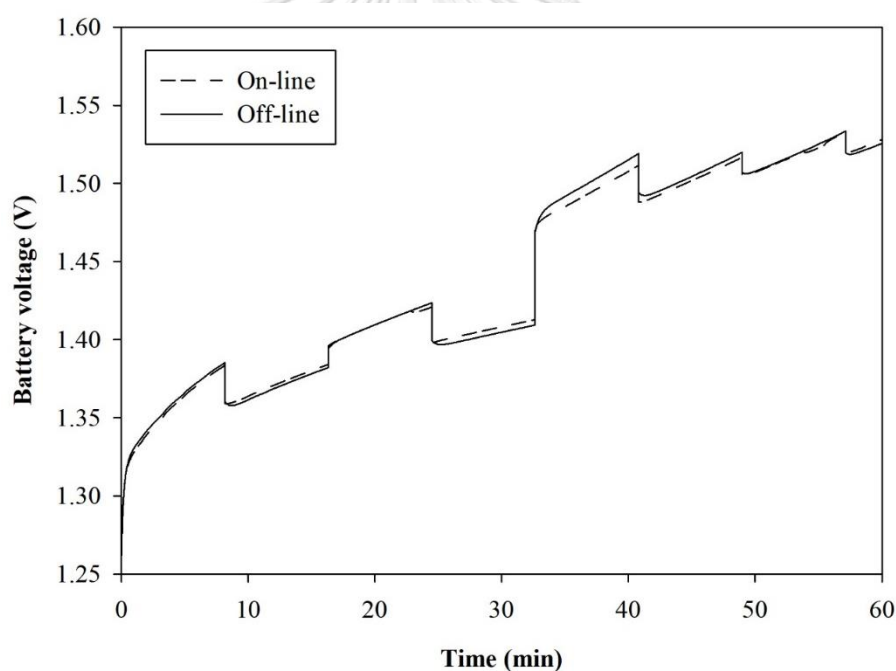


Figure 6.15 Comparison of battery voltage under off-line flow rate and on-line flow rate control.

However, if too low current density was predicted when compare with the actual current density as presented in Figure 6.16. The off-line electrolyte flow rate profile is lower than the value that should be and charging battery with the off-line flow rate significantly increase the battery voltage affecting the increase of total charging energy. Furthermore, insufficient of electrolyte flow at high SOC cause the battery voltage

rapidly increases to the upper limit voltage and stop the charging process as presented in Figure 6.17. The charging process with the off-line electrolyte flow rate finished at 58.51 minutes and the SOC equals 83.97%, while charging with on-line optimal flow rate, the battery can charge to 90.18% and the battery voltage did not reach the upper voltage limit of 1.7 V in 60 minutes. Consequently, the on-line optimization is required for recalculating the optimal electrolyte flow rate value to be consisted the variation of charging-discharging current density. This approach could increase the system efficiency and prevent the battery voltage reach to the limit voltage before the battery achieve the desired SOC.

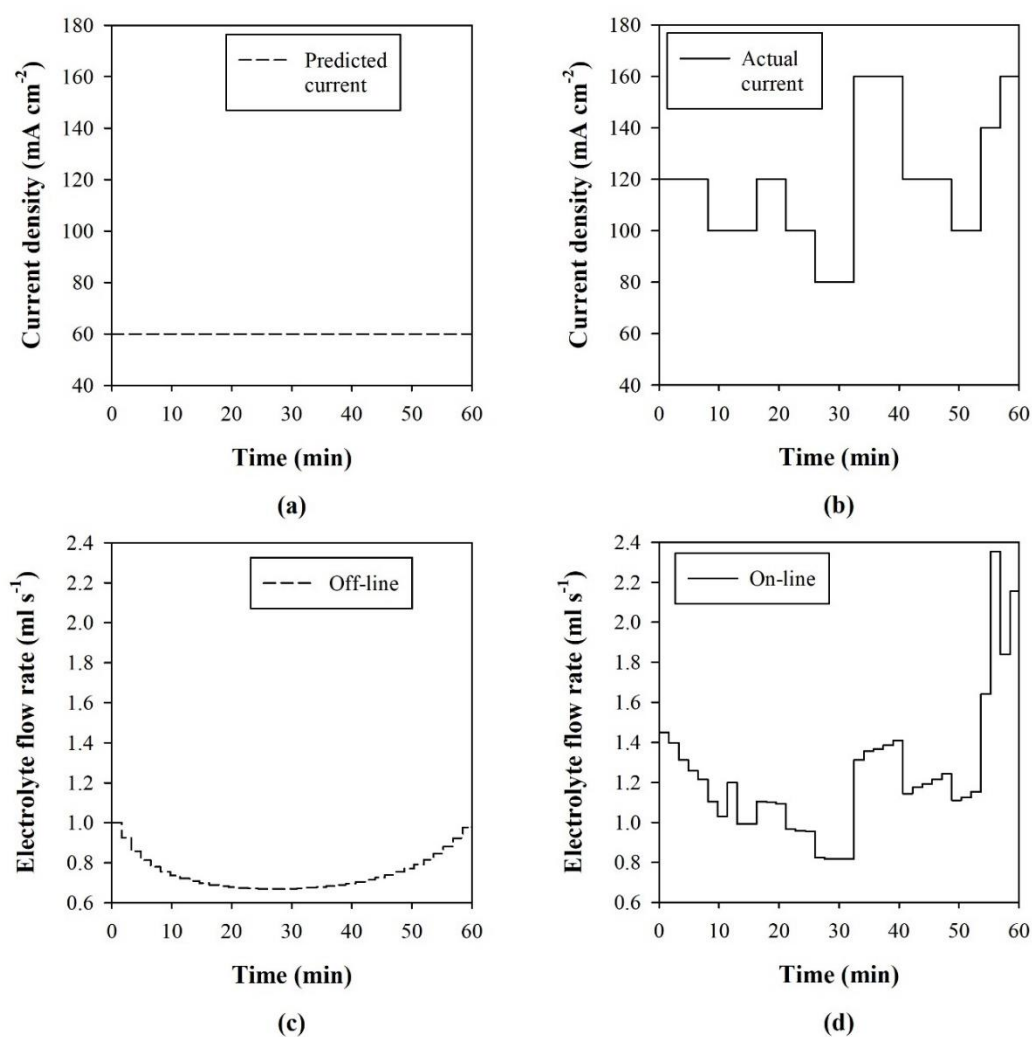


Figure 6.16 Effect of high charging current density on the on-line electrolyte flow rate profile.

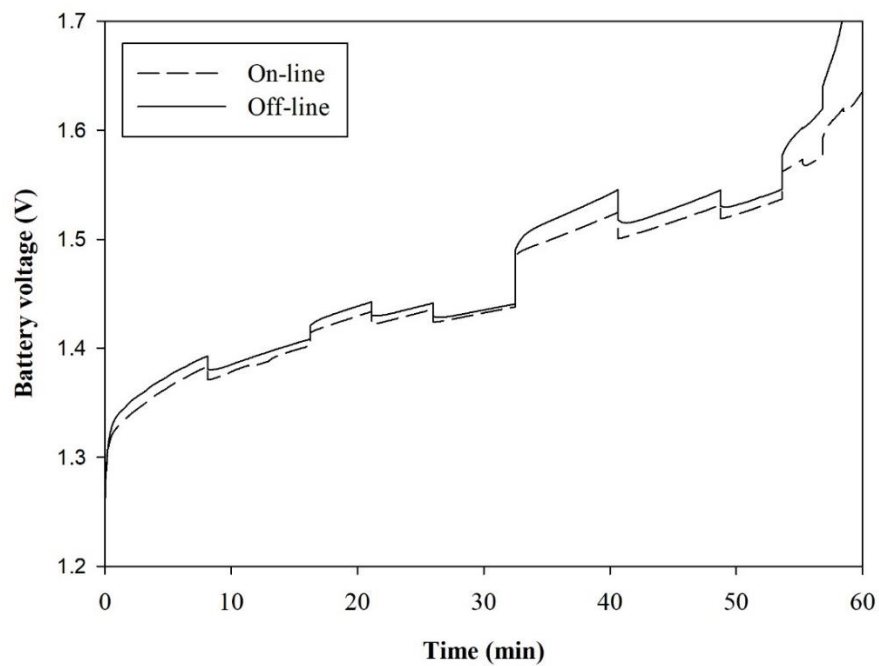
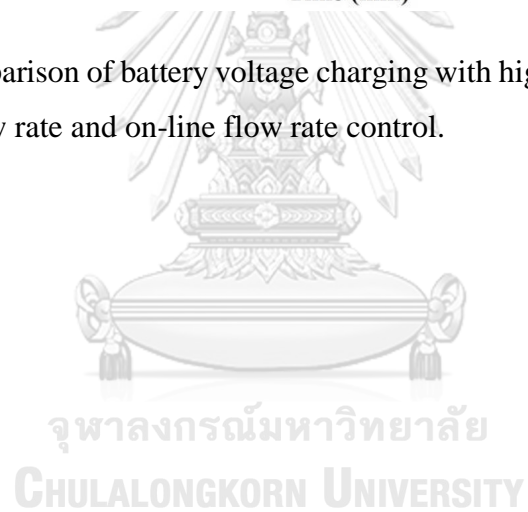


Figure 6.17 Comparison of battery voltage charging with high charging current density under off-line flow rate and on-line flow rate control.



CHAPTER VII

CONCLUSIONS AND RECOMMENDATIONS

9.1 Conclusions

A dynamic model of a vanadium redox flow battery (VRFB) taking into account the electrolyte imbalance was first developed to investigate the efficiency and capacity loss of the battery. The developed model explained the gassing side reactions, oxygen (OER) and hydrogen (HER) evolution, coupled with the mass balance of the vanadium and proton ions, and was validated with the experimental charge-discharge characteristic voltage curves. The theoretical analysis of the electrolyte imbalance in the VRFB using the proposed model revealed that the rate of capacity loss from the gassing side reactions (i.e., HER and OER) depended on electrode and membrane material as well as operating conditions. Moreover, the variation in the vanadium ions during long-term operation relied on the presence of the gassing and self-discharge side reactions. The proposed model can predict which half-cell has the limiting active specie, leading to a plan for rebalancing the capacity in that half-cell. The effect of key operating parameters on the battery performance was also analyzed for a long-term VRFB operation. The battery power and capacity can be increased by using high vanadium and proton concentration. However, the rate of capacity degradation increased with an increase in the total vanadium concentration and proton concentration; moreover, increase the proton concentration result in the increased rates of the hydrogen and oxygen evolution. The increase in the operating temperatures decreased the activation overpotential; however, it enhanced the diffusion of vanadium in the VRFB, increasing the imbalance level. As a result, the VRFB was suggested to be operated at low temperatures for avoiding the gassing and self-discharge reactions. The variable flow rate control can reduce the energy penalty and increase the battery capacity by decreasing the mass transfer limit. Nonetheless, this approach did not improve the battery capacity and efficiency for the long-term operation. The optimization problem of the VRFB was considered to improve its performance. The results showed that the implementation of an optimal electrolyte flow rate can

maximize the system efficiency, regarding the variation in an open circuit voltage and concentration overpotential. When the VRFB was operated with the optimal flow rate of electrolyte, the operating current density is increased and the level of the electrolyte imbalance is decreased, leading to higher system efficiency than that with the constant and variable flow rate control. Finally, an on-line dynamic optimization of the VRFB was performed to update the optimal electrolyte flow rate profile. The extended Kalman filter was integrated with the on-line dynamic optimization to estimate the vanadium concentration using measured data from the modified open circuit voltage. The results showed that the use of the on-line dynamic optimization approve can increase the system efficiency and prevent the battery voltage from reaching the limited cell voltage before the battery achieved the desired state of charge.

9.2 Recommendations

9.2.1 Since the concentrations of vanadium in the VRFB change with an electrolyte volume, the effect of a variation in the electrolyte volume on the electrolyte imbalance should be investigated. The model of the VRFB should predict the battery capacity when the electrolyte volumes of both half cells are not equal.

9.2.2 Regarding a multi-cell VRFB system, the shunt current causes a difference in the applied current on each cell, leading to the decrease of energy efficiency. Thus, the effect of the shunt current loss on the battery performance should be considered for designing the VRFB cell stack.

9.2.3 During the operation of VRFB, the battery may stay in a standby period and the self-discharge side reactions in a cell can continuously occur. Moreover, heat of self-discharge side reactions may cause the precipitation of vanadium in the cell. The electrolyte should be modified with an additive for increasing the operating temperature range and the developed model should include the effect of the electrolyte temperature during operating and standby-periods.

9.2.4 To determine an optimal flow rate profile of electrolyte, a multi-objective function for maximizing both battery capacity and system efficiency should be considered. Furthermore, to solve the on-line optimization of the VRFB, the current state of

vanadium concentrations is needed to be known. Due to its ability to handle the nonlinear mapping with short calculation time, an artificial neural network can be trained to estimate the vanadium concentrations from known measured variables such as battery voltage and implemented in solving the on-line optimization problem to find an optimal electrolyte flow rate. Thus, the performance of the artificial neural network integrated with the on-line optimization approach should be investigated.



REFERENCES

- Al-Fetlawi, H., Shah, A. A., & Walsh, F. C. (2009). Non-isothermal modelling of the all-vanadium redox flow battery. *Electrochimica Acta*, 55, 78-89.
- Al-Fetlawi, H., Shah, A. A., & Walsh, F. C. (2010). Modelling the effects of oxygen evolution in the all-vanadium redox flow battery. *Electrochimica Acta*, 55, 3192-3205.
- Aneke, M., & Wang, M. (2016). Energy storage technologies and real life applications – A state of the art review. *Applied Energy*, 179, 350-377.
- Arpornwichanop, A., Kittisupakorn, P., & Mujtaba, I. M. (2005). On-line dynamic optimization and control strategy for improving the performance of batch reactors. *Chemical Engineering and Processing: Process Intensification*, 44, 101-114.
- Badrinarayanan, R., Zhao, J., Tseng, K. J., & Skyllas-Kazacos, M. (2014). Extended dynamic model for ion diffusion in all-vanadium redox flow battery including the effects of temperature and bulk electrolyte transfer. *Journal of Power Sources*, 270, 576-586.
- Boettcher, P. A., Agar, E., Dennison, C., & Kumbur, E. C. (2016). Modeling of ion crossover in vanadium redox flow batteries: A computationally-efficient lumped parameter approach for extended cycling. *Journal of the Electrochemical Society*, 163, A5244-A5252.
- Chen, C. L., Yeoh, H. K., & Chakrabarti, M. H. (2014). An enhancement to Vynnycky's model for the all-vanadium redox flow battery. *Electrochimica Acta*, 120, 167-179.
- Chen, H., Cong, T. N., Yang, W., Tan, C., Li, Y., & Ding, Y. (2009). Progress in electrical energy storage system: A critical review. *Progress in Natural Science*, 19, 291-312.
- Fetyan, A., El-Nagar, G. A., Lauermann, I., Schnucklake, M., Schneider, J., & Roth, C. (2018). Detrimental role of hydrogen evolution and its temperature-dependent impact on the performance of vanadium redox flow batteries. *Journal of Energy Chemistry*.

- Hadjipaschalis, I., Poulikkas, A., & Efthimiou, V. (2009). Overview of current and future energy storage technologies for electric power applications. *Renewable and Sustainable Energy Reviews*, 13, 1513-1522.
- Khazaeli, A., Vatani, A., Tahouni, N., & Panjeshahi, M. H. (2015). Numerical investigation and thermodynamic analysis of the effect of electrolyte flow rate on performance of all vanadium redox flow batteries. *Journal of Power Sources*, 293, 599-612.
- Knehr, K. W., & Kumbur, E. C. (2011). Open circuit voltage of vanadium redox flow batteries: Discrepancy between models and experiments. *Electrochemistry Communications*, 13, 342-345.
- Liu, H., Xu, Q., Yan, C., & Qiao, Y. (2011). Corrosion behavior of a positive graphite electrode in vanadium redox flow battery. *Electrochimica Acta*, 56, 8783-8790.
- Luo, X., Wang, J., Dooner, M., & Clarke, J. (2015). Overview of current development in electrical energy storage technologies and the application potential in power system operation. *Applied Energy*, 137, 511-536.
- Ma, X., Zhang, H., Sun, C., Zou, Y., & Zhang, T. (2012). An optimal strategy of electrolyte flow rate for vanadium redox flow battery. *Journal of Power Sources*, 203, 153-158.
- Ma, X., Zhang, H., & Xing, F. (2011). A three-dimensional model for negative half cell of the vanadium redox flow battery. *Electrochimica Acta*, 58, 238-246.
- Merei, G., Adler, S., Magnor, D., & Sauer, D. U. (2015). Multi-physics Model for the Aging Prediction of a Vanadium Redox Flow Battery System. *Electrochimica Acta*, 174, 945-954.
- Mohammadi, T., Chieng, S. C., & Skyllas Kazacos, M. (1997). Water transport study across commercial ion exchange membranes in the vanadium redox flow battery. *Journal of Membrane Science*, 133, 151-159.
- Mohammadi, T., & Skyllas-Kazacos, M. (1995). Use of polyelectrolyte for incorporation of ion-exchange groups in composite membranes for vanadium redox flow battery applications. *Journal of Power Sources*, 56, 91-96.
- Newman, J., & Thomas-Alyea, K. E. (2012). *Electrochemical systems*: John Wiley & Sons.

- Ngamsai, K., & Arpornwichanop, A. (2015a). Analysis and measurement of the electrolyte imbalance in a vanadium redox flow battery. *Journal of Power Sources*, 282, 534-543.
- Ngamsai, K., & Arpornwichanop, A. (2015b). Investigating the air oxidation of V(II) ions in a vanadium redox flow battery. *Journal of Power Sources*, 295, 292-298.
- Ngamsai, K., & Arpornwichanop, A. (2015c). Measuring the state of charge of the electrolyte solution in a vanadium redox flow battery using a four-pole cell device. *Journal of Power Sources*, 298, 150-157.
- Nicolas Watrin, B. B. a. A. M. (2012). Review of adaptive systems for lithium batteries. in *Proceedings of IEEE Transportation Electrification Conference and Expo*, pp. 1–6.
- Oh, K., Yoo, H., Ko, J., Won, S., & Ju, H. (2015). Three-dimensional, transient, nonisothermal model of all-vanadium redox flow batteries. *Energy*, 81, 3-14.
- Pavelka, M., Wandschneider, F., & Mazur, P. (2015). Thermodynamic derivation of open circuit voltage in vanadium redox flow batteries. *Journal of Power Sources*, 293, 400-408.
- Rohit, A. K., Devi, K. P., & Rangnekar, S. (2017). An overview of energy storage and its importance in Indian renewable energy sector. *Journal of Energy Storage*, 13, 10-23.
- Roznyatovskaya, N., Herr, T., Küttinger, M., Fühl, M., Noack, J., Pinkwart, K., & Tübke, J. (2016). Detection of capacity imbalance in vanadium electrolyte and its electrochemical regeneration for all-vanadium redox-flow batteries. *Journal of Power Sources*, 302, 79-83.
- Schafner, K., Becker, M., & Turek, T. (2018). Capacity balancing for vanadium redox flow batteries through electrolyte overflow. *Journal of Applied Electrochemistry*.
- Schweiss, R., Pritzl, A., & Meiser, C. (2016). Parasitic hydrogen evolution at different carbon fiber electrodes in vanadium redox flow batteries. *Journal of the Electrochemical Society*, 163, A2089-A2094.
- Shah, A. A., Al-Fetlawi, H., & Walsh, F. C. (2010). Dynamic modelling of hydrogen evolution effects in the all-vanadium redox flow battery. *Electrochimica Acta*, 55, 1125-1139.

- Shah, A. A., Watt-Smith, M. J., & Walsh, F. C. (2008). A dynamic performance model for redox-flow batteries involving soluble species. *Electrochimica Acta*, 53, 8087-8100.
- Skyllas-Kazacos, & McCann, J. F. (2015). Chapter 10 - Vanadium redox flow batteries (VRBs) for medium- and large-scale energy storage. In *Advances in Batteries for Medium and Large-Scale Energy Storage* (pp. 329-386): Woodhead Publishing.
- Skyllas-Kazacos, M., & Goh, L. (2012). Modeling of vanadium ion diffusion across the ion exchange membrane in the vanadium redox battery. *Journal of Membrane Science*, 399, 43-48.
- Skyllas-Kazacos, M., Menictas, C., & Lim, T. (2013). 12 - Redox flow batteries for medium- to large-scale energy storage A2 - Melhem, Ziad. In *Electricity Transmission, Distribution and Storage Systems* (pp. 398-441): Woodhead Publishing.
- Sukkar, T., & Skyllas-Kazacos, M. (2003). Water transfer behaviour across cation exchange membranes in the vanadium redox battery. *Journal of Membrane Science*, 222, 235-247.
- Sun, J., Shi, D., Zhong, H., Li, X., & Zhang, H. (2015). Investigations on the self-discharge process in vanadium flow battery. *Journal of Power Sources*, 294, 562-568.
- Tang, A., Bao, J., & Skyllas-Kazacos, M. (2011). Dynamic modelling of the effects of ion diffusion and side reactions on the capacity loss for vanadium redox flow battery. *Journal of Power Sources*, 196, 10737-10747.
- Tang, A., Bao, J., & Skyllas-Kazacos, M. (2012). Thermal modelling of battery configuration and self-discharge reactions in vanadium redox flow battery. *Journal of Power Sources*, 216, 489-501.
- Tang, A., Bao, J., & Skyllas-Kazacos, M. (2014). Studies on pressure losses and flow rate optimization in vanadium redox flow battery. *Journal of Power Sources*, 248, 154-162.
- Wang, T., Fu, J., Zheng, M., & Yu, Z. (2017). Dynamic control strategy for the electrolyte flow rate of vanadium redox flow batteries. *Applied Energy*.

- Weber, A. Z., Mench, M. M., Meyers, J. P., Ross, P. N., Gostick, J. T., & Liu, Q. (2011). Redox flow batteries: a review. *Journal of Applied Electrochemistry*, 41, 1137.
- Xiong, B., Zhao, J., Tseng, K. J., Skyllas-Kazacos, M., Lim, T. M., & Zhang, Y. (2013). Thermal hydraulic behavior and efficiency analysis of an all-vanadium redox flow battery. *Journal of Power Sources*, 242, 314-324.
- Xu, Q., Zhao, T. S., & Leung, P. K. (2013). Numerical investigations of flow field designs for vanadium redox flow batteries. *Applied Energy*, 105, 47-56.
- Yan, Y., Li, Y., Skyllas-Kazacos, M., & Bao, J. (2016). Modelling and simulation of thermal behaviour of vanadium redox flow battery. *Journal of Power Sources*, 322, 116-128.
- Yang, W. W., He, Y. L., & Li, Y. S. (2015). Performance Modeling of a Vanadium Redox Flow Battery during Discharging. *Electrochimica Acta*, 155, 279-287.
- You, D., Zhang, H., & Chen, J. (2009). A simple model for the vanadium redox battery. *Electrochimica Acta*, 54, 6827-6836.
- Zhang, L., Ling, L., Xiao, M., Han, D., Wang, S., & Meng, Y. (2017). Effectively suppressing vanadium permeation in vanadium redox flow battery application with modified Nafion membrane with nacre-like nanoarchitectures. *Journal of Power Sources*, 352, 111-117.

VITA

NAME Tossaporn Jirabovornwisut

DATE OF BIRTH 13 September 1993

PLACE OF BIRTH Bangkok

**INSTITUTIONS
ATTENDED** Chulalongkorn university

HOME ADDRESS 421 Prachautid 98 Thungku Bangkok 10140

PUBLICATION Effect of the electrolyte imbalance on performance of a vanadium redox flow battery: Dynamic simulation and analysis

